UNIVERSITY OF SOUTHAMPTON

FACULTY OF PHYSICAL AND APPLIED SCIENCES

Optoelectronics Research Centre

Design and Application of a Distributed Optical Fibre Dynamic Strain Sensor

Ali Masoudi

Thesis for the degree of Doctor of Philosophy

January 2015

UNIVERSITY OF SOUTHAMPTON

ABSTRACT

FACULTY OF PHYSICAL AND APPLIED SCIENCES

OPTOELECTRONICS RESEARCH CENTRE

Doctor of Philosophy

DESIGN AND APPLICATION OF A DISTRIBUTED OPTICAL FIBRE DYNAMIC STRAIN SENSOR

by Ali Masoudi

Over the past two decades, distributed optical fibre sensors (DOFS) based on Brillouin and Raman scattering have been extensively studied. As a result, a wide range of distributed temperature and strain sensors with different sensing range and accuracy levels have been developed. However, due to the weak nature of Brillouin and Raman scattering, most of the research in this field has been focused on DC or quasi-DC measurement of temperature and strain. On the other hand, the Rayleigh-based DOFS which have been previously proposed are only able to detect dynamic disturbances along the sensing fibre. In this thesis, a new sensing technique has been developed which is capable of quantifying and tracking multiple dynamic perturbations along the sensing fibre, simultaneously.

The sensing mechanism of the proposed technique relies on the phase of the Rayleigh backscattered light. For any given segment along the fibre, the difference in the phase of the backscattered light radiating from the two ends of that segment changes as a function of the external perturbations at that segment. Therefore, dynamic vibration along the sensing fibre can be extracted by comparing the phase of the backscattered light from two different sections of the sensing fibre. By implementing this technique using an imbalanced Mach-Zehnder Interferometer (IMZI), a distributed sensor was developed that was capable of quantifying dynamic perturbations within the frequency range of $200Hz \sim 5kHz$ along a $1km$ sensing fibre.

Furthermore, the same principle was used to develop a distributed magnetic field sensor. By coupling an optical fibre to a magnetostrictive wire and by using this combination as a magnetic field to strain transducer, a distributed magnetic field sensor was formed with magnetic intensity range of $1Gs \sim 8Gs$ and frequency range of $50Hz \sim 5kHz$. In addition, the IMZI arrangement was used as a frequency-to-intensity convertor to develop a distributed dynamic strain sensor based on Brillouin scattering. The proposed sensor exhibited a strain range of $400\mu\varepsilon \sim 4m\varepsilon$ and a sensing range of $2km$.

Contents

List of Figures

List of Tables

DECLARATION OF AUTHORSHIP

I, Ali Masoudi, declare that the thesis entitled "Design and Application of Distributed Optical Fibre Dynamic Strain Sensors" and the work presented in the thesis are both my own, and have been generated by me as the result of my own original research. I confirm that:

- this work was done wholly or mainly while in candidature for a research degree at this University;
- where any part of this thesis has previously been submitted for a degree or any other qualification at this University or any other institution, this has been clearly stated;
- where I have consulted the published work of others, this is always clearly attributed;
- where I have quoted from the work of others, the source is always given. With the exception of such quotations, this thesis is entirely my own work;
- I have acknowledged all main sources of help;
- where the thesis is based on work done by myself jointly with others, I have made clear exactly what was done by others and what I have contributed myself;
- parts of this work have been published as the journal papers and conference contributions listed in Appendix D.

Signed: _____

Date: _____

Acknowledgments

First and foremost, I would like to express my sincere gratitude to my supervisor, Dr. Trevor Newson, for his support and encouragement throughout my PhD tenure. I have been fortunate to have a supervisor who gave me the freedom to explore on my own, and at the same time the guidance to recover when my steps faltered.

Special thanks go to my colleague Dr. Mohammad Belal for his intellectual and practical assistance in the lab.In addition, I wish to express my gratitude to the following people for their help and support during the past four years: Dr. Morten Ibsen, Dr. James Gates, Dr. Yongmin Jung, Martin Nunez Velazquez, Reza Sandoghchi, Simon Butler, and David Turner.

Finally, I would like to thank my wonderful family, especially my dear parents, to whom this dissertation is dedicated to. None of this would have been possible without their love and patience.

Abbreviations

φ-OTDR	Phase-Sensitive Optical Time Domain Reflectometry
AOM	Acousto-Optic Modulator
ASE	Amplified Spontaneous Emission
BOTDA	Brillouin Optical Time Domain Analysis
BOTDR	Brillouin Optical Time Domain Reflectometry
CRN	Coherent Rayleigh Noise
CW	Continuous Wave
DAS	Distributed Acoustic Sensor
DCM	Differentiate and Cross-multiply
DFB	Distributed Feed-back
DOFMS	Distributed Optical Fibre Magnetic-field Sensor
DOFS	Distributed Optical Fibre Sensor
DVS	Distributed vibration Sensor
EDFA	Erbium-Doped Fibre Amplifier
EM	Electromagnetic Wave
FBG	Fibre Bragg Grating
FFT	Fast Fourier Transform
FSR	Free Spectral Range
FUT	Fibre Under Test
IIR	Infinite-duration impulse response
IMZI	Imbalanced Mach-Zehnder Interferometer
MZI	Mach-Zehnder Interferometer
NA	Numerical Aperture
NEP	Noise Equivalent Power
OSC	Oscilloscope
OFS	Optical Fibre Sensor
OTDR	Optical Time Domain Reflectometry
POFDR	Polarization Optical Frequency Domain Reflectometry
POTDR	Polarization Optical Time Domain Reflectometry
ROTDR	Raman Optical Time Domain Reflectometry
SBS	Stimulated Brillouin Scattering
SMF	Single Mode Fibre
SNR	Signal to Noise Ratio
SPL	Sound Pressure Level
SSMF	Standard Single Mode Fibre
WDM	Wavelength Division Multiplexing

Chapter 1

Introduction

1.1 Optical Fibre Sensor and its Advantages

Today, sensors play an increasingly important role in various aspects of human life, from, for instance, measuring the heart rate of a patient to monitoring power-grid networks. Amongst the various types of sensing mechanisms, optical fibre-based sensors (OFS) have attracted a considerable amount of attention due to the advantages they offer such as robustness, flexibility, and high sensitivity. However, what distinguishes OFS from their rivals is the capability of a certain category of these sensors to spatially resolve measurands along the sensing fibre. This class of sensors which are known as distributed optical fibre sensors (DOFS) use the optical scattering phenomenon in optical fibre to measure the physical variables such as temperature, strain, and magnetic field. In recent years, the majority of studies on DOFS have been focused on using inelastic scattering processes (*i.e.* Brillouin and Raman scattering) to measure physical phenomena such as temperature and strain. High sensitivity, simplicity, and long sensing-range of Brillouin- and Raman-based DOFS have established them as the primary means of measurement in many applications from monitoring the strain across large structures such as bridges to measuring the temperature profiles of power cables. However, since the Raman and Brillouin scattering processes are relatively weak in comparison with Rayleigh scattering, the sensing procedures for the sensors that are based on Brillouin and Raman scattering require a lot of averaging. Therefore, DOFS based on these scattering processes are best reserved for DC and quasi-DC measurement of temperature and strain *i.e.* measurands which are either constant or varying very slowly with time. To overcome this issue, a technique has been introduced and developed which is based on the phase of the backscattered Rayleigh light.

1.2 Research Objectives

The aim of this research was to develop a DOFS capable of measuring the dynamic strain along the sensing fibre and to expand this concept to design distributed sensors

for other dynamic phenomena such as distributed dynamic magnetic field sensing. The concept was to use the phase variation between the coherent Rayleigh backscattered light from two segments of the sensing fibre to detect the strain-induced phase change between those segments. Such DOFS can not only be used to quantify the vibrations of stationary objects along the sensing fibre, but also to track mobile objects along its path. There are a variety of applications for distributed sensors capable of measuring dynamic phenomena. In the oil and gas industry, for instance, they can be used to detect leakage along the pipelines. They can be used in the rail industry to track trains across the rail networks and to monitor the condition of the trains and the railways. Perimeter security and monitoring the power grids can be mentioned among the other applications of these distributed sensors.

1.3 Thesis Outline

This thesis is organized in seven chapters. A brief description of each chapter is given below:

In chapter 2, the basic principles of distributed optical fibre sensors are presented. The Rayleigh, Brillouin, and Raman scattering processes are explained and the limitations they impose on DOFS are discussed. Recent research on Rayleigh- and Brillouin-based distributed dynamic strain sensors is presented and their fundamental limitations are pointed out. The chapter concludes with a review of the recent studies on distributed magnetic field sensors.

Chapter 3 establishes the basic principles of the distributed dynamic strain sensor studied in this thesis. The theory of phase sensitive optical time domain reflectometry ($\varphi - OTDR$) is presented through mathematical equations and diagrams. It is explained how an imbalanced Mach-Zehnder interferometer (MZI) can be combined with a 3×3 coupler to extract the phase of the backscattered light while avoiding the fading effect. The experimental setup and the output results of the sensor are presented, followed by a discussion on its capabilities and limitations.

Chapters 4 and 5 expand on the concept introduced in chapter 3 to demonstrate a distributed acoustic sensor and distributed magnetic field sensor, respectively. The effect of the dimension and compound of the coating of the sensing fibre to acoustic vibrations is analyzed in chapter 4 and the response of different fibres to acoustic vibration generated by a loud speaker is presented and discussed.

In chapter 5, the magnetostrictive properties of a Nickel wire are utilized to measure the dynamic magnetic field. It is shown how the dynamic magnetic field can be quantified by coupling an optical fibre and a Nickel wire and by measuring the magnetic-field-induced strain on the optical fibre. The theoretical and experimental aspects of the sensor are presented and discussed as well.

In chapter 6, a Brillouin-based distributed dynamic strain sensor is introduced which uses the concept described in chapter 3 to passively avoid the fading effect. The theoretical section demonstrates how the strain-induced frequency shift in backscattered Brillouin light is converted to optical intensity variation by an imbalanced MZI. The experimental work and results are presented, and advantages and drawbacks of the sensor are discussed.

Finally, chapter 7 summarizes the research and provides an outlook on the future of these sensors and recommendations for potential future works.

Chapter 2

Distributed Optical Fibre Sensor: Principles and Literature Review

2.1 Introduction

Optical fibre sensors (OFS) are generally classified into two main categories; these are extrinsic sensors (where the optical fibre is used to carry the light to and from the sensing target) and intrinsic sensors (where the fibre itself is used as the sensing element) [1]. Intrinsic optical fibre sensors are further categorized into single-point sensors, quasi-distributed sensors, and distributed sensors [2]. Single-point sensors are the simplest form of intrinsic sensor where the sensor measures the net effect of the measurand on the entire length of the sensing fibre. Figure 2.1(a) shows an example of such a sensor. In this configuration, which is know as Mach-Zehnder interferometer (MZI), the sensing arm is exposed to the sensing target while the reference arm is kept isolated. Changes in the physical properties of the sensing arm are measured by combining the light emerging from the sensing and the reference arms and monitoring the intensity variation at the output ports.

Another class of intrinsic sensors are quasi-distributed sensors which are sensitive to measurands at certain and predetermined points along the length of the sensing fibre. Fibre Bragg grating-based OFS are the most common type of quasi-distributed sensors where multiple fibre Bragg gratings (FBG) with different Bragg wavelengths are combined to form the sensing fibre (Figure 2.1(b)). The sensing procedure of such sensors relies on the variation of the wavelength of the reflected light from each individual FBG due to changes in their physical properties such as their length.

Unlike quasi-distributed OFS where the sensing fibre is sensitive at discrete sections of the optical fibre, a distributed optical fibre sensor (DOFS) is capable of measuring physical phenomena all along the fibre since it does not rely on the introduction of any extra features to individual sections of the optical fibre (Figure 2.1(c)). Instead, DOFS relies on the scattering of light within the fibre. As light propagates inside an optical fibre, it interacts with its surrounding medium. As a consequence of this interaction,

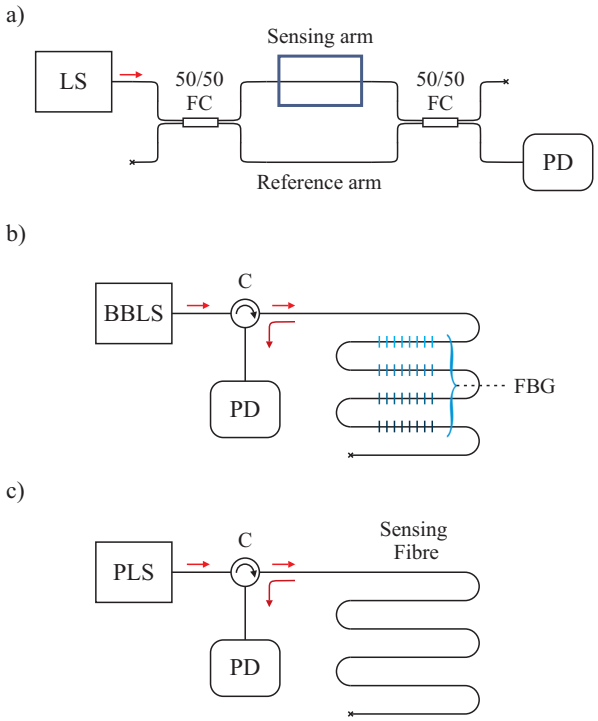

Figure 2.1: Three categories of intrinsic optical fibre sensors (a) single-point sensor, (b) quasi-distributed sensor, and (c) distributed sensor. LS: Laser source; FC: Fibre coupler; PD: Photodetector; BBLS: Broad-band laser source; C: Circulator; FBG: Fibre Bragg grating; PLS: Pulsed laser source.

light scatters in all directions. A fraction of the scattered light which propagates backward towards the front end of the fibre is called the backscattered light. The sensing procedure of DOFS relies on this backscattered light which carries useful information about the physical condition of the fibre at the point where the scattering has occurred.

2.2 Principles of Light Scattering

Despite the conventional perception which considers the scattering of light as a redirection of light that occurs when a light ray encounters the particles of a medium, the light-scattering process is in fact a complex interaction between an incident electromagnetic (EM) wave and atoms or molecules of a medium. Light scattering occurs through three different processes [3]: Rayleigh scattering, Brillouin scattering, and Raman scattering. These scattering processes are investigated in the rest of this section.

2.2.1 Rayleigh Scattering

When an EM wave encounters density fluctuations in an otherwise homogeneous medium, it periodically perturbs the electron cloud of the molecules within the medium. The oscillation of the electron cloud results in a periodic polarization of atoms or molecules in that region which forms an oscillating dipole moment. The oscillation of the induced

dipole moment leads to the radiation of a secondary EM wave known as Rayleigh scattering. It can be shown that the sum of the secondary waves radiated from a fully homogeneous medium is zero in all directions except in the direction of the propagation of the incident wave [4]. Therefore, the Rayleigh scattering phenomenon can be observed in an inhomogeneous medium only. Furthermore, since the induced dipole moments are oscillating at the same frequency of the incident EM wave, the wavelength of the Rayleigh scattered light is equal to that of the incident light. Therefore, the Rayleigh scattering phenomenon is an elastic process.

Rayleigh scattering occurs due to randomly-distributed density fluctuations in the fibre. These inhomogeneities, which in size are much smaller than the wavelength of the propagating light, form during the fibre fabrication process. Although a carefully planned fabrication process can reduce the size and concentration of these inhomogeneities, it cannot eliminate them completely.

Rayleigh scattering is characterized by a coefficient which is inversely proportional to the power of four of the wavelength of the incident light, λ. For a condensed isotropic media, this coefficient is given as

$$\gamma_R = \frac{8\pi^3}{3\lambda^4} n^8 p^2 \beta_T K T_F \tag{2.1}$$

where the description of the parameters along with their values for a standard single-mode fibre (SSMF) is given in table 2.1. The derivation of this equation is provided in Appendix A.

2.2.2 Brillouin Scattering

Brillouin scattering, first predicted by Leon Brillouin in 1922, occurs as a result of the interaction between incident light and thermally generated acoustic phonons. Since acoustic phonons are quantized vibrational modes of atoms or molecules in condensed matter, they can be considered as thermally generated acoustic waves propagating in all directions over a wide range of frequencies. Therefore, Brillouin scattering can be thought of as the diffraction of incident light due to the periodic variation in the refractive index of a medium caused by acoustic waves.

The Brillouin scattering process within an optical fibre follows similar principles as

Symbol	Description	Value
n	Fibre refractive index	1.46
p	Average photoelastic coefficient	0.286
β_T	Isothermal compressibility at T_F	$7 \times 10^{-11}\, m^2 N^{-1}$
K	Boltzmann's constant	$1.38 \times 10^{-23}\, J\, K^{-1}$
T_F	Fictive temperature	$1950^{\circ} K$

Table 2.1: Definition of the parameters in equation (2.1) along with their values for a standard single-mode fibre.

that within bulk material. As the light travels through the fibre, it interacts with the thermally generated acoustic phonons. Among all the phonons in the fibre, only those which are phase-matched with the incident light (*i.e.* those which satisfy the Bragg condition) contribute to the Brillouin scattering process. Under the Bragg condition, it can be shown that [5]

$$2n\,\lambda_a\,\sin(\frac{\varphi}{2}) = \lambda_P \tag{2.2}$$

where n is the refractive index of the fibre, λ_a is the wavelength of the acoustic wave, φ is the angle between the incident and scattered light, and λ_P is the wavelength of the incident light. Figure 2.2 illustrates the process of Brillouin scattering for an acoustic wave propagating parallel to the waveguide. From all the scattered rays, however, only those within the numerical aperture (NA) of the fibre are guided by the fibre. Therefore, only the acoustic phonons propagating in parallel with the axis of the fibre contribute towards the Brillouin backscattered light which is guided towards the front-end of the fibre.

As a result of the interaction of light with the acoustic phonons travelling at a velocity v_a, the scattered light undergoes a Doppler shift. The frequency of the acoustic phonons, f_a, can be expressed in terms of its velocity, v_a, and its wavelength

$$f_a = \frac{v_a}{\lambda_a}. \tag{2.3}$$

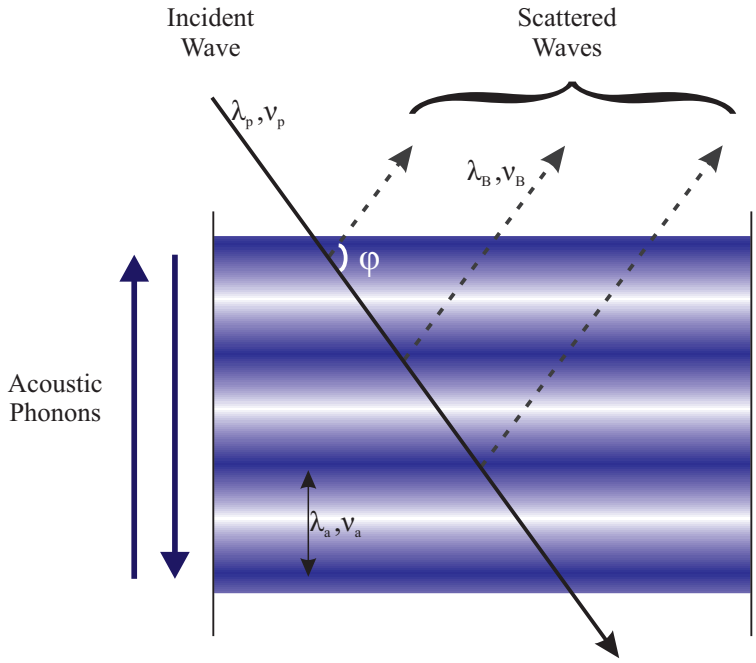

Figure 2.2: Brillouin scattering (λ_B) as a result of interaction between an incident light (λ_P) and thermally generated acoustic waves (λ_a).

Combining equations (2.3) and (2.2) gives

$$f_a = \frac{2n}{\lambda_P}\, \upsilon_a\, \sin(\frac{\varphi}{2}). \tag{2.4}$$

which demonstrates the frequency of the phonons in terms of the wavelength of the incident light and the refractive index of the fibre. The frequency difference between the incident and scattered light, which is called Brillouin frequency shift, $\Delta\nu_B$, is equal to the frequency of the acoustic wave, f_a. Since only the scattered light in forward and backward directions is guided (*i.e.* $\varphi = 0^o$ and $\varphi = 180^o$), the frequency shift of the Brillouin backscattered light is[1]

$$|\nu_p - \nu_{BS}| = |\Delta\nu_B| = \frac{2n}{\lambda_P}\, \upsilon_a \tag{2.5}$$

where ν_p and ν_{BS} are the frequencies of the incident and backscattered light, respectively. The sign of the Brillouin frequency shift depends on whether the acoustic wave is co-propagating or counter-propagating with the incident light. Equation (2.5) shows that, for a given incident wavelength, the Brillouin frequency shift depends only on the refractive index of the fibre and the acoustic velocity within the fibre. In turn, both of these parameters are dependent on the environmental conditions of the fibre such as its temperature and strain. In addition, the intensity of the Brillouin backscattered light is also dependent on the temperature and strain of the fibre. The Brillouin scattering coefficient, γ_B, is given by [6]

$$\gamma_B = \frac{8\pi^3}{3\lambda^4}\, n^8 p^2\, K\, T\, (\rho \upsilon_a^2)^{-1} \tag{2.6}$$

where T is the absolute temperature and ρ is the mean density of the fibre. Therefore, by analyzing the intensity and frequency of the Brillouin backscattered light, the distributed strain and temperature along the sensing fibre can be unambiguously measured [7, 8].

2.2.3 Raman Scattering

In section 2.2.1, it was shown that the induced dipole moment, $\mathbf{P}$, is the source of Rayleigh scattering where

$$\mathbf{P} = \alpha \mathbf{E}. \tag{2.7}$$

Here, $\mathbf{E}$ is the incident electric field and α is the polarizability of the medium. The assessment of Rayleigh scattering was carried out with an assumption that the value of α is fixed at each point along the medium. However, since polarizability is defined as the ability of a medium to be polarized, the value of α depends on the instantaneous position of the individual atoms within that medium as well. Considering the fact that the individual atoms vibrate within the boundary of their molecular bonds, the value of

[1] For $\varphi = 0^o$, equation (2.4) shows that $\Delta\nu_B = 0$. This shows that the Brillouin scattering is mainly a backward process.

α can be written as

$$\alpha = \alpha_0 + \frac{\partial \alpha}{\partial Q}\, dQ \tag{2.8}$$

where α_0 is the polarizability at equilibrium and dQ is the physical displacement of the atoms. In addition, for a given molecular bond, quantum mechanics has shown that the individual atoms are confined to specific vibrational modes in which the vibrational energy levels of each vibrational mode, $\mathcal{E}_j$, are quantized, and is given by [9]

$$\mathcal{E}_j = (\, j + \frac{1}{2}) \, h\nu_{vib} \tag{2.9}$$

where j is the vibrational quantum number ($j = 0, 1, 2, ...$), h is the Planck's constant, and ν_{vib} is the frequency of the vibrational mode. Therefore, the physical displacement of an atom with vibrational frequency of ν_{vib} can be expressed as

$$dQ = Q_0 \, \cos(2\pi \, \nu_{vib} t) \tag{2.10}$$

where Q_0 is the maximum displacement about the equilibrium position. Combining equations (2.8), (2.9) and (2.10) gives

$$\mathbf{P} = \mathbf{E} \, [\alpha_0 + \frac{\partial \alpha}{\partial Q} \, Q_0 \, \cos(2\pi \, \nu_{vib} t)]. \tag{2.11}$$

Substituting electric field $|\mathbf{E}| = E_0 \cos(2\pi\nu_0 t)$ in this equation results in

$$P = \alpha_0 E_0 \cos(2\pi\nu_0 t) + \frac{\partial \alpha}{\partial Q} \, Q_0 E_0 \cos(2\pi\nu_0 t) \, \cos(2\pi \, \nu_{vib} t). \tag{2.12}$$

Using trigonometric identities, equation (2.12) can be transformed into

$$P = \alpha_0 E_0 \cos(2\pi\nu_0 t) + \frac{\partial \alpha}{\partial Q} \, \frac{Q_0 E_0}{2} [\cos(2\pi(\nu_0 - \nu_{vib})t) + \cos(2\pi \, (\nu_0 + \nu_{vib})t)]. \tag{2.13}$$

The first term of this equation corresponds to Rayleigh scattering while the next two terms are the source of Raman scattering. According to equation (2.13), Raman scattering is an inelastic process where the frequency difference between the incident and scattered light is determined by quantized vibrational modes of the medium. Therefore, unlike Brillouin scattering, changes in the environmental condition of a medium do not affect the frequency of the Raman scattered light. Additionally, equation (2.13) shows that the Raman scattering process occurs only in media where $\partial\alpha/\partial Q$ is non-zero.

The Raman scattering process can also be explained in terms of the energy of the incident light and the energy levels of the molecular vibrational modes, also known as optical phonons. Figure 2.3 illustrates the process for both Raman Stokes and anti-Stokes scattering. In the Stokes scattering process, for instance, an incident photon with energy $h\nu_0$ excites a phonon from energy level $\mathcal{E}_1$ to a virtual energy state $\mathcal{E}_3 = \mathcal{E}_1 + h\nu_0$. If the excited phonon decays to energy state $\mathcal{E}_2$ in return, it emits a photon

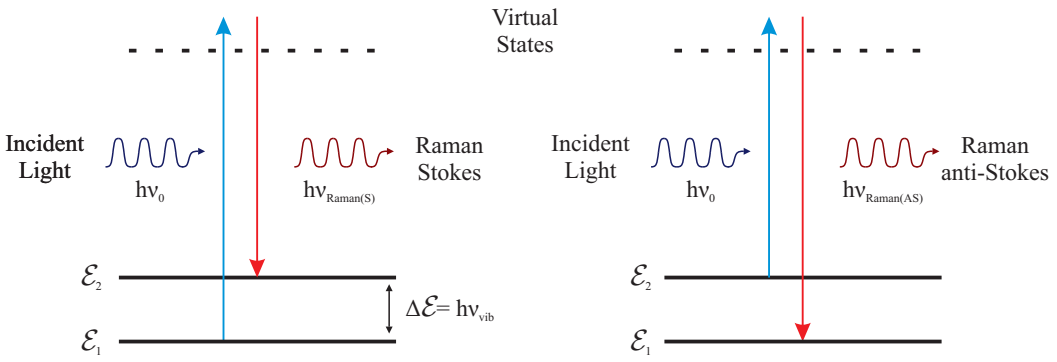

Figure 2.3: Schematic representation of Raman scattering process by means of the energy levels of molecular vibrational modes.

with a lower energy $h(\nu_0 - \nu_{vib})$ and the process is called Raman Stokes scattering. The population density of phonons in both energy levels $\mathcal{E}_1$ and $\mathcal{E}_2$ depends on the temperature of the medium. However, since the population density of higher-energy phonons are more sensitive to the temperature variations than that of lower-energy phonons, the temperature at certain point along an optical fibre can be measured by calculating the ratio of the anti-Stokes power to Stokes power of the backscattered Raman [13]:

$$R(T) = \frac{I_{AS}}{I_S} = (\frac{\lambda_{AS}}{\lambda_S})^4 \exp(-\frac{h\,\Delta\nu}{KT}) \tag{2.14}$$

where λ_{AS} and λ_S are the Raman anti-Stokes and Stokes wavelengths, respectively, and $\Delta\nu$ is the frequency difference between the Raman anti-Stokes and the incident light.

2.2.4 Comparison

Since DOFS are based on one or more of the scattering processes introduced in this section, comparing the properties of backscattered light as a result of these scattering processes can provide a valuable insight of the main advantages and drawbacks of DOFS

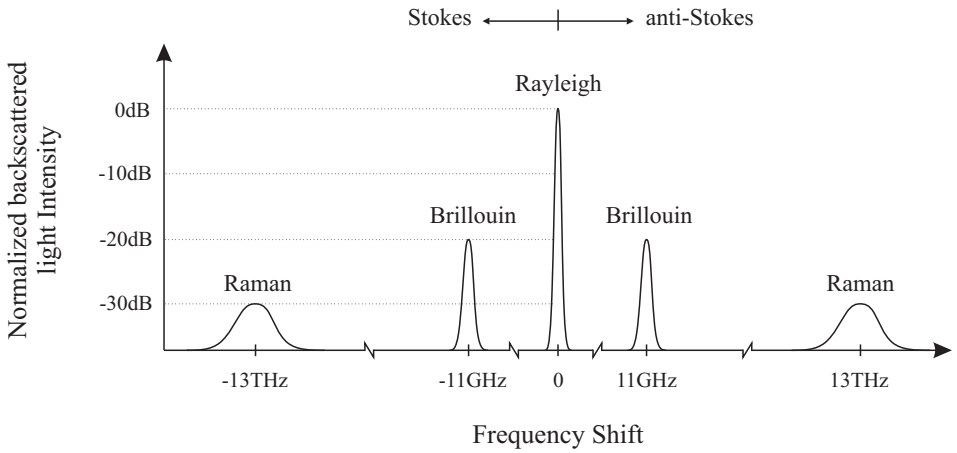

Figure 2.4: Schematic diagram showing a typical spectrum of spontaneous backscattered light in silica fibre for 1550nm incident light [14].

using them. A schematic diagram of a typical spectrum of spontaneous backscattered light in silica fibre for $1550nm$ incident light is shown in figure 2.4. This figure illustrates the frequency shift, bandwidth, and relative intensity of Raman and Brillouin backscattered light in comparison with that of Rayleigh scattering. From this figure, it can be seen that the intensities of Brillouin and Raman backscattered light are $\sim 20dB$ and $\sim 30dB$ weaker than that of Rayleigh backscattered light, respectively. Therefore, DOFS which are based on Brillouin and Raman scattering require a larger amount of averaging in their signal processing procedures to achieve a reasonable signal to noise ratio (SNR) [10–12]. As a result, most of the Brillouin- and Raman-based DOFS are developed as quasi-static distributed temperature or distributed strain sensors.

In addition, figure 2.4 shows that the Raman frequency shift is much larger than that of the Brillouin. Therefore, prior to development of fibre Bragg grating, it was much easier to filter and analyze the Raman backscattered light without any concern for Rayleigh contamination. However, Raman scattering is sensitive to temperature variation only (equation 2.14). On the contrary, Brillouin scattering is an inelastic scattering process which is sensitive to both temperature and strain. Since any variation in temperature or strain of a fibre changes the intensity and frequency of both Brillouin Stokes and anti-Stokes backscattered signals, Brillouin backscattered light can be used to disentangle the temperature variations from strain fluctuations.

Of the three scattering processes, Rayleigh scattering is the most powerful and the only scattering phenomenon which is elastic. Although the coherent nature of Rayleigh backscattered light may not be convenient for mapping the fibre loss along optical fibre cables, coherent Rayleigh backscattering has been widely used as distributed sensors for detection of dynamic disturbances along the sensing fibre. Most of the studies presented in this thesis take advantage of the coherence nature of the coherent Rayleigh backscattered light between two separate regions of the fibre.

The key parameters of spontaneous Raman, Brillouin, and Rayleigh scattering for silica fibre for $1550nm$ incident light are summarized in table 2.2.

2.3 Distributed Optical Fibre Sensing Techniques

DOFS employ different techniques to analyze the backscattered light from the sensing fibre. These techniques can be divided into three main categories; these are including optical time-domain reflectometry (OTDR), optical frequency-domain reflectometry (OFDR), and optical correlation-domain analysis (OCDA).

Optical-Time Domain Reflectometry (OTDR)

OTDR is the simplest form of fibre interrogation technique. This technique is based on launching a pulse of light down one end of the sensing fibre and collecting the backscattered light from the same end. Backscattered light from the sensing fibre forms a trace

	Rayleigh	*Brillouin*	*Raman*
Principle of scattering	*Inhomogeneites*	*Acoustic phonons*	*Optical phonons*
Scattering Process	*Coherent, Elastic*	*Coherent, Inelastic*	*Incoherent, Inelastic*
Gain bandwidth	$= incident\ light$	$\sim 20 - 100MHz$	$\sim 5THz$
Frequency shift	$0Hz$	$11GHz$	$13THz$
Corresponding wavelength shift	$0nm$	$0.09nm$	$104nm$
Comparision with Rayleigh scattering	-	$\sim 20dB\ weaker$	$\sim 30dB\ weaker$
Backscattered power for $10ns$ *pulse with* $1W$ *peak power*	$\sim 100nW$	$1.6nW$	$100pW$

Table 2.2: Key characteristics of Raman, Brillouin, and Rayleigh scattering for silica fibre for $1550nm$ *incident light.*

where the time axis along the trace represents the distance along the sensing fibre. Hartog *et al.* [15] have shown that for an optical pulse with a peak intensity of I_0, the intensity of the backscattered light at the front-end of the fibre is given by

$$I(t) = \frac{1}{2} v_g I_0 \, t_p \, S \, \gamma_S \, exp(-2\gamma \, x) \tag{2.15}$$

where $x = t\, v_g/2$ is the distance from the front-end of the fibre and S is the fraction of capture which, for a step-index fibre, is given by [15]

$$S = \frac{(NA)^2}{4.3\, n^2}. \tag{2.16}$$

The description and typical values of the elements in these equations are given in table 2.3.

OTDR-based DOFS can be further divided based on the scattering processes they rely on and the techniques they use. Rayleigh-based OTDR systems fall into three categories including polarization OTDR (POTDR) which relies on the polarization state of

Symbol	Description	Value
v_g	Group Velocity	$\sim 2 \times 10^8\, m/s$
t_P	Pulse width	-
S	Fraction of capture	2.11×10^{-3}
γ_S	Scattering coefficient	*Depends on the scattering mechanism*
γ	Total attenuation coefficient	$\sim 4.6 \times 10^{-5}$
NA	Numerical aperture	0.14
n	Fibre refractive index	1.46

Table 2.3: The description and typical values of the elements of equations (2.15) and (2.16) for step index standard SMF fibre.

the backscattered Rayleigh, phase OTDR (φ-OTDR) which relies on the phase of the backscattered Rayleigh, and coherent OTDR (COTDR) which relies on the variation in the intensity of the backscattered coherent Rayleigh noise (CRN). It should be mentioned that the operation of POTDR and φ-OTDR techniques relies on the fact that the Rayleigh scattering radiates coherent light.

Since Brillouin scattering is not an elastic process, OTDR techniques which rely on Brillouin scattering differ from that of Rayleigh scattering. Brillouin OTDR (BOTDR) is the simplest form of Brillouin-based DOFS in which the wavelength and the intensity of the spontaneous Brillouin backscattered signal from a pulse of light are used to map the temperature and strain at each point along the sensing fibre [16, 17]. Brillouin optical time domain analysis (BOTDA) is a more complex form of BOTDR which relies on stimulated Brillouin scattering. In this technique, an optical pulse and CW light with frequency difference equivalent to the Brillouin frequency shift are launched at the two opposite ends of the sensing fibre. The interaction between these two waves at the sections of the sensing fibre which meet the Bragg condition results in stimulated Brillouin scattering. Therefore, by scanning the wavelength of either the CW light or the optical pulse over a range of frequencies, the temperature and strain along the sensing fibre can be mapped [18]. Although this technique generates a more powerful backscattered light, it has a number of problems which are discussed in the next section.

Due to the unique properties of Raman scattering, Raman OTDR (ROTDR) is the only Raman scattering-based OTDR which has been thoroughly studied. The principle of the ROTDR technique is similar to that of BOTDR, but instead of Brillouin backscattered light, the intensity of Raman backscattered light is used to map the temperature distribution along the sensing fibre. Since Raman frequency shift does not depend on the environmental condition of the sensing fibre, optical time domain analysis described for BOTDA technique cannot be adopted for Raman scattering.

Optical Frequency-Domain Reflectometry (OFDR)

In the OFDR technique, instead of an optical pulse, a highly monochromatic CW light is used to interrogate the sensing fibre. In the simplest version of this technique, light from a narrow linewidth tunable laser source is coupled to the sensing fibre while its frequency is linearly swept over a range of frequencies. It is shown that by adjusting the sweeping frequency correctly, the entire length of the fibre can be mapped as a function of the frequency of the backscattered light [20]. A more advanced version of the OFDR technique was proposed by Froggatt *et al.* [19] which relies on the relationship between the intensity of the backscattered light as a function of wave number, $\Psi(\beta)$, and the variation in the permittivity of the fibre core as a function of distance along the fibre, $\Delta\varepsilon(x)$. This relationship is given by [19]

$$\Psi(\beta) = \frac{E_0\beta}{2i} \int \frac{\Delta\varepsilon(x)}{\varepsilon} \exp(i\,2\beta x)\,dx \tag{2.17}$$

where β is the wave number, ε is the mean permittivity of the fibre, E_0 is the amplitude of the incident electric wave, and i is the imaginary number. This equation shows that the complex amplitude of the backscattered light at a certain wave number is equal to the spatial Fourier transform of the fluctuations in the permittivity of the fibre as a function of distance evaluated at twice the spatial frequency of the exciting field. Therefore, by measuring the backscattered light as a function of the wave number, the permittivity along the fibre core can be spatially mapped, and any change in it can be used to measure the changes along the fibre. Although the main application of the OFDR technique is in the distributed measurements of the parameters of optical fibres [21, 22], this technique has been used for distributed sensing purposes as well [23, 24].

Optical Correlation-Domain Analysis (OCDA)

Among the three interrogating techniques, OCDA is the most complex one, and can only be applied to Brillouin scattering. The principle of the Brillouin-OCDA (BOCDA) technique is based on the interaction between two counter-propagating CW lights while the wavelengths of the lights are being modulated. The point at which the two lights interact to generate stimulated Brillouin scattering (SBS) can be controlled by adjusting the wavelength-modulation frequency of the two counter-propagating waves as well as their frequency difference. Therefore, by controlling the correlation between the two counter-propagating CW lights, the temperature and strain along the sensing fibre can be mapped one point at a time [25]. The Brillouin optical correlation-domain reflectometry (BOTDR) is another technique which takes advantage of the correlation between the Brillouin backscattered light and reference light. In this technique, wavelength-modulated CW light is divided into pump and reference light. The pump light is injected into the sensing fibre and the Brillouin backscattered light is mixed with the delayed reference light. Similar to the BOCDA technique, the sensing fibre can be mapped by controlling the wavelength-modulation frequency of the source [26].

The tree diagram of figure 2.5 summarises the different interrogation techniques used in DOFS based on the scattering phenomenon they use. In the next chapter, DOFS capable of either detecting or quantifying the dynamic variations or magnetic fields along the sensing fibre are reviewed according to this diagram.

2.4 Distributed Dynamic Strain Sensing: An Overview

2.4.1 Distributed Vibration Sensor Based on Rayleigh Scattering

As mentioned earlier, only Rayleigh and Brillouin scattering processes are sensitive to the induced strain in an optical fibre. Among the Rayleigh-based sensing techniques described in the previous section, three techniques are used in distributed vibration sensors (DVS). The following reviews the main studies in Rayleigh scattering-based DVS and looks at their advantages and drawbacks.

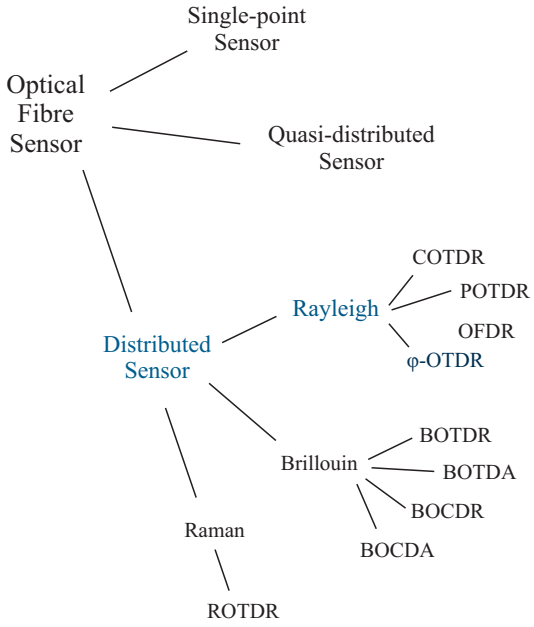

Figure 2.5: Summary of the different interrogation techniques used in DOFS based on the scattering phenomenon that each uses.

COTDR-based Sensor

The simplest form of DVS which was first proposed by Taylor *et al.* [27] is based on COTDR traces. In this technique, the perturbations along the sensing fibre change the distribution of the inhomogeneities within the fibre. The redistribution of inhomogeneities changes the intensity of the coherent Rayleigh backscattered light from which the vibrations are detected. A number of such sensors have been proposed [28–30], with the recent studies demonstrating DVS with frequency and sensing range of $1kHz$ and $2km$ respectively. In addition, a range of commercial devices with a sensing range as long as $50km$ are available which are based on COTDR and are used as an intruder sensor. However, since the redistribution of inhomogeneities in the fibre results in a random variation in the intensity of the backscattered CRN, the DVS using this sensing technique cannot provide a true measure of the magnitude and frequency of the perturbation.

OFDR-based Sensor

Unlike the COTDR-based sensors, DVS which are based on OFDR are capable of quantifying perturbations along the sensing fibre. The sensing mechanism of this technique is based on continuously monitoring the changes in the permitivity of the sensing fibre as a function of distance by the method introduced eariler [19]. Although this technique allows for quantification of perturbations with a high spatial resolution, it has a limited frequency and sensing range. For instance, Zhou *et al.* [31] have demonstrated a sensor with a spatial resolution of $10cm$, but sensing and frequency ranges of $17m$ and $32Hz$,

respectively. In addition, it should be noted that the long-range OFDR-based vibration sensors demonstrated in a number of publications (*e.g.* [24]) are not distributed sensors since, at any given time, they can detect the vibration at one point along the fibre by gating the backscattered light.

φ-OTDR-based Sensor

φ-OTDR has also been used as a sensing technique in a number of distributed vibration sensing systems. The underlying principle of all of the φ-OTDR sensors is based on the relative changes in the phase of the backscattered light from two separate regions of the fibre. In contrast with the intensity of CRN which varies in an unpredictable manner as a result of the external disturbances, changes in the phase difference between two regions of the fibre is a linear function of the separation between them. Therefore, vibrations between two regions along the fibre can be quantified by monitoring the variation in the phase of the backscattered light from those regions.

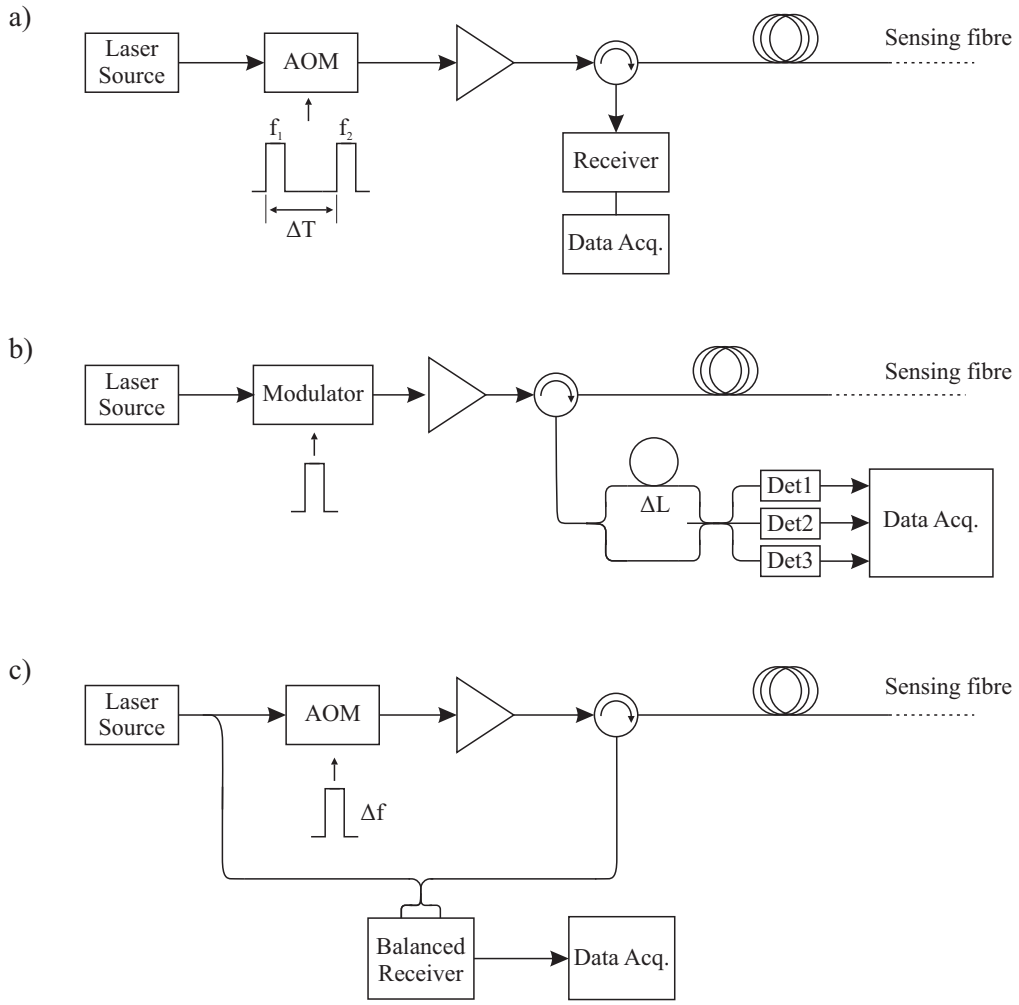

Figure 2.6: The outline of the experimental setups of three DVS, the operations of which are based on φ-OTDR.

Utilization of φ-OTDR as an DVS was first proposed by Dakin *et al.* [32]. The operation of the proposed sensor was based on launching a pair of optical pulses of slightly different frequency, separated by time ΔT, into the sensing fibre and measuring the phase difference between two separate regions of the fibre by mixing the two backscattered traces at the photodetector (figure 2.6(a)). The frequency difference of the two pulses results in a signal with beat frequency of $\Delta f = \mid f_1 - f_2 \mid$where the phase of this signal represents the differential phase between the two regions of the sensing fibre separated by distance $\Delta z = \Delta T.c/2n$ where c is the speed of light in vacuum and n is the group refractive index of fibre. Although, in theory, the proposed concept can provide the phase information along the sensing fibre, in practice, for the setup to work, a precise control over the phase of the two interrogating pulses is required. Therefore, this system cannot be practically implemented.

In the year 2000, Posey *et al.* [33] demonstrated an alternative measurement technique in which the relative phase of the backscattered light between two locations in the sensing fibre was measured using an imbalanced Mach-Zehnder interferometer (MZI) to monitor $2kHz$ dynamic strain along $400m$ of sensing fibre (figure 2.6(b)). In the proposed technique, the backscattered light from a single pulse is launched into two unequal paths to provide two similar traces with temporal shift of $\Delta T = \Delta L.n/c$ where ΔL is the path imbalance. Afterward, the two traces are mixed in a 3×3 coupler to provide three electromagnetic wave with a nominal phase-shift of 120° between them. It was shown that the differential phase information at a certain section of the sensing fibre can be extracted by gating the signals at the outputs of the three photodetectors and demodulating the signal using a differentiate and cross-multiply demodulator. Farhadiroushan *et al.* [34] later modified this technique to develop a DVS capable of detecting perturbations along the sensing fibre simultaneously. However, using this technique, their proposed scheme has a minimum detectable frequency of over $100kHz$ according to the specification of the commercial products. The reason for this limitation is the demodulation process of the technique which relies on the derivative of the backscattered trace as a function of distance.

Another technique proposed by Hartog *et al.* [35] measures the phase difference between two segments of the sensing fibre in an electrical domain (figure 2.6(c)). In this technique, an acousto-optic modulator (AOM) is used to generate optical pulses with a frequency shift of Δf relative to the input CW light. The backscattered light from the fibre is mixed with the CW light from the laser source at a balanced photodetector to provide a beat signal which retains both the amplitude and phase information. The phase information along the fibre is then measured in the electrical domain by a phase detection circuit. However, the analysis of this approach shows that the fluctuations in the intensity of the backscattered traces (also know as CRN) introduce noise to the phase measurement since the phase detection mechanism cannot distinguish between intensity and phase variation. Therefore, this technique cannot provide an accurate measurement of the amplitude of vibration.

POTDR

There was no study found on the utilization of the POTDR technique as DVS. Studies suggesting such an approach were either not entirely based on the polarization of the backscattered light (such as [36,37] which rely on both the intensity and the polarization of the backscattered light) or they were not distributed sensors at all (such as Liu *et al.* [38] which demonstrated a sensor capable of detecting a single perturbation along the sensing fibre).

2.4.2 Distributed Vibration Sensor Based on Brillouin Scattering

As previously noted, Brillouin is a weak scattering process in comparison with Rayleigh scattering. Therefore, most of the studies on Brillouin-based DVS are based on stimulated Brillouin sensing techniques (*i.e.* BOCDA and BOTDA) which provide a stronger backscattered signal. With a more powerful signal, less averaging time is required and, as a result, Brillouin sensing techniques can be used as distributed vibration sensors. Following is a review of the DVS which rely on BOCDA and BOTDA in their sensing mechanism.

BOCDA

One of the first studies of Brillouin-based dynamic strain measurement was introduced in 2003 by Hotate *et al.* [39] in which the BOCDA technique was used to interrogate a short-range sensing fibre. With a short sensing range, the frequency sweeping rate of the BOCDA was increased to form a high spatial resolution distributed dynamic strain sensor capable of quantifying dynamic strains with an accuracy of $\pm 38\mu\varepsilon$. In 2011, a more advanced version of this technique was introduced by the same research group [40] offering specifications such as a sampling rate of $20Hz$ and a strain accuracy of $\pm 50\mu\varepsilon$ over a $100m$ sensing fibre. However, since the BOCDA interrogation technique is a slow process, DVS based on this technique have a limited frequency and sensing range. Although the sensing range can be increased, there is a trade-off between the sensing range and the spatial resolution in the sensors which are based on this technique. Therefore, this technique is not suitable for measurement of the dynamic vibrations over a long sensing range.

BOTDA

The Brillouin optical time-domain analysis (BOTDA) technique has also been used for distributed dynamic sensing. Bernini *et al.* [41] were the first to experimentally demonstrate a DVS based on this technique. In their approach, the range of the sensing fibre was reduced to $100m$ to allow for a higher interrogation rate and, consequently, measurement of dynamic disturbances along the fibre. Recent studies on this technique

have demonstrated a scheme with an effective sampling rate of less than $2kHz$ and a spatial resolution of $1m$ over a sensing range of $160m$ [42, 43].

The BOTDA sensing technique, however, suffers from two main drawbacks. The first problem is the trade-off between the sensing and frequency range of the sensor. BOTDA is a slow sensing process similar to BOCDA which requires the scanning of the whole length of the sensing fibre in small frequency steps. Therefore, the frequency range of the BOTDA-based sensors is at best limited to few tens of hertz. On the other hand, the BOTDA sensing technique is best reserved for monitoring single disturbances in the sensing fibre with relatively high strains where the strain-induced shift in the Brillouin frequency relative to the unstrained fibre is greater than the Brillouin linewidth. If not, the apparent Brillouin gain spectrum at a point from which the strain is computed is influenced by the strain distribution along the fibre. This effect, first identified by Horiguchi *et al.* [44] and later analyzed by Geinitz *et al.* [45], is due to the potential transfer of power between the CW pump light and counter-propagating interrogating pulse all along the fibre from the point where the pulse enters the fibre to the point of measurement.

2.4.3 Distributed Dynamic Magnetic Field Sensor

Distributed optical fibre magnetic-field sensors (DOFMS) are based on monitoring the variation in either the polarization or the phase of the backscattered light from the sensing fibre. DOFMS which are based on the polarization of the backscattered light exploit the Faraday effect phenomenon, a magneto-optical phenomenon which causes the rotation of the plane of polarization of the light propagating inside the fibre as a function of the magnetic field. The theoretical principles of this sensor were first elucidated back in 1981 by Rogers [46] and referred to as polarization optical time domain reflectometry (POTDR). In 2012, experimental results of a state of the art DOFMS were published by Palmieri *el at.* [47] which uses polarization optical frequency domain reflectometry (POFDR) for magnetic field detection. Despite its wide intensity range ($1.5T$), the proposed sensor has a number of limitations including the sensitivity of $100mT$ (which is due to the weak nature of the Faraday effect), the spatial range of $15m$, and repetition rate of $10s$ which makes it suitable only for DC and quasi-DC magnetic field sensing.

Previously reported magnetostrictive-based optical fibre magnetic field sensors are based on coupling an optical fibre to a magnetostrictive material and measuring the magnetic field by monitoring the strain induced on the fibre. Although this technique has been successfully used to develop point sensors using MZI [48–50] as well as quasi-distributed sensor using fibre Bragg gratings (FBG) [51–53], it has never been employed to develop a DOFMS.

2.5 Conclusions

In this chapter, the physical principles of Rayleigh, Brillouin, and Raman scattering were introduced. It was shown that DOFS use techniques including time-domain reflectometry, frequency-domain reflectometry, or correlation-domain analysis to interrogate the sensing fibre. After a brief introduction to the working principles of these techniques, DOFS capable of detecting the dynamic variation of strain and magnetic fields along the sensing fibre were reviewed. OFDR- and BOCDR- based sensors capable of quantifying multiple dynamic strain disturbances were described and it was shown that DOFS based on these techniques have a limited frequency and sensing range. On the other hand, a number of long-range DOFS were reviewed which are capable of detecting, but not quantifying, dynamic disturbances along the sensing fibre.

In the next chapter, a DOFS is introduced which is based on φ-OTDR and is capable of quantifying and tracking multiple dynamic perturbations over a large frequency and sensing range.

Bibliography

[1] K.T.V. Grattan and T. Sun, "Fiber optic sensor technology: an overview," Sensors and Actuators A: Physical, vol. 82, pp. 40-61, 2000.

[2] A. Rogers, "Distributed optical-fibre sensing," Measurement Science and Technology, vol. 10, pp. 75-99, 1999.

[3] B. J. Berne and R. Pecora, Dynamic Light Scattering: With Applications to Chemistry, Biology, and Physics, Ed. New York: Dover Publications, Unabridged edition, 2000.

[4] I. L. Fabelinskii, Molecular Scattering of Light, Ed. New York: Springer, 1968.

[5] T. Still, "Basics and Brillouin Light Scattering," in High Frequency Acoustics in Colloid-Based Meso- and Nanostructures by Spontaneous Brillouin Light Scattering, Germany: Springer Thesis, pp. 9-34 ,2010.

[6] J. Shcroeder, R. Mohr, P. B. Macedo, and C. J. Montrose, "Rayleigh and Brillouin Scattering in $K_2O - SiO_2$ Glasses," 74th Annual Meeting, The American Ceramic Society, Washington DC, May 10, 1972.

[7] S. M. Maughan, H. H. Kee, and T. P. Newson, "Simultaneous distributed fibre temperature and strain sensor using microwave coherent detection of spontaneous Brillouin backscatter," Measurement Science and Technology, vol. 12, pp. 834–842, 2001.

[8] M. N. Alahbabi, N. P. Lawrence, Y. T. Cho, and T. P. Newson, "High spatial resolution microwave detection system for Brillouin-based distributed temperature and strain sensors," Measurement Science and Technology, vol. 15, 1539-1543, 2004.

[9] D. A. Long, "The Raman Effect: A Unified Treatment of the Theory of Raman Scattering by Molecules," John Wiley&Sons, West Sussex, England, 2002.

[10] M. Belal and T. P. Newson, "Enhanced performance of a temperature-compensated submeter spatial resolution distributed strain sensor," IEEE Photonics Technology Letters, vol. 22, pp. 1705-1707, 2010.

[11] M. N. Alahbabi, Y. T. Cho, and T. P. Newson, "Simultaneous temperature and strain measurement with combined spontaneous Raman and Brillouin scattering," Optics Letters, vol. 30, pp. 1276-1278, 2005.

[12] K.de Souza and T. P. Newson, "Signal to noise and range enhancement of a Brillouin intensity based temperature sensor" Optics Express, vol.12, pp. 2656-2661, 2004.

[13] J. P. Dakin, "Multiplexed and distributed optical fibre sensor systems," Journal of Physics E: Scientific Instrumennts, vol. 20, pp. 954-967, 1987.

[14] X. Zhou, Q. Yu, and W. Peng, "Simultaneous measurement of down-hole pressure and distributed temperature with a single fiber," Measurement Science and Technology, vol. 23, 085102, 2012.

[15] A. Hartog and M. P. Gold, "On the theory of backscattering in single-mode optical fibers," Journal of Lightwave Technology, vol. 2, pp. 76-82, 1984.

[16] M. N. Alahbabi, Y. T. Cho, and T. P. Newson, "Long-range distributed temperature and strain optical fibre sensor based on the coherent detection of spontaneous Brillouin scattering with in-line Raman amplification," Measurement Science and Technology, vol. 17, pp. 1082-1090, 2006.

[17] M. N. Alahbabi, Y. T. Cho, and T.P.Newson, "Comparison of the methods for discriminating temperature and strain in spontaneous Brillouin-based distributed sensors," Optics Letters, vol.29, pp. 26-28, 2004.

[18] T. Kurashima, T. Horiguchi, and M. Tateda, "Distributed-temperature sensing using stimulated Brillouin scattering in optical silica fibers," Optics Letters, vol. 15, pp. 1038-1040, 1990.

[19] M. Froggatt and J. Moore, "High-Spatial-Resolution Distributed Strain Measurement in Optical Fiber with Rayleigh Scatter," Applied Optics, vol. 37, pp. 1735-1740, 1998.

[20] W. Eickhoff and R. Ulrich, "Optical frequency domain reflectometry in single-mode fiber," Applied Physics Letters, vol. 39, pp. 693-695 , 1981.

[21] M. Wegmuller, M. Legre, and N. Gisin, "Distributed Beatlength Measurement in Single-Mode Fibers With Optical Frequency-Domain Reflectometry," Journal of Lightwave Technology, vol. 20, pp. 800-807 ,2002.

[22] U. Glombitza and E. Brinkmeyer, "Coherent frequency domain reflectomtry for charactization of single-mode integrated optical waveguides," Journal of Lightwave Technology, vol. 11, pp. 1377-1384 ,1993.

[23] M. Froggatt and J. Moore, "High-Spatial-Resolution Distributed Strain Measurement in Optical Fiber with Rayleigh Scatter," Applied Optics, vol. 37,, pp. 1735-1740, 1998.

[24] Z. Ding, X. S. Yao, T. Liu, Y. Du, K. Liu, Q. Han, Z. Meng, and H. Chen, "Long-range vibration sensor based on correlation analysis of optical frequency-domain reflectometry signals," Optics Express, vol. 20, pp. 28319-28329, 2012.

[25] K. Hotate, and M. Tanaka, "Distributed fiber Brillouin strain sensing with 1-cm spatial resolution by correlation-based continuous-wave technique," IEEE Photonics Technology Letters, vol. 14, pp. 197-199, 2002.

[26] Y. Mizuno, W. Zou, Z. He, and K. Hotate, "Proposal of Brillouin optical correlation-domain reflectometry (BOCDR)," Optics Express, vol. 16, pp. 12148-12153, 2008.

[27] H. F. Taylor and C. E. Lee, "Apparatus and method for fiber optic intrusion sensing," U.S. patent 5 194 847 A, March 16, 1993.

[28] S. V. Shatalin, V. N. Treschikov, and A. J. Rogers, "Interferometric Optical Time-Domain Reflectometry for Distributed Optical-Fiber Sensing," Applied Optics, vol. 37, pp. 5600-5604, 1998.

[29] J. C. Juarez and H. F. Taylor, "Field test of a distributed fiber-optic intrusion sensor system for long perimeters," Applied Optics, vol. 46, pp. 1968-1971, 2007.

[30] Y. Lu, T. Zhu, L. Chen, and X. Bao, "Distributed Vibration Sensor Based on Coherent Detection of Phase-OTDR," Journal of Lightwave Technology, vol. 28, pp. 3243-3249, 2010.

[31] D. Zhou, Ze. Qin, W. Li, L. Chen, and X. Bao, "Distributed vibration sensing with time-resolved optical frequency-domain reflectometry," Optics Express, vol. 20, pp. 13138-13145, 2012.

[32] J. P. Dakin and C. Lamb, "Distributed fibre optic sensor system," GB patent 2 222 247A, February 28, 1990.

[33] R. Posey, G. A. Johnson, and S. T. Vohra, "Strain sensing based on coherent Rayleigh scattering in an optical fibre," Electronics Letters, vol. 36, pp. 1688-1689, 2000.

[34] M. Farhadiroushan, T. R. Parker, and S. Shatalin, "Method and apparatus for optical sensing," US patent application 2012/0060615 A1, March 15, 2012.

[35] A. H. Hartog and K. Kader, "Distributed fiber optic sensor system with improved linearity," US patent application 2012/0067118 A1, March 22, 2012.

[36] Z. Zhang and X. Bao, "Distributed optical fiber vibration sensor based on spectrum analysis of Polarization-OTDR system," Optics Express, vol. 16, pp. 10240-10247, 2008.

[37] N. Linze, P. Megret, and M. Wuilpart, "Development of an Intrusion Sensor Based on a Polarization-OTDR System," IEEE Sensors Journal, vol. 12, pp. 3005-3009, 2012.

[38] J. Liu, J. Yu, J. Guo, C. Gao, W. Wang, and E. Yang, "Distributed optical fiber vibration sensing system based on polarization detection Optoelectronics Letters, vol. 7, p. 458-462, 2011.

[39] K. Hotate and S. S. L. Ong, "Distributed dynamic strain measurement using a correlation-based Brillouin sensing system," IEEE Photonics Technology Letters, vol. 15, pp. 272-274, 2003.

[40] K. Y. Song, M. Kishi, Z. Y. He, and K. Hotate, "High-repetition-rate distributed Brillouin sensor based on optical correlation-domain analysis with differential frequency modulation," Optics Letters, vol. 36, pp. 2062-2064, 2011.

[41] R. Bernini, A. Minardo, and L. Zeni, "Dynamic strain measurement in optical fibers by stimulated Brillouin scattering," Optics Letters, vol. 34, pp. 2613-2615, 2009.

[42] Y. Peled, A. Motil, and M. Tur, "Fast Brillouin optical time domain analysis for dynamic sensing," Optics Express, vol. 20, pp. 8584-8591, 2012.

[43] J. Urricelqui, A. Zornoza, M. Sagues, and A. Loayssa, "Dynamic BOTDA measurements based on Brillouin phase-shift and RF demodulation," Optics Express, vol. 20, pp. 26942-26949, 2012.

[44] T. Horiguchi, K. Shimizu, T. Kurashima, M. Tateda, and Y. Koyamada, "Development of a Distributed Sensing Technique Using Brillouin-Scattering," Journal of Lightwave Technology, vol. 13, pp. 1296-1302, 1995.

[45] E. Geinitz, S. Jetschke, U. Ropke, S. Schroter, R. Willsch, and H. Bartelt, "The influence of pulse amplification on distributed fibre-optic Brillouin sensing and a method to compensate for systematic errors," Measurement Science and Technology, vol. 10, pp. 112-116, 1999.

[46] A. J. Rogers, "Polarization-optical time domain reflectometry: a technique for the measurement of field distributions," Applied Optics, vol. 20, pp. 1060-1074, 1981.

[47] L. Palmieri and A. Galtarossa, "Distributed fiber optic sensor for mapping of intense magnetic fields based on polarization sensitive reflectometry," Proceedings of SPIE vol. 8351, 835131, 2012.

[48] S. C. Rashleigh, "Magnetic-field sensing with a single-mode fiber," Optics Letters, vol. 6, pp. 19-21, 1981.

[49] M. Sedlara, V. Matejeca, and I. Paulickab, "Optical fibre magnetic field sensors using ceramic magnetostrictive jackets," Sensors and Actuators A: Physical, vol 84, pp. 297-302, 2000.

[50] A. Yariv and H. V. Winsor, "Proposal for detection of magnetic fields through magnetostrictive perturbation of optical fibers," Optics Letters, vol. 5, pp. 87-89, 1980.

[51] P. M. Cavaleiro, F. M. Araujo, and A. B. L. Ribeiro, "Metal-coated fibre Bragg grating sensor for electric current metering," Electronics Letters, vol. 34, pp. 1133-1135, 1998.

[52] C. Shi, J. Chen, G. Wu, X. Li, J. Zhou, and F. Ou, "Stable dynamic detection scheme for magnetostrictive fiber-optic interferometric sensors," Optics Express, vol. 14, pp. 5098-5102, 2006.

[53] M. Yang, J. Dai, C. Zhou, and D. Jiang, "Optical fiber magnetic field sensors with TbDyFe magnetostrictive thin films as sensing materials," Optics Express, vol. 17, pp. 20777-20782, 2009.

Chapter 3

Dynamic Strain Sensor Based on Coherent Rayleigh Scattering

3.1 Introduction

Brillouin-based DOFS have been established as standard tools for measuring the distribution of physical quantities such as temperature and strain [1–6]. Despite their capability of measuring DC and quasi-DC changes in strain and temperature, Brillouin-based DOFS have not been used for long-range dynamic measurements of such quantities since their sensing mechanism requires a lot of averaging. This high averaging requirement is due to the weak nature of the Brillouin scattering as illustrated in table 2.2.

Distributed dynamic strain sensing has most successfully been explored using coherent Rayleigh scattering [7]. In this technique, an induced strain causes a change in the coherent Rayleigh noise of the backscattered trace from which the location of the perturbation can be spatially located. However, it was shown in the previous chapter that this technique cannot provide a measure of the magnitude of strain-induced perturbation. An OTDR system based on the phase of the coherent Rayleigh noise, first proposed by Posey *et al.* [8], provided a means to quantify the strain at a single section of the fibre at any one time. This chapter builds on this work, utilizing the same proposed phase demodulation scheme but capturing the entire backscattered trace which allows for a true measurement of distributed dynamic strain along the sensing fibre. The advantage of this technique lies in its ability to quantify and track multiple disturbances along the fibre.

The underlying principles of the proposed scheme are detailed in section 3.2, followed by a description of the experimental layout in section 3.3. Experimental results including the 3D plot of the sensing fibre under strain are presented in section 3.4. Discussion and analysis of the experimental results are presented in section 3.5 and the final section highlights the outcome of the study.

3.2 Principles

3.2.1 $\varphi - OTDR$ principles

The basic principle governing the operation of the dynamic strain sensor is based on measuring the relative phase variation of the backscattered Rayleigh light between two segments of the sensing fibre due to induced strain. The relative phase difference between the backscattered lights from the two segments of the fibre, $\Delta\phi$, is a function of the distance between the two segments, L, as shown in figure 3.1. In the absence of any strain perturbations, the value of L changes at low frequency due to ambient temperature variation. In the presence of an external perturbation, however, the value of L changes as a function of the frequency and magnitude of the induced strain due to that perturbation. Therefore, the value of the distance between the two segments of the fibre can be written as

$$L(t) = L_0 + \Delta L(t) \tag{3.1}$$

where ΔL denotes the changes in L due to external perturbations and L_0 is the stationary distance between the two segments.

The changes in the separation length between the two segments of the fibre results in a change in the phase difference between the backscattered light from those segments. The changes in the phase difference between the two segments is measured using a Mach-Zehnder fibre interferometer (MZI). The measurement procedure relies on launching a

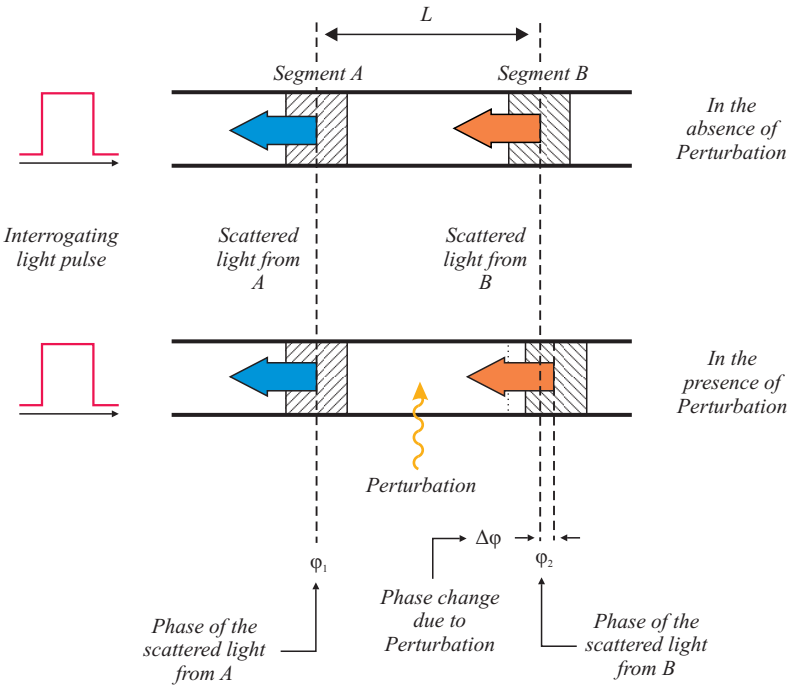

Figure 3.1: Principle of the dynamic strain sensing using φ-OTDR. This figure shows the graphical representation of two groups of scatterers in a section of the sensing fibre (a) before external perturbation, and (b) after external perturbation.

short pulse of light into the sensing fibre and feeding the backscattered coherent Rayleigh light into an imbalanced MZI (IMZI) with a path-imbalance $\triangle\ell$. The role of the path-imbalance in the MZI is to add delay to the backscattered light propagating in the longer arm of the MZI relative to the light travelling in the shorter arm, therefore mixing the phase of the backscattered light from two separate segments of the sensing fibre. Therefore, the path-imbalance, $\triangle\ell$, determines the spatial resolution of the sensor. For a spatial resolution of L_0 metres, the relationship between the path-imbalance and the separation between the two segments should be $\Delta\ell = 2L_0$.

Figure 3.1 explains the principle of operation of an imbalanced MZI. Two segments shown in this figure (A and B) represent two segments on the sensing fibre, L metres apart. As a result of the path-imbalance of the MZI, the backscattered electric field from the segment A which travels through the longer arm of the MZI (the arm with the delay fibre) mixes with the backscattered electric field from segment B which travels through the shorter arm of the MZI. Neglecting the fibre loss along L, these electric fields can be written as

$$\begin{aligned} E_A &= E_0 \exp[i(\omega t + \varphi_1)] \\ E_B &= E_0 \exp[i(\omega t + \varphi_2)] \end{aligned} \tag{3.2}$$

where φ_1 and φ_2 are the phases of the backscattered light from A and B respectively, ω is the angular frequency of the backscattered light, and E_0 is the magnitude of the electric field of the backscattered light. As a result of the optical path-imbalance of the MZI, the backscattered electric field E_A is delayed and mixes with the backscattered electric field E_B. Therefore, the intensity of the combined electric fields at the output of the MZI is given by

$$\begin{aligned} I_{det} &= (E_A|_{delayed} + E_B)(E_A|_{delayed} + E_B)^* \\ &= (E_A \exp[i(\frac{2\pi}{\lambda}\Delta\ell)] + E_B)(E_A \exp[i(\frac{2\pi}{\lambda}\Delta\ell)] + E_B)^* \qquad (3.3) \\ &= 2E_0^2\,[1 + \cos[(\varphi_1 + \frac{2\pi}{\lambda}\Delta\ell) - \varphi_2]]. \qquad (3.4) \end{aligned}$$

The phase-difference between $E_A|_{delayed}$ and E_B (*i.e.* the electric field at the end of the two arms of the MZI) can be written as

$$\begin{aligned} \Delta\phi = (\varphi_1 + \tfrac{2\pi}{\lambda}\Delta\ell) - \varphi_2 &= (\Phi + \tfrac{2\pi}{\lambda}\Delta\ell) - (\Phi + \tfrac{2\pi}{\lambda}2L) \\ &= \tfrac{2\pi}{\lambda}(\Delta\ell - 2L) \end{aligned} \tag{3.5}$$

where Φ is a random phase and λ is the wavelength of the backscattered light. Since $\Delta\ell = 2L_0$, substituting equation (3.1) into (3.5) gives

$$\Delta\phi = \frac{2\pi}{\lambda}(\Delta\ell - 2L_0 - 2\Delta L) = -\frac{2\pi}{\lambda}(2\Delta L). \tag{3.6}$$

Finally, substituting equation (3.6) in (3.4) gives

$$\begin{aligned} I_{det} &= 2E_0^2\,[1+\cos(\Delta\phi)] \\ &= 2E_0^2\,[1+\cos(\frac{4\pi}{\lambda}\,\Delta L)]. \end{aligned} \tag{3.7}$$

Equation (3.7) shows that the detected intensity depends on the cosine of the phase difference between the backscattered light from the two segments. Therefore, any external disturbances (e.g. acoustic vibration) within the gauge length which affect the separation of the two segments will change the intensity at the output of the MZI.

3.2.2 Principles of Signal Fading Elimination

According to equation (3.7), variation in the output of the photodetector is a function of ΔL. However, for $\Delta L = \lambda/4n$ $(n = 1, 2, 3, ...)$, the value of the cosine function reaches its extremum and, consequently, the sensitivity of the sensor reaches zero. This phenomenon is known as signal fading in interferometers [9]. Among the different optical techniques which have been demonstrated to solve the signal fading problem [10], a passive technique based on directional 3×3 fibre coupler was adopted. In this technique, the 3dB coupler at the output end of the MZI is replaced by a symmetrical 3×3 fibre coupler as shown in figure 3.2.

The operation of a MZI utilizing 3×3 fibre coupler was analyzed by Priest *et al.* [11] using transfer matrices of the components forming the interferometer. The same procedure is employed here to analyze the operation of an IMZI with a 3×3 coupler at the output end. In principle, the operation the IMZI shown in figure 3.2 can be described in terms of the product of transfer matrices in the form of

$$\underbrace{\begin{bmatrix} E_1 \\ E_2 \\ E_3 \end{bmatrix}}_{E_{out}} = \underbrace{\begin{bmatrix} \mathbf{b_{11}} & \mathbf{b_{12}} & \mathbf{b_{13}} \\ \mathbf{b_{21}} & \mathbf{b_{22}} & \mathbf{b_{23}} \\ \mathbf{b_{31}} & \mathbf{b_{32}} & \mathbf{b_{33}} \end{bmatrix}}_{M_3} \underbrace{\begin{bmatrix} 0 & 0 & 0 \\ 0 & e^{i\Delta\phi} & 0 \\ 0 & 0 & 1 \end{bmatrix}}_{M_{Delay}} \underbrace{\begin{bmatrix} 0 & 0 & 0 \\ 0 & \mathbf{a_{11}} & \mathbf{a_{12}} \\ 0 & \mathbf{a_{21}} & \mathbf{a_{22}} \end{bmatrix}}_{M_2} \underbrace{\begin{bmatrix} 0 \\ E_{in} \\ 0 \end{bmatrix}}_{E_{in}} \tag{3.8}$$

where M_2 and M_3 are the transfer matrices of the 2×2 and 3×3 couplers respectively,

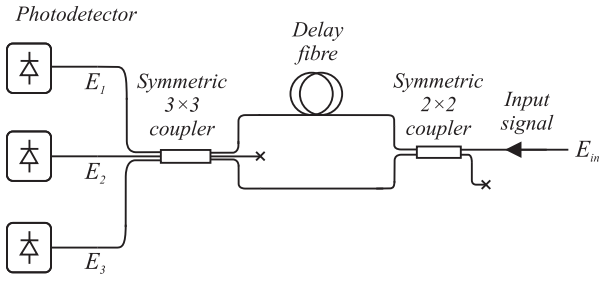

Figure 3.2: Schematic of the setup used to eliminate signal fading in the interferometer by using a symmetric 3×3 coupler at the output of the interferometer.

$\Delta\phi$ is the phase difference between the two arms due to path-imbalance, and E_{in} and E_{out} are the column vectors specifying the electric fields at the input and output of the IMZI. Zero row and column are added to the M_2 matrix to allow for integration of a 2×2 coupler with a 3×3 coupler.

Generally, the elements of the transfer matrix of couplers are complex numbers which are determined by the properties of the couplers. However, for a symmetrical 2×2 coupler, it is shown that [11]

$$\mathbf{a_{11}} = \mathbf{a_{12}} = \mathbf{a_{21}} = -\mathbf{a_{22}} = \frac{1}{\sqrt{2}},$$

while, for a symmetrical 3×3 coupler, the square of the modulus of its transfer matrix elements is shown to be equal to 1/3. Therefore, the product transfer matrix of an IMZI composed of symmetrical couplers is given by

$$\begin{bmatrix} E_1 \\ E_2 \\ E_3 \end{bmatrix} = \frac{1}{\sqrt{3}} \begin{bmatrix} e^{i\angle\mathbf{b_{11}}} & e^{i\angle\mathbf{b_{12}}} & e^{i\angle\mathbf{b_{13}}} \\ e^{i\angle\mathbf{b_{21}}} & e^{i\angle\mathbf{b_{22}}} & e^{i\angle\mathbf{b_{23}}} \\ e^{i\angle\mathbf{b_{31}}} & e^{i\angle\mathbf{b_{32}}} & e^{i\angle\mathbf{b_{33}}} \end{bmatrix} \begin{bmatrix} 0 & 0 & 0 \\ 0 & e^{i\Delta\phi} & 0 \\ 0 & 0 & 1 \end{bmatrix} \begin{bmatrix} 0 & 0 & 0 \\ 0 & \frac{1}{\sqrt{2}} & \frac{1}{\sqrt{2}} \\ 0 & \frac{1}{\sqrt{2}} & \frac{-1}{\sqrt{2}} \end{bmatrix} \begin{bmatrix} 0 \\ E_{in} \\ 0 \end{bmatrix} \tag{3.9}$$

where $\angle\mathbf{b_{ij}}$ is the angle of the $\mathbf{b_{ij}}$ phasor. The product of the transfer matrices in equation (3.9) gives

$$\begin{bmatrix} E_1 \\ E_2 \\ E_3 \end{bmatrix} = \begin{bmatrix} \frac{1}{\sqrt{6}} E_{in}\, e^{i(\Delta\phi+\angle\mathbf{b_{12}})} + \frac{1}{\sqrt{6}} E_{in}\, e^{i(\angle\mathbf{b_{13}})} \\ \frac{1}{\sqrt{6}} E_{in}\, e^{i(\Delta\phi+\angle\mathbf{b_{22}})} + \frac{1}{\sqrt{6}} E_{in}\, e^{i(\angle\mathbf{b_{23}})} \\ \frac{1}{\sqrt{6}} E_{in}\, e^{i(\Delta\phi+\angle\mathbf{b_{32}})} + \frac{1}{\sqrt{6}} E_{in}\, e^{i(\angle\mathbf{b_{33}})} \end{bmatrix}. \tag{3.10}$$

The intensity of the electric fields at the output arms of the IMZI can be calculated by multiplying the electric field of each arm with its complex conjugate. Therefore, the intensity of the output arms of the IMZI is given by

$$\begin{aligned} I_1 &= E_1 E_1^* = \frac{1}{3} I_0 + \frac{1}{6} I_0\, m[e^{i(\Delta\phi+\angle\mathbf{b_{12}}-\angle\mathbf{b_{13}})} + e^{-i(\Delta\phi+\angle\mathbf{b_{12}}-\angle\mathbf{b_{13}})}] \\ I_2 &= E_2 E_2^* = \frac{1}{3} I_0 + \frac{1}{6} I_0\, m[e^{i(\Delta\phi+\angle\mathbf{b_{22}}-\angle\mathbf{b_{23}})} + e^{-i(\Delta\phi+\angle\mathbf{b_{22}}-\angle\mathbf{b_{23}})}] \\ I_3 &= E_3 E_3^* = \frac{1}{3} I_0 + \frac{1}{6} I_0\, m[e^{i(\Delta\phi+\angle\mathbf{b_{32}}-\angle\mathbf{b_{33}})} + e^{-i(\Delta\phi+\angle\mathbf{b_{32}}-\angle\mathbf{b_{33}})}] \end{aligned} \tag{3.11}$$

where $I_0 = (E_0)^2$ and m is a parameter which determines the state of polarization between the two arms of the IMZI ($0 < m < 1$). Using Euler's formula, equation (3.11) becomes

$$\begin{aligned} I_1 &= \frac{1}{3} I_0[1 + m\cos(\Delta\phi + \angle\mathbf{b_{12}} - \angle\mathbf{b_{13}})] \\ I_2 &= \frac{1}{3} I_0[1 + m\cos(\Delta\phi + \angle\mathbf{b_{22}} - \angle\mathbf{b_{23}})] \\ I_3 &= \frac{1}{3} I_0[1 + m\cos(\Delta\phi + \angle\mathbf{b_{32}} - \angle\mathbf{b_{33}})]. \end{aligned} \tag{3.12}$$

Another important feature of a symmetrical 3×3 coupler is the $2\pi/3$ phase difference between the output of its three arms. Therefore, if $\angle\mathbf{b_{12}} - \angle\mathbf{b_{13}} = \theta$, it can be shown that

$$\begin{aligned} \angle\mathbf{b_{22}} - \angle\mathbf{b_{23}} &= \theta + 2\pi/3 \\ \angle\mathbf{b_{32}} - \angle\mathbf{b_{33}} &= \theta - 2\pi/3. \end{aligned} \tag{3.13}$$

Without the loss of essential generality, it can be assumed that $\theta = 0$. Therefore, substituting equation (3.13) into (3.12) gives

$$\begin{aligned} I_1 &= \frac{1}{3} I_0[1 + m\cos(\Delta\phi)] \\ I_2 &= \frac{1}{3} I_0[1 + m\cos(\Delta\phi + \frac{2\pi}{3})] \\ I_3 &= \frac{1}{3} I_0[1 + m\cos(\Delta\phi - \frac{2\pi}{3})]. \end{aligned} \tag{3.14}$$

According to this equation, the output intensities of the IMZI shown in figure 3.2 are functions of the phase difference between the two arms and the output of each arm is $2\pi/3$ out of phase with respect to the output of the other two arms. As a result, for any given $\Delta\phi$, the output intensities of at least two output arms of the IMZI are not at their stationary points (figure 3.3). Therefore, signal fading can be avoided by monitoring the outputs of the three arms simultaneously.

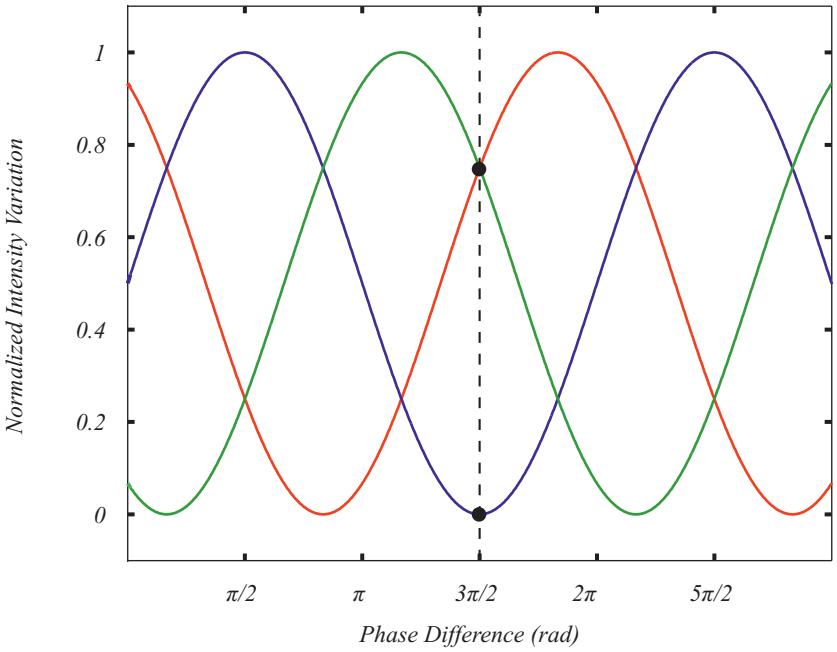

Figure 3.3: The normalized output intensities of an IMZI utilizing a 3×3 coupler as a function of phase difference $\Delta\phi$. While the output intensity of one arm (the blue line) is at its minimum, the output intensities of the two other arms are not.

3.2.3 Differentiate and Cross-Multiply Demodulation

Although the signal fading problem can be solved by introducing a 3×3 coupler in the IMZI, this technique has two main drawbacks. The first problem is to determine which output has the highest sensitivity at any given time which requires complicated signal processing. But the more important issue is the non-linear response of the interferometer outputs represented in equation (3.14).

Both problems can be addressed by using a phase detection technique known as the differentiate and cross-multiply demodulation scheme [12]. In this technique, by using the data acquired from the three outputs of the 3×3 coupler, the phase difference between the two arms of the MZI (i.e. $\Delta\phi$ in equation (3.14)) can be directly measured. The block diagram of the differentiate and cross-multiply demodulator is depicted in figure 3.4. For an interferometric output in form of equation (3.14), the mathematical analysis shows that the output of the demodulator is given by (appendix B)

$$V_{Out} = \sqrt{3}\Delta\phi \tag{3.15}$$

which is a linear function of the phase difference.

3.3 Experimental Arrangement

3.3.1 Experimental Setup

The experimental setup, shown in figure 3.5, can be divided into three principle sections: optical pulse generator, sensing fibre, and interferometer and data acquisition unit. In order to generate the interrogating pulse, the injection current of a distributed feedback

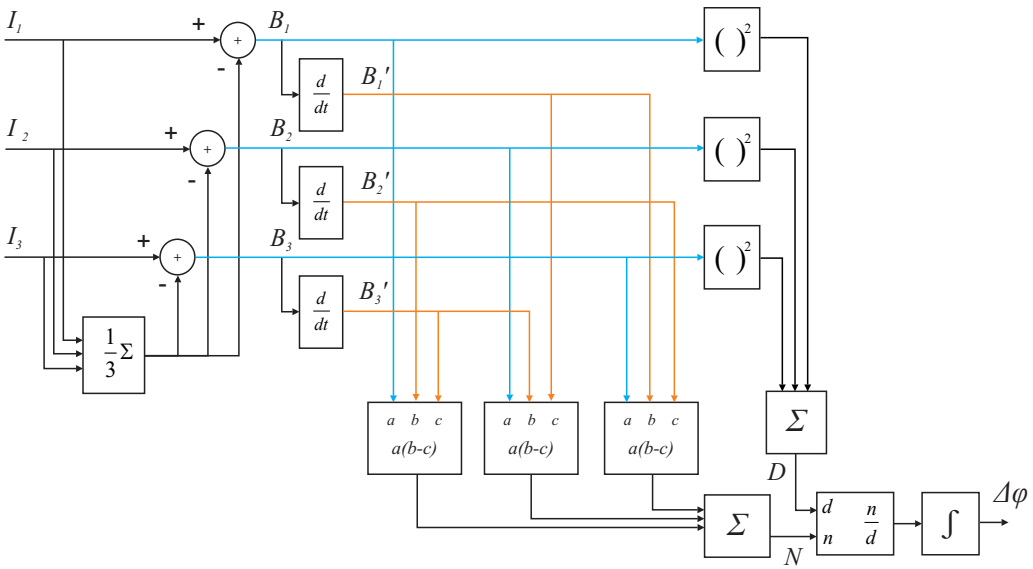

Figure 3.4: Block diagram of the differentiate and cross-multiply demodulator, adopted Camron et al. [12].

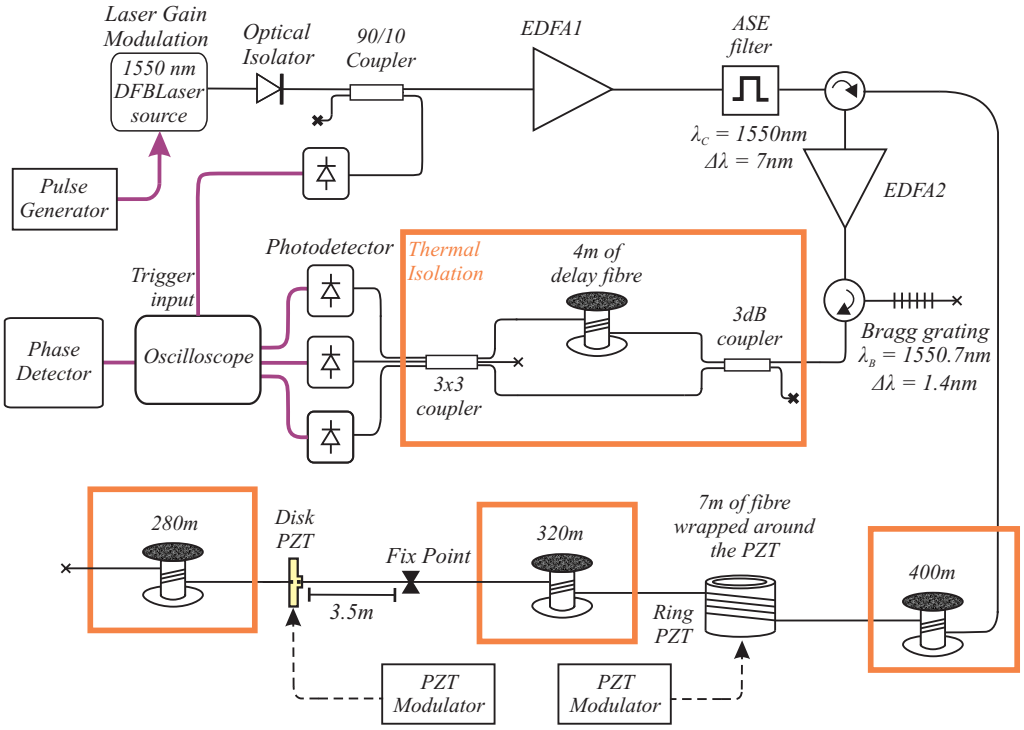

Figure 3.5: Experimental arrangement. EDFA: Erbium-doped fibre amplifier, PD: photodetector, FBG: fibre Bragg grating, PC: polarization controller, C: circulator, DFB: Distributed feedback.

(DFB) laser diode was directly modulated to generate $10ns$ optical pulses with a peak power of $10mW$ at a repetition rate of $10\mu s$. Using a 90/10 fibre coupler, 90% of each output pulse was amplified by a $28dB$ gain Erbium-doped fibre amplifier (EDFA) ($980nm$ laser diode-pump with $100mW$ cw output; $10m$ of Erbium-doped fibre) while the remaining 10% was used to trigger the oscilloscope. An optical isolator was used after the $1550nm$ laser diode to prevent the backward ASE (amplified spontaneous emission) generated in the EDFA(1) from causing instabilities in the laser diode. Forward ASE from EDFA(1) was filtered by an ASE-filter ($3dB$ bandwidth of $7nm$) and the amplified optical pulses ($\sim 4W$ peak power) were launched into the sensing fibre.

The sensing fibre included two regions of length $3.5m$ and $7m$ subjected to dynamic strain using a disk PZT and a cylindrical PZT, respectively. $320m$ of unstrained-unheated fibre was used to separate these two regions. A further $400m$ and $280m$ long streches of unstrained-unheated fibre were added before and after the $7m$ and the $3.5m$ strained sections respectively to separate them from the front-end and far-end of the sensing fibre.

Since the intensity of the backscattered Rayleigh light was low, it was amplified by another Er-doped fibre amplifier (EDFA(2) - $980nm$ laser diode-pump with $100mW$ cw output; $5m$ of Erbium-doped fibre) with $20dB$ gain. A fibre Bragg grating (FBG) (Reflectivity 99%; $\Delta\lambda = 3nm$; $\lambda_B = 1550.7nm$) was used to filter the EDFA2 forward ASE. The output of the FBG filter was fed into a thermally isolated IMZI via a 50/50 coupler. To combine the backscattered light from two separate regions of the sensing

fibre, the path-imbalance of the IMZI was set to $4m$ which corresponds to $2m$ spatial resolution. The three arms of the 3×3 coupler at the output of the IMZI were connected to three detectors ($40V/mA$ transimpedance, $125MHz$ bandwidth, $22.5pW/\sqrt{Hz}$ NEP). The outputs of the detectors were collected by a $250MHz$ oscilloscope (PicoScope model 6402B) with a sampling rate of $300MSa/s$. Since the data acquisition process of the oscilloscope was based on interleaved sampling, the length of the optical fibre leads from the 3×3 coupler to the photodetectors were adjusted to eliminate the consequent data acquisition time delay between the channels.

3.3.2 Signal Processing Procedure

The acquired signals on each detector consisted of a train of backscattered traces (figure 3.6(a)). The length of each trace was proportional to the length of the sensing fibre, and its repetition rate was equal to the repetition rate of the pulse generator. The train of the traces were rearranged to provide a 3D plot of the backscattered traces as shown in figure 3.6(b). Since each data point on the backscattered traces represents a

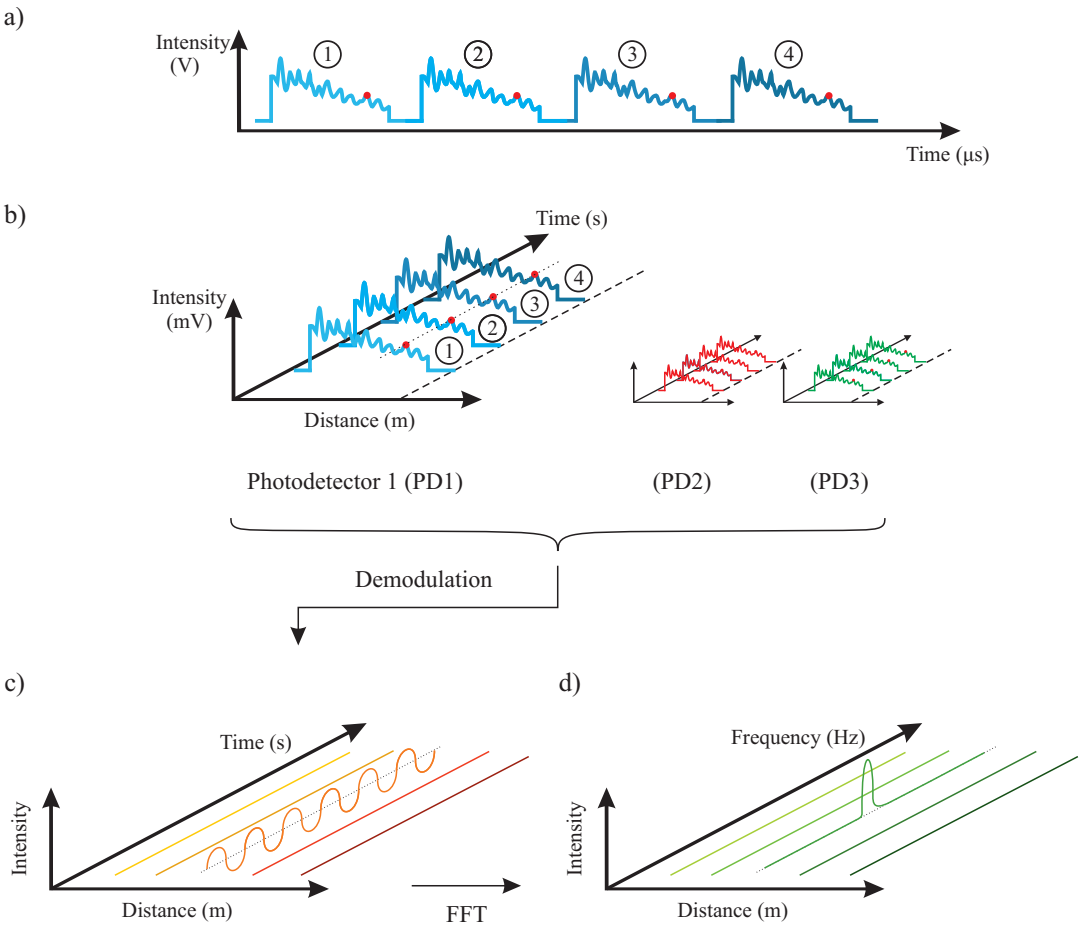

Figure 3.6: Rearrangement of (a) a two dimensional train of trances into (b) a three dimensional diagram depicting the sequence of traces. (c) Output of the differentiate and cross-multiply demodulator for an input data from three photodetectors, and (d) the FFT of the differentiate and cross-multiply demodulator output.

certain section of the sensing fibre, the rearrangement of backscattered traces allows for monitoring the sensing fibre as a function of both distance and time.

In order to quantify the disturbances at a particular position along the sensing fibre, the differentiate and cross-multiply demodulation procedure should be applied to the backscattered data collected from that position. Therefore, the differentiate and cross-multiply demodulation scheme was implemented digitally along the lines of the block diagram shown in figure 3.4 so that the demodulation process can be applied to each section of the sensing fibre individually. It should be pointed out that the demodulation process should not be implemented directly after the photodetectors by connecting the outputs of the detectors to an analogue demodulator. The reason for this is that, if the phase-demodulator is implemented directly after the photodetectors, the differentiator within the phase-detector would measure the spatial derivative of the backscattered data along the length of the sensing fibre [13] while for the sensor to measure the perturbation at each point, the differentiator is expected to measure the temporal derivative of that point. Therefore, the signal processing procedure was implemented digitally to provide the backscattered data for each point along the sensing fibre as a function of time.

The MATLAB code used to implement this algorithm is presented and explained in appendix C. A fast Fourier transform (FFT) was performed on the demodulated data along the time axis (figure 3.6(c)) to identify the frequency components of any phase perturbation occurring within that section. This process was then repeated for all of the points along the sensing fibre and drawn as a 3D plot showing the frequency spectrum of the perturbations along the sensing fibre as shown in figure 3.6(d).

3.3.3 Experimental Procedure

Both the disk and the ring PZTs were initially characterized using a MZI to determine their voltage-strain relationships at different frequencies before installing them in the experimental setup. To demonstrate the effect of induced strain on the sensing fibre, the applied voltages to the PZTs were initially adjusted to stretch the fibre sinusoidally by approximately $750nm$ or π radians corresponding to $375n\varepsilon$ strain. The frequency of the disk PZT and the cylindrical PZT were set to $1500Hz$ and $1900Hz$ respectively. To determine the frequency and strain range of the sensor, data were acquired for a range of frequencies and input voltages with a repetition rate of $10\mu s$ for $12ms$. To investigate the linearity of the sensor, the input frequency of the disk PZT was set to a fixed value while different voltages were applied to strain the fibre over the range of $50n\varepsilon$ to $1.5\mu\varepsilon$. In addition, to assess the accuracy of the sensor, the sensor response to $0.7V_{PP}$ input voltage for a range of frequencies was collected and compared to the PZT response which was determined eariler using a MZI.

3.4 Experimental Results

Figure 3.7(a) depicts the FFT of the phase-detector output in a 3D diagram. The horizontal axes at the bottom of the figure represent the distance and the frequency of perturbation while the vertical axis shows the magnitude of perturbation. The two peaks in the figure correspond to the two strained regions in the sensing fibre at distances of $400m$ and $720m$ from the front end of the fibre under test (FUT). Figure 3.7(b) shows the output of the phase-detector for $12m$ section of the sensing fibre where the disk PZT is located. The horizontal axes of this figure represent time and distance.

A 2D view of the diagrams from figure 3.7 is depicted in figure 3.8. The two frequency components shown in figure 3.8(a) correspond to the applied strain at $400m$ (red trace)

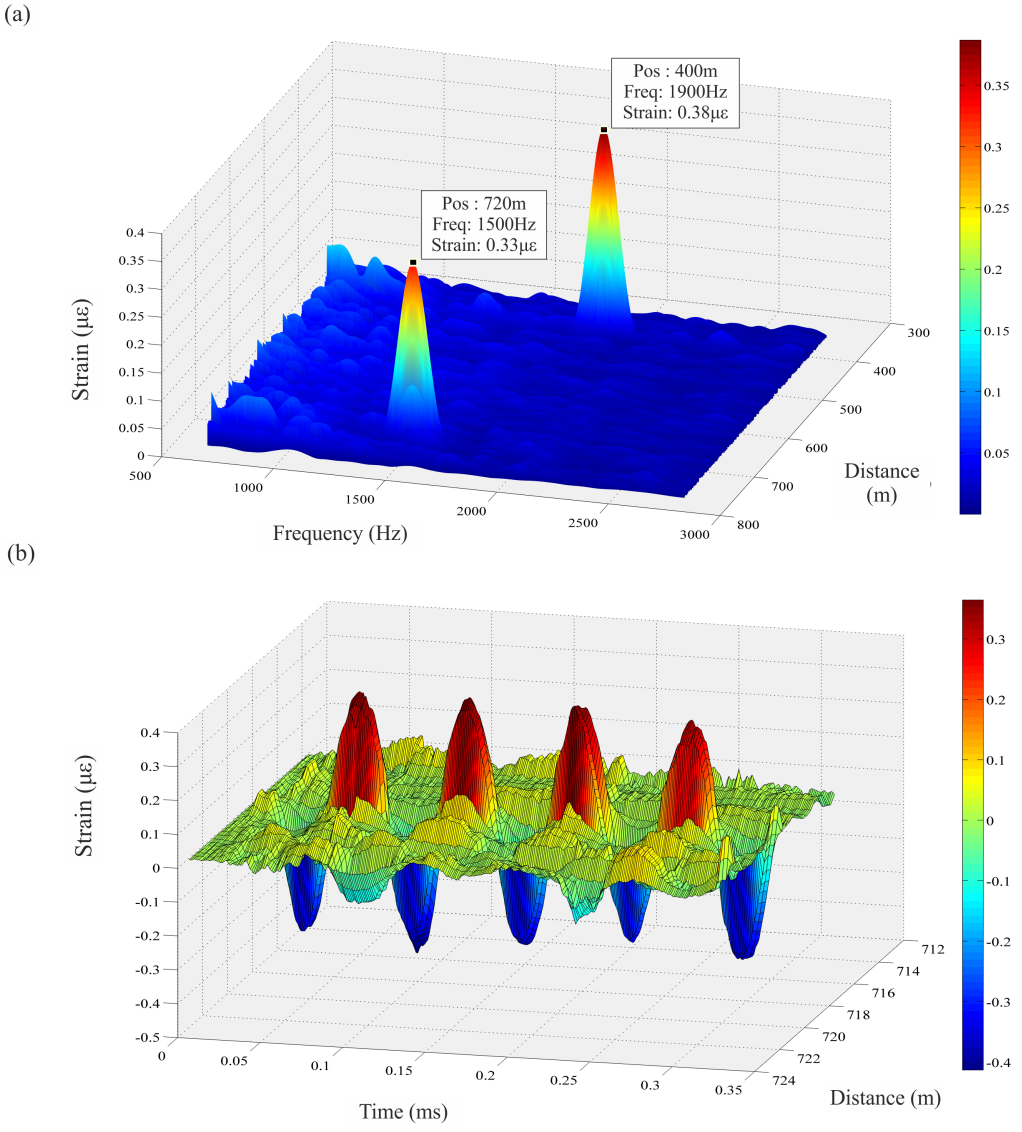

Figure 3.7: (a) 3D plot of FFT of the phase-detector output of the experimental setup. (b) 3D plot of the phase-detector output as a function of time and distance for a section of the sensing fibre in the vicinity of $720m$.

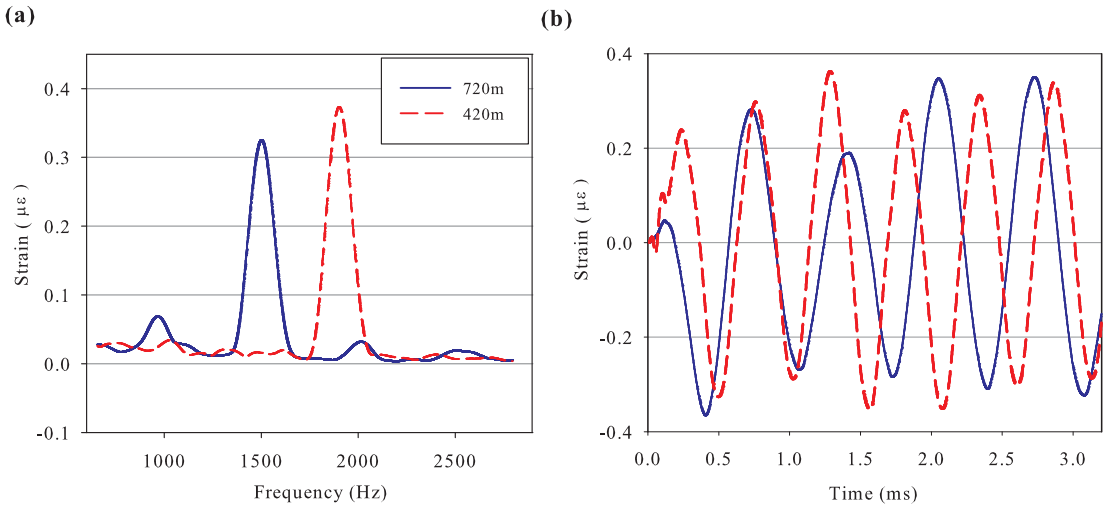

Figure 3.8: (a) 2D cross section of figure 3.7(a) at points 400m and 720m. (b) 2D cross section of the phase-detector output at the same points.

and $720m$ (blue trace) from the front end of the sensing fibre by the disk and cylindrical PZT, respectively. Figure 3.8(b) shows the output of the phase-detector as a function of time for the same positions.

Figure 3.9 depicts a 2D cross section of the 3D plot of figure 3.7(a), perpendicular to its frequency axis at $1500Hz$. The spatial range of the diagram is set to include the section of the sensing fibre where the disk PZT is located. The spatial response of the sensor to the the ring PZT is also shown in figure 3.13.

Figure 3.10 shows the sensor's response when the disk PZT was subjected to a sinusoidal disturbance at $900Hz$ sinwave of varying amplitude. The data points on this

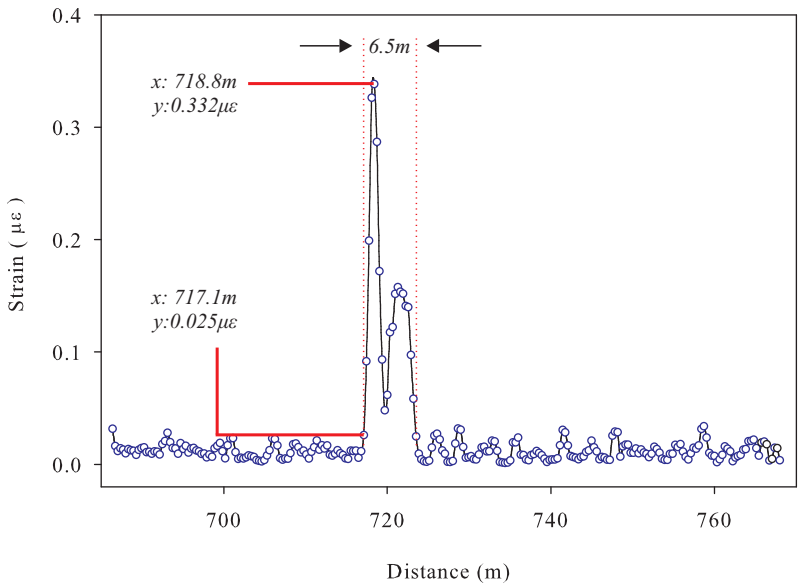

Figure 3.9: a 2D cross section of figure 3.7(a) perpendicular to its frequency axis at $1500Hz$.

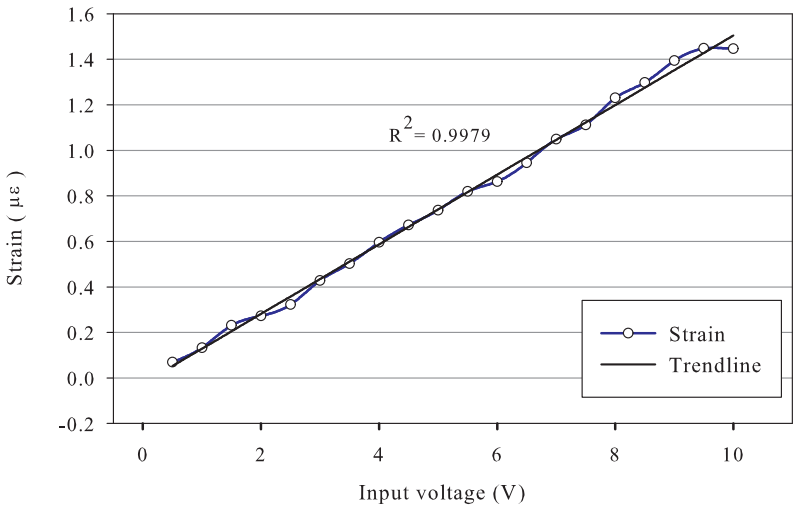

Figure 3.10: PZT input voltage versus sensor output for input sinusoidal signal at frequency of $900Hz$.

figure represent the peak value of the FFT of the phase-detector output. A correlation coefficient of 0.9979 was determined.

The frequency response of the sensing fibre to longitudinal strain induced by the disk PZT with an input voltage of $0.7V_{PP}$ is plotted in figure 3.11. In this figure, the output of the distributed sensor is shown in blue trace while the red trace shows the disk PZT frequency response characterized using a MZI.

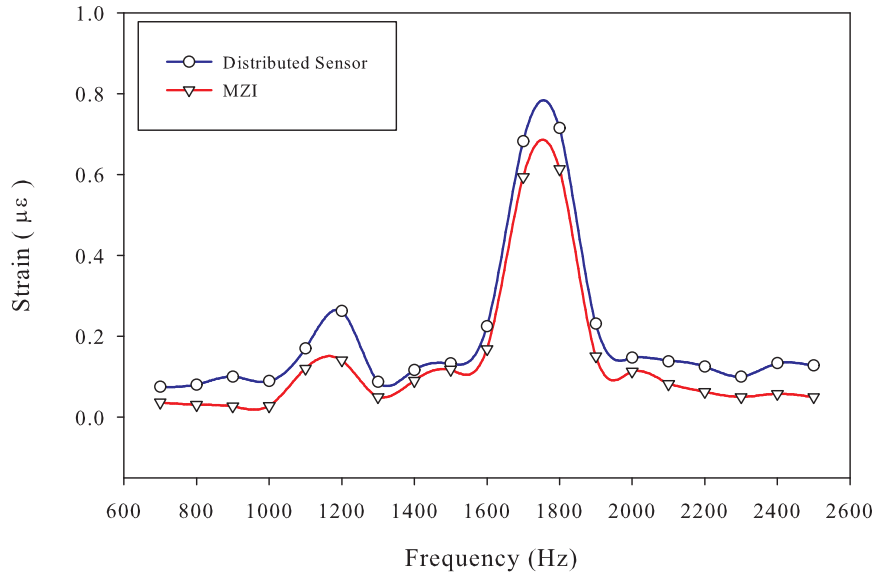

Figure 3.11: Frequency response of the PZT for input voltage of $0.7V_{PP}$ *where the red trace shows the frequency response of the FUT using a MZI and the blue trace shows that of the distributed sensor.*

3.5 Discussions

3.5.1 Interpretation of 3D Figures

The two peaks of figure 3.7(a) correspond to the strains applied by the two PZTs at $400m$ and $720m$. The 2D plot shown in figure 3.8(a) confirms that the peaks on the 3D diagram are accurately indicating the frequency and the amplitude of the strains applied to the FUT. Figure 3.7(b) shows the 3D plot of the phase-detector output as a function of time and distance for a section of the sensing fibre in the vicinity of disk PZT (*i.e.* $720m$). The 2D cross section of the phase-detector output at $400m$ and $720m$ shown in figure 3.8(b) confirms that the output of the phase-detector follows the sinusoidally applied strain to the sensing fibre.

3.5.2 Frequency Resolution of the Sensor

The frequency resolution of the sensor is governed by the data acquisition period of each experimental run. Frequency resolution, Δf, for a data acquisition period of T is given by

$$\Delta f = \frac{1}{T} = \frac{1}{R \times N_S} \tag{3.16}$$

where N_S is the overall number of traces captured at a repetition rate of R. This equation indicates that a higher frequency resolution can be achieved by capturing the data for a longer period of time. For the current experimental setup, the oscilloscope was set to capture 1200 traces per channel with a repetition rate of $10\mu s$. This corresponds to a theoretical frequency resolution of $83Hz$. This value was confirmed experimentally using the $3dB$ value of the peaks of the Fourier transform of the phase-detector output (figure 3.8(a)). The frequency range of the sensor was measured to be $500Hz$ to $5000Hz$.

3.5.3 Spatial Resolution of the Sensor

The spatial resolution of the sensor is determined by the length of the delay fibre as well as the duration of the probe pulses. In the current setup, the length of the delay fibre was $4m$ with interrogating pulse width of $10ns$, providing a spatial resolution of $2m$. The 2D cross section of figure 3.9 shows the mean value of the strain applied via the disk PZT. Unlike the ring PZT, vibrations initiated by the disk PZT form a travelling wave. Due to the elastic nature of the fibre, these travelling waves attenuate as they propagate away from the disk PZT. Therefore, the peak on the left in figure 3.9 has a higher amplitude than the peak on the right since it represents the strain of the sensing fibre for a section next to the disk PZT.

Figure 3.12 explains the behaviour of the sensor output for the $6.5m$ segment specified in figure 3.9. Since the delay fibre is added to the IMZI to compare the backscattered light from two sections of the sensing fibre, the operation of the setup can be modelled

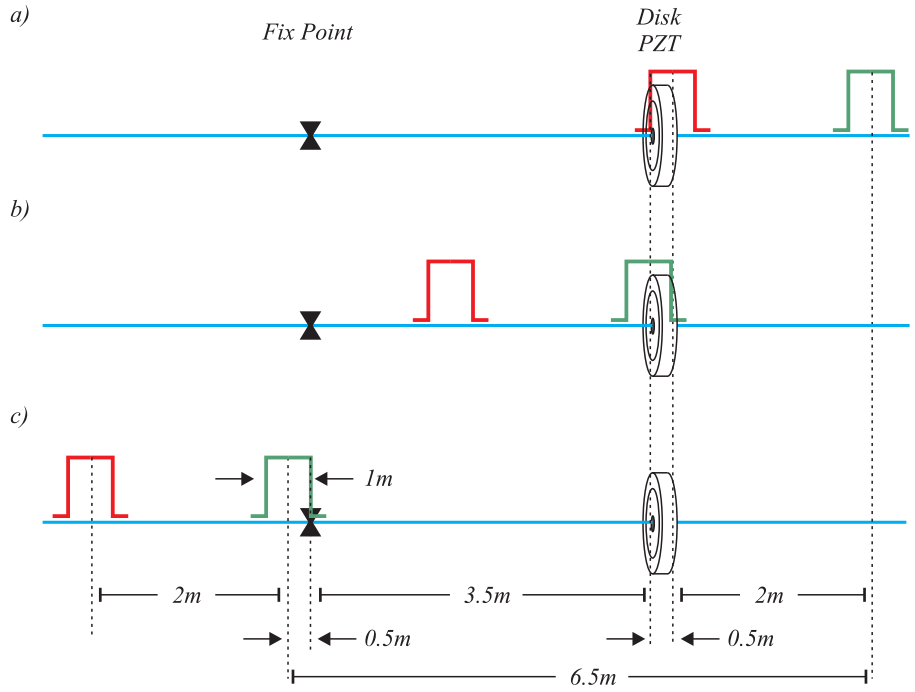

Figure 3.12: Diagram for explaining the behaviour of the sensor output for a 6.5m section of the sensing fibre in the vicinity of the disk PZT.

by the phase difference between two $10ns$ pulses which are separated by $2m$. A $10ns$ optical pulse in an SMF fibre with a group velocity of $2 \times 10^8\, m/s$ has a length of $2m$. Due to the round-trip propagation time of optical pulse in the sensing fibre, the backscattered trace from an optical pulse is twice as long as the length of the sensing fibre. Therefore, the spatial resolution of each point along the backscattered trace is half of the temporal length of the interrogating light pulse. Hence, the spatial resolution of an OTDR system with $2m$ interrogating pulse is $1m$.

The sensor output changes as soon as the rising edge of the red pulse enters the $3.5m$ region under strain (figure 3.12(a)). The strain keeps increasing for the next $2m \pm 0.33m$ ($\pm 0.33m$ is added to allow for $300MSa/s$ sampling rate of the oscilloscope) since there are no phase variations at the green pulse. As soon as the green pulse enters the $3.5m$ region (figure 3.12(b)), the output experiences a sharp decrease since the phase of the green pulse starts to change at a rate higher than that of the red pulse since it is closer to the PZT. The amplitude of the strain keeps falling until the red pulse starts leaving the $3.5m$ region (figure 3.12(c)). From this point onward, since there are no strain variations at the red pulse, the output starts to increase. However, this increase is not as large as the initial increase since the fibre experiences less strain away from the PZT. The total length of all these stages are shown to be $6.5m$ in figure 3.12.

To experimentally verify the $2m$ spatial resolution of the sensor, the section of the sensing fibre wrapped around the ring PZT can be used where a relatively uniform strain is applied to the fibre. Figure 3.13 shows the FFT of the phase-detector output

as a function of distance for $f = 1900Hz$ (*i.e.* the 2D cross section view of the 3D diagram of figure 3.7(a) for the peak at $1900Hz$). The $10\% \sim 90\%$ step response on this figure shows that the spatial resolution of the sensor is within the predicted value of $2m \pm 0.33m$. The spatial resolution can be improved by reducing the pulse width duration and the length of the delay fibre simultaneously.

3.5.4 Strain Range and Strain Resolution of the Sensor

Figure 3.10 shows a linear relationship between the amplitude of $900Hz$ sinusoidal strain applied on the FUT and the sensor output. Similar experiments at other frequencies (*i.e.* $1400Hz$, $1900Hz$, and $2300Hz$) verified that this linear relationship is independent of the frequency. The R^2 value of 0.9979 for the fitted line confirms a high level of linearity. The minimum detectable strain was measured to be $80n\varepsilon$ with signal to noise ratio (SNR) of 1. The strain accuracy was measured to be $30n\varepsilon$.

The main limiting factor for the minimum detectable strain and the strain resolution was the digitization level of the $8-bit$ digitizer used in the experimental setup. In order to optimize the experimental setup, the $8-bit$ input array of the digitizer should be adjusted to accommodate a phase-shift of π in the interference pattern of the MZI. The minimum detectable phase-shift for an $8-bit$ digitizer would be $\pi/2^8$. For $1550nm$ light source, this phase-shift corresponds to $3nm$ fibre elongation which, for $2m$ gauge length, translates to $1.5n\varepsilon$ strain. However, since the signal processing procedure involves assessing the slope and amplitude of interferometric fringes, at least 3 bits of data are required to identify any perturbation. This increases the strain resolution of the oscilloscope to $12n\varepsilon$. However, since the intensity of the light varies along the backscattered

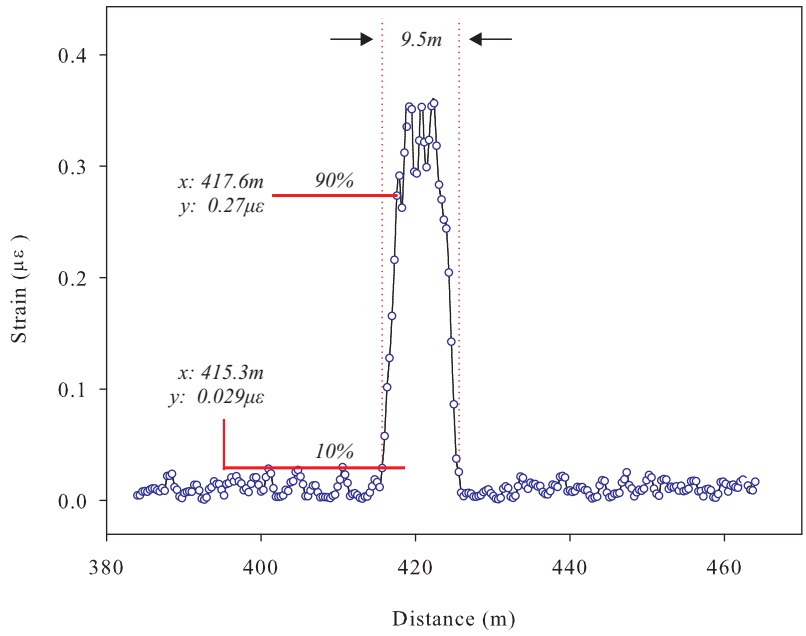

Figure 3.13: The FFT of the phase-detector output as a function of distance for $f = 1900Hz$.

trace, the voltage of the oscilloscope should be adjusted with regards to the highest intensity. Therefore, the strain resolution of the sensor was measured to be $30n\varepsilon$. The other sources of noise such as photodetector noise, ASE-ASE beat noise, ASE-signal beat noise, and shot noise can be neglected in the calculation of strain resolution since their contribution to the overall noise level are less significant in comparison with the limitation imposed by the digitizer.

The maximum detectable strain of the sensor depends on two factors: the length of the sensing fibre and the frequency of the dynamic strain. The length of the sensing fibre determines the repetition rate of the interrogating pulse which itself governs the sampling rate for each point along the FUT. Therefore, the frequency of the interferometric fringes should be kept less than half of the sampling frequency to ensure that each point along the sensing fibre is sampled at the Nyquist rate. On the other hand, the magnitude of the strain perturbation determines the phase-change and hence the frequency of the interferometric fringes. If the fibre elongation magnitude exceeds the wavelength of the probe pulse ($\lambda = 1550nm$ in case of the proposed setup), the output of the interferometer will travel over one fringe. As a result, perturbations with higher magnitudes exhibit a higher frequency at the output of an interferometer. The relationship between the frequency of the strain, f_{strain}, the length of the FUT, L, and the maximum detectable strain, ε_{max}, is governed by

$$\varepsilon_{max}.\, f_{strain}.\, L = K \tag{3.17}$$

where K is a constant. In order to determine the minimum sampling rate requirement for the detection of perturbations with large-magnitudes, the maximum slope of the interferometer output for a sinusoidal strain should be calculated first. The normalized intensity of an output of the IMZI (figure 3.2) can be written as

$$I = 1 + sin(\Delta\phi(t)). \tag{3.18}$$

Substituting equation (3.6) in (3.18) gives

$$I = 1 + sin[4\pi\frac{\Delta L(t)}{\lambda}] \tag{3.19}$$

where $\Delta L(t)$ represents the elongation of the sensing fibre due to induced strain as a function of time. For a sinusoidal strain, equation (3.19) becomes

$$I = 1 + sin[4\pi\frac{\varepsilon L_0}{\lambda}\, sin(2\pi f\, t)] \tag{3.20}$$

where L_0 is the mean distance between the two segment, ε is the magnitude of the strain, and f is the frequency of the induced strain. To find the maximum rate of change in the intensity of the interferometer output, the derivative of equation (3.20) needs to be calculated

$$\frac{dI}{dt} = cos[4\pi\frac{\varepsilon L_0}{\lambda}\, sin(2\pi f\, t)].4\pi\frac{\varepsilon L_0}{\lambda}\, cos(2\pi f\, t).2\pi f. \tag{3.21}$$

It can be shown that the maximum of this equation occurs when $t = n/f$ $(n \in \mathbb{Z})$. Therefore

$$\frac{dI}{dt}\,|_{max} = 8\pi^2 f\,\frac{\varepsilon L_0}{\lambda}. \tag{3.22}$$

Using linear approximation, it can be shown that

$$\lim_{t \to 0} \quad sin(2\pi f\,t) = 2\pi f\,t \tag{3.23}$$

Therefore, for $t = n/f$ $(n \in \mathbb{Z})$, equation (3.20) can be approximated by

$$I \backsimeq 1 + sin(4\pi\frac{\varepsilon L_0}{\lambda}\,2\pi f\,t). \tag{3.24}$$

In addition, according to the Nyquist theorem, the minimum sampling rate required to accurately quantify a sinwave function is twice the frequency of that sinwave. Therefore, the minimum sampling frequency (S_{eff}) required for sampling the sinusoidal function of equation (3.24) is given by

$$S_{eff} = 8\pi f\,\frac{\varepsilon L_0}{\lambda}. \tag{3.25}$$

Equations (3.17) and (3.25) demonstrate the limitations imposed on the strain and frequency ranges of the sensor. First of all, the maximum repetition rate of any OTDR system is limited by the round-trip of the pulse-light in the FUT. As a result, the maximum sampling rate in equation (3.25) is determined by the length of the FUT. Therefore, for any setup with a fixed sensing length and at any given frequency, the maximum detectable strain is determined by equation (3.17). In order to maintain the linear relationship between the sensor output and the imposed strain, it is essential to keep the strain below this maximum value.

Figure 3.14 shows the response of the digitally implemented phase-demodulator to sinusoidal phase variation with three different magnitudes (2π, 3π, and 4π radian) as a function of frequency. The four diagrams in this figure represent the effect of the sampling rate on the phase-demodulator output. The vertical dashed-lines on the two diagrams at the bottom of figure 3.14 determine the maximum frequency limit of each strain rate calculated using equation (3.25). Although the dashed-lines correctly estimate the maximum detectable frequency, it can be seen that the phase-demodulator responses are not constant even for the frequencies below the maximum frequency identified by the dashed-lines. This deviation from a straight line is due to the differentiation procedure of the phase-demodulator explained in appendix C.

According to equation (3.25), the maximum detectable frequency for $1.5\mu\varepsilon$ strain using the proposed experimental setup ($1km$ sensing length which is equivalent to $10\mu s$ repetition rate and $100kSa/s$ sampling rate, $2m$ spatial resolution, $\lambda = 1550nm$) is $4111Hz$. The maximum frequency measured experimentally was $4000Hz$. To increase the frequency range of the sensor, either the gauge length of the sensor should be reduced or the sampling rate of the sensor needs to be increased using an arrangement with

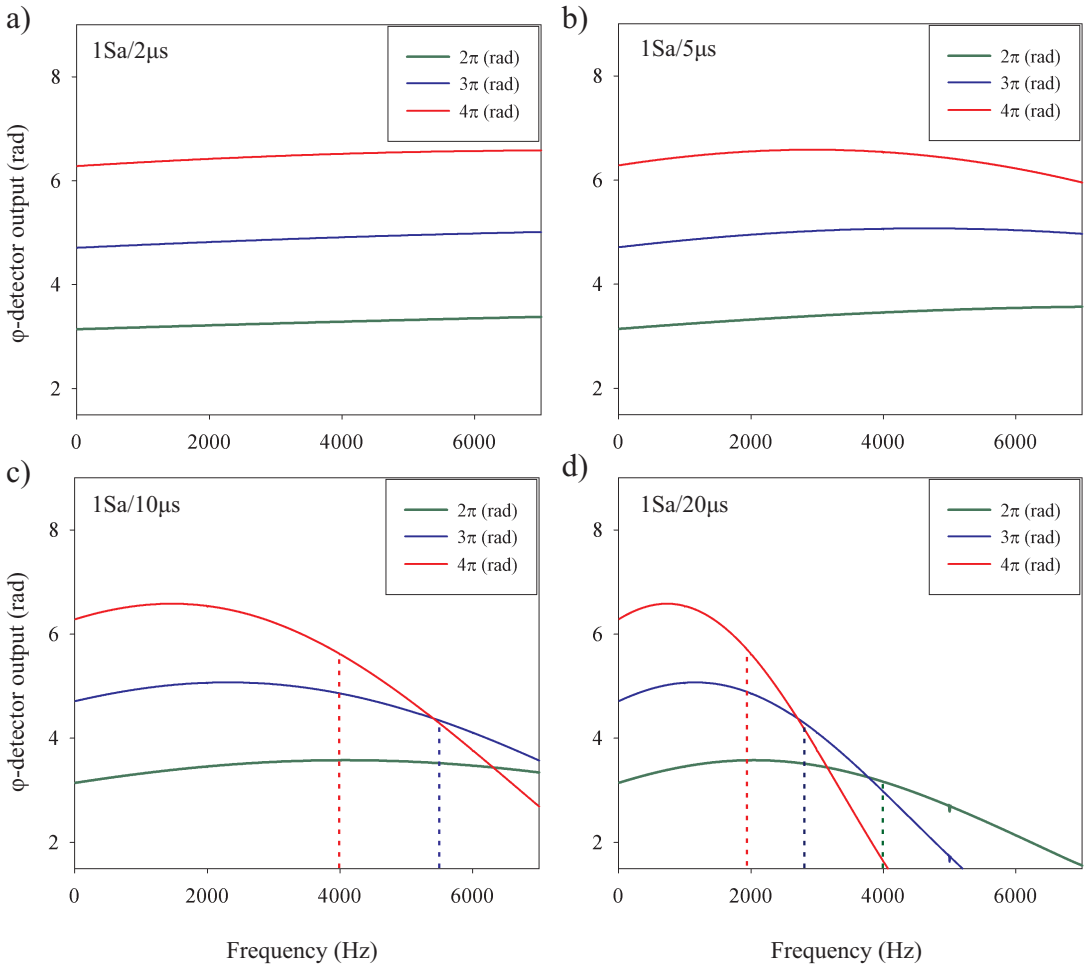

Figure 3.14: The response of the digitally implemented phase-demodulator to sinusoidal phase variation with three different magnitudes ($2\pi \sim 4\pi$ radian) as a function of frequency. The four diagrams represent four different sampling rates; these are (a) $1Sa/2\mu s$, (b) $1Sa/5\mu s$, (c) $1Sa/10\mu s$, and (d) $1Sa/20\mu s$. The dashed-line on these diagrams represents the maximum detectable frequency according to equation (3.25).

wavelength division multiplexing.

The blue and red traces of figure 3.11 which show the measured frequency response of the fibre using the distributed sensor and a MZI arrangement indicate good correlation. This demonstrates that the strain rate measured using the distributed sensor agrees with the data collected using the MZI. Therefore, the proposed setup is capable of quantifying the frequency and the magnitude of perturbations along the fibre.

3.5.5 Data Acquisition Limitations

The lower frequency limit of the sensor's frequency range is determined by the data acquisition period of each experimental run. For $12ms$ acquisition period, the lower frequency limit of $500Hz$ was experimentally determined. To reduce the lower frequency limit, the data acquisition period needs to be increased either by using an oscilloscope with a deeper internal memory (for instance, to save $1s$ worth of data using the current

experimental setup, $2.5GB$ memory was required) or by streaming the data from the oscilloscope to an external data storage unit.

To calculate the required data transfer rate for streaming the data, the rate at which the backscattered data were sampled needs to be determined first. The triggering instant of the oscilloscope is an important factor in determining the required sampling rate. Since the time along the backscattered trace represents the distance along the sensing fibre, a small change in the triggering time affects the locations at which the backscattered light is being sampled. For instance, if the triggering time changes by $1ns$, the location of the samples along the sensing fibre will change by $20cm$ ($1ns \times 2 \times 10^8 = 20cm$). Since the operation of the sensor is based on sampling the backscattered light from certain points along the sensing fibre and measuring the phase-variation at those points as a function of time, any changes in the location at which the backscattered light is sampled will introduce an error in the output of the sensor. Therefore, the triggering jitter of the oscilloscope plays a crucial role in the operation of the sensor.

Due to the influence of trigger jitter on the operation of the sensor, a sampling rate of $50MSa/s$ (which is equivalent to one sample every $2m$) is not sufficient for a sensor with $2m$ spatial resolution. Therefore, a higher sampling rate of $300MSa/s$ was adopted (which is equivalent to one sample every $33cm$) which corresponds to sampling rate of $4 \times 300MSa/s = 1.2GSa/s$ for four channels (three channels for the IMZI outputs, one channel for triggering output). Since the oscilloscope used to capture data was not capable of transferring data at this rate, all of the experiments were conducted using the internal memory of the oscilloscope. $1.2GSa/s$ determines the minimum data transfer rate required for real time data analysis.

3.6 Conclusions

The principle of dynamic strain measurement has been established in this chapter using phase-sensitive OTDR. It is shown that by combining an IMZI with a symmetrical 3×3 coupler, the frequency and amplitude of multiple perturbations along $1km$ sensing fibre can be measured simultaneously with a spatial resolution of $2m$. It is shown that such a measurement requires a digitally implemented differentiate and cross-multiply demodulator to extract the phase information from the output of the IMZI while avoiding the signal fading problem. The experimental results show a strain resolution of $30n\varepsilon$ over a frequency range of $500Hz$ to $4000Hz$. The frequency and strain range and their relationships with the pulse repetition rate and the length of the sensing fibre have been established.

In this chapter, the response of the distributed dynamic strain sensor to uniform longitudinal strains was assessed. The next chapter expands on this concept to demonstrate a distributed acoustic sensor (DAS) capable of measuring non-uniform spherical acoustic waves. The effect of the longitudinal strain induced by PZT and acoustically induced transverse strain on the sensing fibre is demonstrated, and it is shown that the

sensing fibre can be used as a distributed microphone.

Bibliography

[1] M. N. Alahbabi, Y. T. Cho, and T. P. Newson, "Simultaneous temperature and strain measurement with combined spontaneous Raman and Brillouin scattering," Optics Letters, vol. 30, pp. 1276-1278, 2005.

[2] H. H. Kee, G. P. Lees, and T. P. Newson "1.65μm Raman-based distributed temperature sensor," Electronics Letters, vol. 35, pp. 1869-1871, 1999.

[3] M. Belal, Y. T. Cho, M. Ibsen, and T. P. Newson, "A temperature-compensated high spatial resolution distributed strain sensor," Measurement Science & Technology, vol. 21, 015204, 2010.

[4] K. Y. Song, Z. He, and K. Hotate, "Distributed strain measurement with millimeter-order spatial resolution based on Brillouin optical correlation domain analysis," Optics Letters, vol. 31, pp. 2526-2528, 2006.

[5] M. N. Alahbabi, Y. T. Cho, and T. P. Newson, "Long-range distributed temperature and strain optical fibre sensor based on the coherent detection of spontaneous Brillouin scattering with in-line Raman amplification," Measurement Science & Technology, vol. 17, pp. 1082-1090, 2006.

[6] M. N. Alahbabi, Y. T. Cho, and T. P. Newson, "100km distributed temperature sensor based on coherent detection of spontaneous Brillouin backscatter," Measurement Science & Technology, vol. 15, pp. 1544-1547, 2004.

[7] S. V. Shatalin, V. N. Treschikov, and A. J. Rogers, "Interferometric optical time-domain reflectometry for distributed optical-fiber sensing," Applied Optics, vol. 37, pp. 5600-5604, 1998.

[8] R. J. Posey, G. A. Johnson, and S. T. Vohra, "Strain sensing based on coherent Rayleigh scattering in an optical fibre," Electronics Letters, vol. 36, pp. 1688-1689, 2000.

[9] D. A. Jackson, R. Priest, A. Dandridge, and A. B. Tveten, "Elimination of drift in a single-mode optical fiber interferometer using a piezoelectrically stretched coiled fiber," Applied Optics, vol. 19, pp. 2926-2929, 1980.

[10] S. K. Sheem, T. G. Giallorenzi, and K. Koo, "Optical techniques to solve the signal fading problem in fiber interferometers," Applied Optics, Vol. 21, pp. 689-693, 1982.

[11] R. G. Priest, "Analysis of fiber interferometer utilizing 3×3 fiber coupler," IEEE Journal of Quantum Electronics, vol. 18, pp. 1601-1603, 1982.

[12] C. B. Cameron, R. M. Keolian, and S. L. Garrett, "A symmetrical analog demodulator for optical fiber interferometric sensors," Proceedings of the 34th Midwest Symposium on Circuits and Systems, vol. 2, pp. 666-671, 1992.

[13] M. Farhadiroushan, T. R. Parker, S. Shatalin, "Optical sensor and method of use," U.S. Patent 2012/0162639A1, June 28, 2012.

Chapter 4

Acoustic Wave Sensor

4.1 Introduction

Following the early demonstration in 1977 by Cole *et al.* [1] and Bruno *et al.* [2] that sound could be detected using optical fibres, much of the subsequent research activity has focused on developing optical fibre hydrophones. The majority of such devices have utilized multiple fibre optic Mach-Zehnder interferometers (MZI) for detecting the acoustically-induced phase perturbations. An early reported distributed sensor proposed by Kurmer *et al.* [3] used a Sagnac interferometer to detect acoustic vibrations anywhere along a $5km$ of fibre. Whilst this technique is capable of detecting the location of a single acoustic perturbation along the sensing fibre, it does not allow multiple acoustic disturbances to be monitored as the output of the Sagnac interferometer returns the net phase-change due to all acoustic perturbations along the Sagnac loop.

In the previous chapter, a DOFS capable of detecting dynamic strains along the sensing fibre was demonstrated. In this chapter, a similar experimental setup is used to evaluate the effect of acoustic waves on the sensing fibre and to confirm that the output of the sensor corresponds to the frequency and amplitude of acoustic disturbances along the fibre. In addition, the effect of the mechanical properties of the sensing fibre on the sensitivity of the sensor is studied.

4.2 Principles

In order to evaluate the effect of acoustic perturbations on an optical fibre, the propagation of an acoustic wavefronts generated by an acoustic transducer needs to be studied first. For a point acoustic source, the acoustic power radiates equally in all directions. Therefore, the wavefronts of such a source are spheres which propagate radially outward. The distance between the wavefronts defines the wavelength of a sound wave. Therefore, the wavefronts of a sound wave with higher frequency are closer to each other than that with lower frequency.

The sensing mechanism of the distributed sensor demonstrated in the previous chap-

ter depends not only on the frequency and amplitude of the imposed sinusoidal strain, but also on the phase of the strain. The sensor measures the net induced strain within the gauge length of the sensing fibre. Therefore, while strains with similar phase are added constructively within the gauge length, strains with opposite phase cancel each other out and, as a result, they will not be observed at the output of the sensor.

The interaction between spherical acoustic wavefronts and an optical fibre results in a non-uniform strain in the fibre. Considering the inverse relationship between the sound-pressure level, P, and the distance from the sound source, r,($P \propto 1/r$) and with an assumption that the acoustic pressure level has a linear relationship with the induced strain on the sensing fibre, $\varepsilon(r)$, the strain at each point on the fibre is given by

$$\varepsilon(r) \propto P_{source} \frac{\sin(2\pi f\, t + \frac{2\pi}{\lambda_a} r)}{r} \tag{4.1}$$

where P_{source} is the sound pressure at the source, f and λ_a are the frequency and wavelength of the sound wave ($f\,\lambda_a \cong 340\,m/s$ in air), and r is the distance between the sound source and the fibre. Figure 4.1 demonstrates the normalized strain distribution induced on a $2m$ sensing fibre as a result of the acoustic waves emitted by a sound source at a distance of $50cm$ from the fibre. It can be seen that the strain distribution is not only a function of the sound-pressure level, but also of its frequency. Figure 4.2 shows the net induced strain on a $2m$ optical fibre as a function of the frequency of the acoustic source for the arrangement shown in figure 4.1. The blue line in this figure represents the integrated strain over the entire length of the fibre (*i.e.* $2m$) while the red and the green lines represent the integrated strain on the mid $1m$ and mid $50cm$ sections of the fibre, respectively. This figure demonstrates that the strain sensitivity

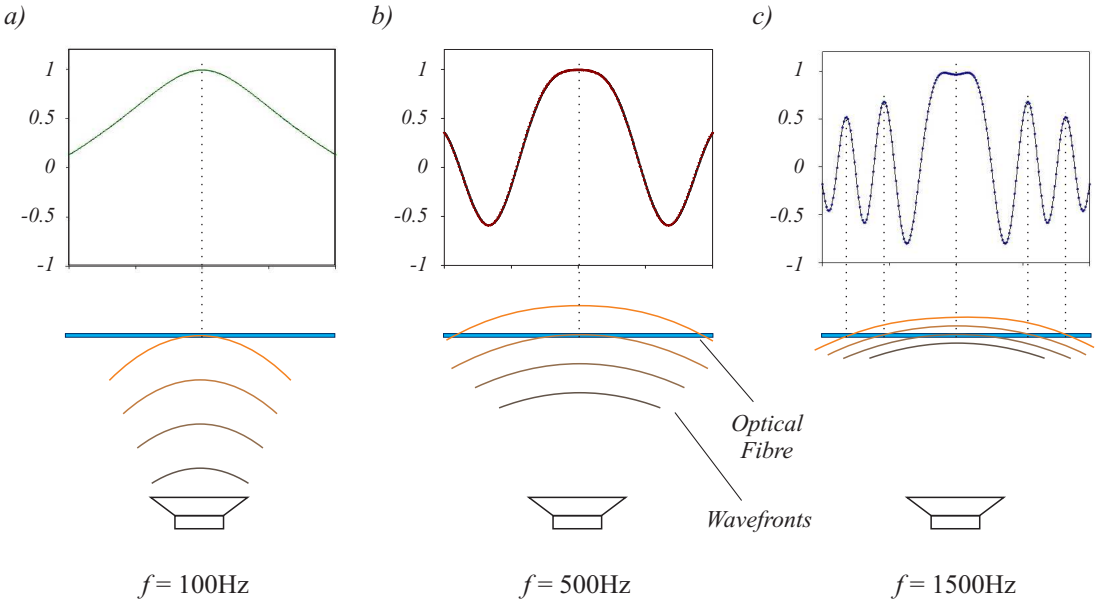

Figure 4.1: The normalized strain distribution induced on a 2m optical fibre as a result of the acoustic waves of a sound source at a distance of 50cm from the fibre.

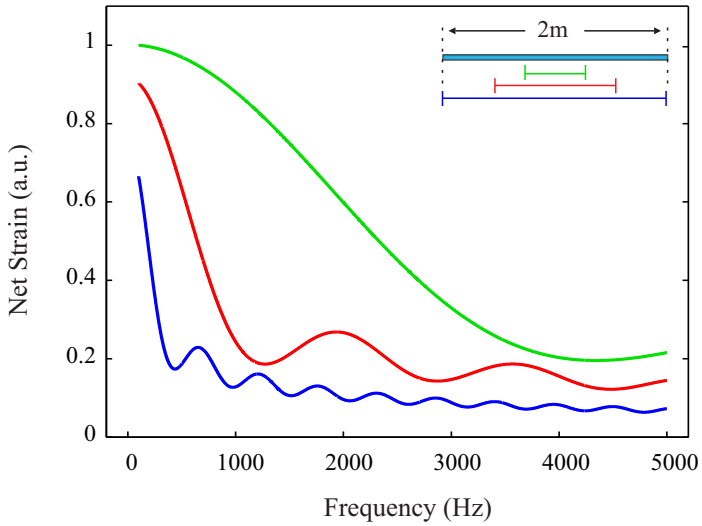

Figure 4.2: Net induced strain on a 2m optical fibre as a function of the frequency of the acoustic source positioned at a distance of 50cm from the fibre.

of the sensor reduces as the frequency of the acoustic wave increases. In addition, for any given frequency interval along the frequency axis of this figure, it can be seen that the variation of the net strain over a shorter gauge length (*e.g.* the green line) is slower than that of a longer gauge length (*e.g.* the blue line), a phenomenon which can be observed intuitively from figure 4.1. Therefore, in order to employ the experimental setup introduced in the previous chapter as a distributed acoustic sensor, a shorter gauge length needs to be used.

The properties of the sensing fibre such as its geometry and composition are important factors in determining the sensitivity of a distributed acoustic sensor as well. The relationship between the pressure-induced phase-shift, $\Delta\phi$, in an optical fibre due to pressure P is given by [4]

$$\frac{\Delta\phi}{PL} = \frac{\beta(1-2\mu)}{E}\left[\frac{n^2}{2}(2p_{12}+p_{11})\right] \tag{4.2}$$

where L and E are the length and Young's modulus of the fibre, while μ represents its Poisson's ratio. n denotes the effective refractive index of the fibre, β is the propagation constant of the light in the fibre, and p_{11} and p_{12} are the strain-optic coefficients of the fibre. This equation shows that the pressure-induced phase-shift is inversely proportional to the Young's modulus of the fibre. Although the value of the Young's modulus for an SMF-28 silica fibre cannot be directly adjusted to change the sensitivity of an optical fibre, it is shown that the pressure-induced phase-shift can be enhanced by embedding the fibre in a different elastic material [5]. By coating the sensing fibre with a polymer with low Young's modulus in comparison with the Young's modulus of the fibre, and by increasing the coating thickness with respect to the diameter of the fibre, the sensitivity of the sensor can be improved by two orders of magnitude [5]. Increasing the thickness

of the fibre coating enhances the sensitivity of the fibre to acoustic waves by expanding its effective surface area. The effective surface area of the fibre can also be improved by attaching it to an object with large surface area and high sound wave absorption coefficient.

4.3 Experimental Arrangement

4.3.1 Experimental Setup

The experimental setup of the sensor studied in this chapter was similar to that of the distributed sensor investigated in the previous chapter except for three changes. The first change was to replace the ASE filter after the first Erbium-doped fibre amplifier (EDFA1) with a FBG filter (Reflectivity 99% ;$\Delta\lambda = 3nm$;$\lambda = 1550.7nm$) to improve the rejection of the ASE noise. The second change was a reduction in the path-imbalance of the MZI to improve the spatial resolution of the sensor from $2m$ down to $1m$. The final change was the introduction of an acoustic module to the setup in order to assess the effect of acoustic perturbations on the fibre. The acoustic module comprised of two $70cm$ optical fibres attached to a $700mm \times 450mm \times 25mm$ polystyrene sheet and a loud speaker. Both of the fibres used in the acoustic module were SMF-28, one with acrylate CPC6 coating with a thickness of $165\mu m$ and the other without any coating. The two fibres were used separately to evaluate the effect of the diameter of the fibre coating on its sensitivity to acoustic perturbations. The polystyrene sheet was used to enhance the acoustic sensitivity of the fibres by increasing its effective surface area. A

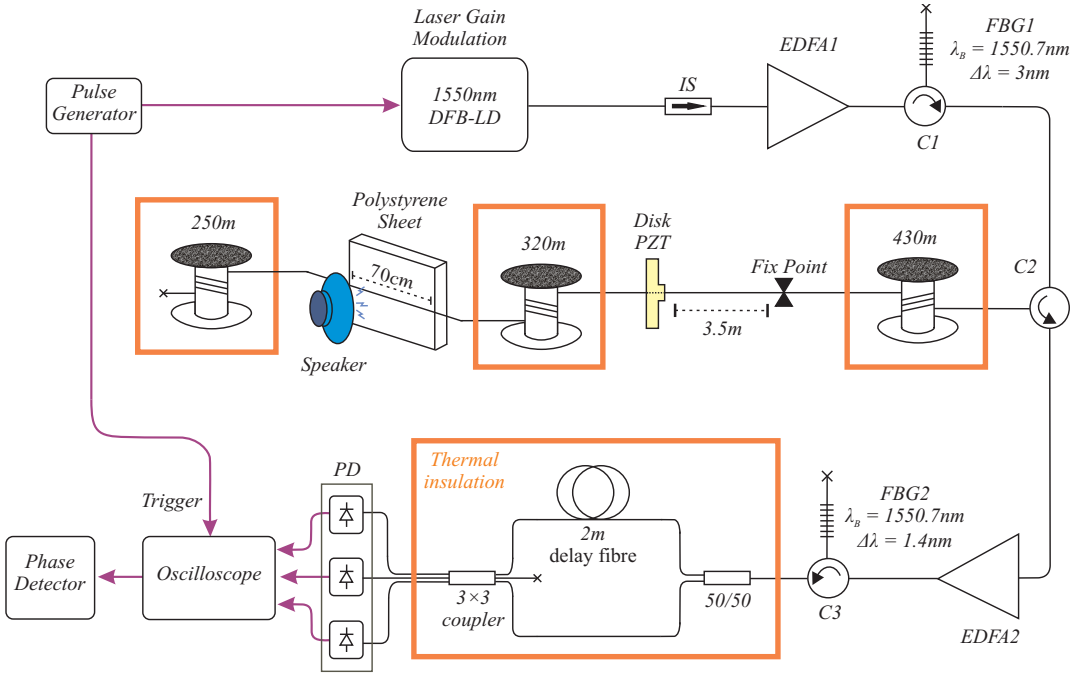

Figure 4.3: Experimental Setup. DFB-LD: distributed feedback laser source, IS: isolator, EDFA: Erbium-doped fibre amplifier, PD: photodetector, FBG: fibre Bragg grating, C: circulator.

calibrated microphone was also attached to the polystyrene sheet in order to monitor the frequency and pressure-level of the sound waves at the middle section of the fibres. The experimental setup is shown in figure 4.3. In order to demonstrate the sensitivity of the setup to both longitudinal and transverse strains, the disk PZT module used in the experimental setup of the previous chapter was included in the arrangement alongside the acoustic module. The acoustic module was used to induce transverse strain on the sensing fibre while the disk PZT was used to impose longitudinal strain.

4.3.2 Experimental Procedure

Since the response of the sensor to longitudinal strain has been studied in the previous chapter, the focus of this chapter is to evaluate the sensor's response to acoustically-induced transverse strain. Therefore, the disk PZT was retained in the experimental setup to show that the sensor can detect both longitudinal and transverse strain simultaneously and also to demonstrate the capability of the sensor to measure multiple dynamic disturbances at the same time. So, the frequency and voltage of the signal applied to the disk PZT was kept, respectively, at $1500Hz$ and $4V_{PP}$ throughout the experiment. To generate acoustic perturbation, a loud speaker was used at various distances from the sensing fibre. The pressure and frequency of the sound waves radiated from the speaker were monitored by the calibrated microphone installed on the polystyrene sheet. Sinusoidal voltages with various frequencies were applied to the loud speaker to generate sound waves with sound-pressure levels ranging from $90dBC$ to $120dBC$. For each experimental run, $10ns$ pulses with repetition rate of $20\mu s$ were launched into the sensing fibre and the backscattered traces were collected for $100ms$. This was equivalent to 5000 traces.

To investigate the linearity of the sensor's response to pressure-induced strain, $800Hz$ sinusoidal sound waves with pressure-levels ranging from $90dBC$ to $120dBC$ were applied to the acoustic module from a fixed distance ($40cm$) and the backscattered data were collected from each sensing fibre (with and without coating) separately. In order to evaluate the sensor's response to an acoustic source as a function of its distance to the source, the loud speaker was placed at a number of different positions from the sensing fibre covering distances from $30cm$ to $100cm$, while radiating a uniform acoustic wave. To analyse the sensors response to acoustic perturbations with multiple frequencies, a human voice was recorded and played back through the loud speaker and the data were recorded with both the microphone and the sensor.

4.4 Results

The 3D diagram of figure 4.4 shows the FFT of the phase-detector output between $400m$ and $800m$ for a $2\mu\varepsilon$ longitudinal strain with a frequency of $1500Hz$ applied by the disk PZT and a $100dBC$ sinusoidal acoustic wave (*i.e.* transverse strain) with a

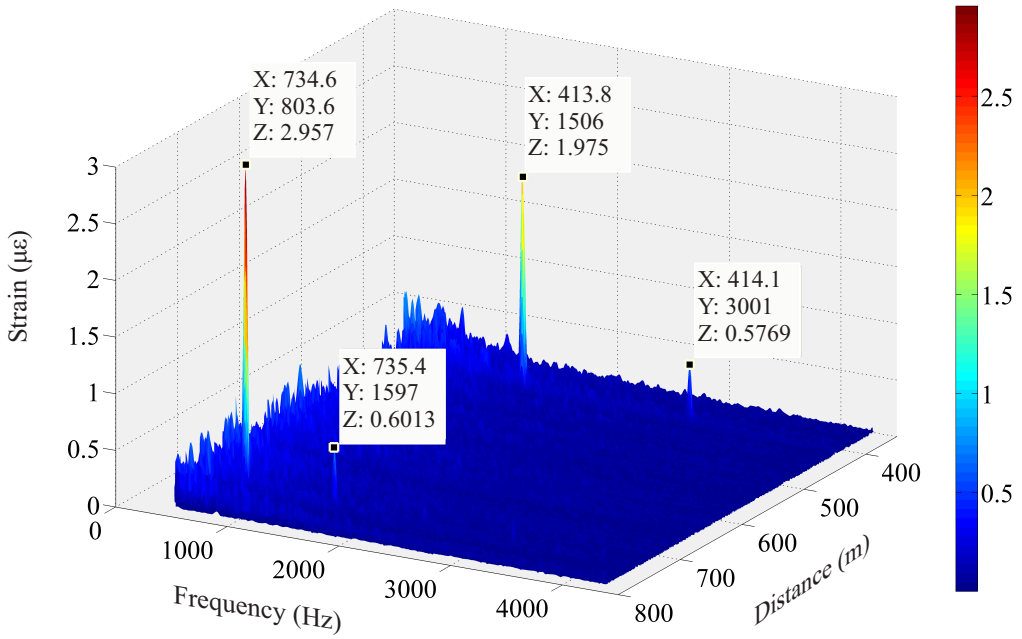

Figure 4.4: 3D plot of FFT of the phase-detector output for the data points between $400m$ *and* $800m$.

frequency of $800Hz$ applied by the loud speaker. The two smaller peaks at $3000Hz$ and $1600Hz$ represent the second harmonics of the perturbation due to the PZT and speaker respectively. The horizontal axes of this figure represent the distance along the sensing fibre and the frequency of the perturbation while the vertical axis represents the induced strain on the fibre.

Figure 4.5 shows the response of the two sensing fibres (*i.e.* the fibre with $165\mu m$

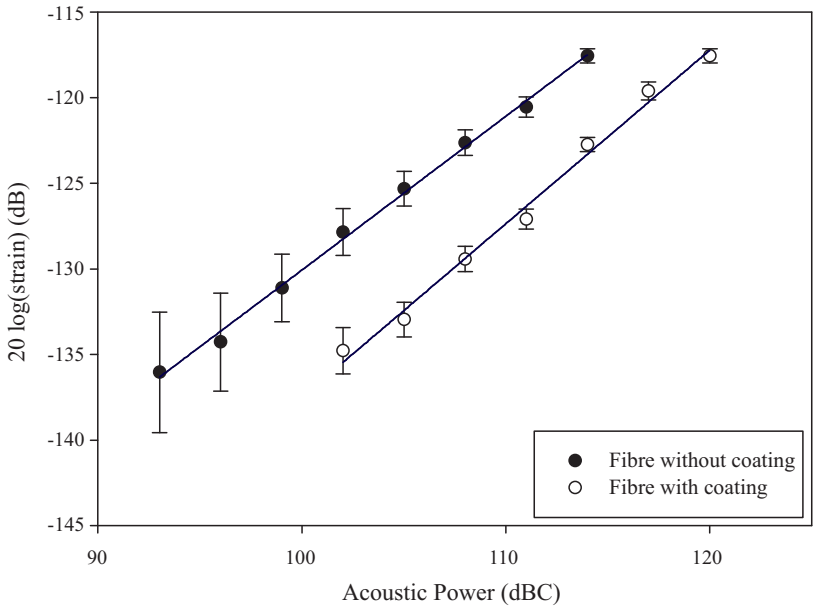

Figure 4.5: Pressure-induced strain on the two sensing fibres (one with $165\mu m$ *coating and the other without coating) versus sound-pressure level as a result of a* $800Hz$ *acoustic wave.*

polymer coating and the fibre without coating) to a range of $800Hz$ sinusoidal sound waves with different acoustic pressure-levels. The vertical axis of this figure which represents the magnitude of the induced strain is plotted in log scale to correspond to the acoustic pressure level which was measured in dB.

Figure 4.6 shows the sound-pressure level (SPL) measured by the microphone and the distributed sensor as a function of the distance between the acoustic source and the sensing fibre. The blue curve on this diagram represents the microphone output (in mV) while the white squares represent the sensor output (in $\mu\varepsilon$). This experiment was carried out using the uncoated fibre as the sensing medium.

Figure 4.7 shows the frequency response of the sensor (red-line) and that of the microphone (blue-line) to a recorded voice which was comprised of several frequency components. The recorded voice was played back through the loud speaker.

4.5 Discussions

The two peaks of figure 4.4 correspond to the two sources of perturbation along the sensing fibre including the disk PZT at $430m$ and the loud speaker at $750m$ from the front end of the sensing fibre. The frequency, location, and amplitude of the two peaks in this 3D diagram are accurately indicating those of the PZT and the speaker. The sharpness of the peaks indicates the high frequency resolution of the sensor. This resolution is determined by the pulse repetition rate and the total data collection time. For the current experimental setup with a $20\mu s$ pulse repetition rate and total data acquisition

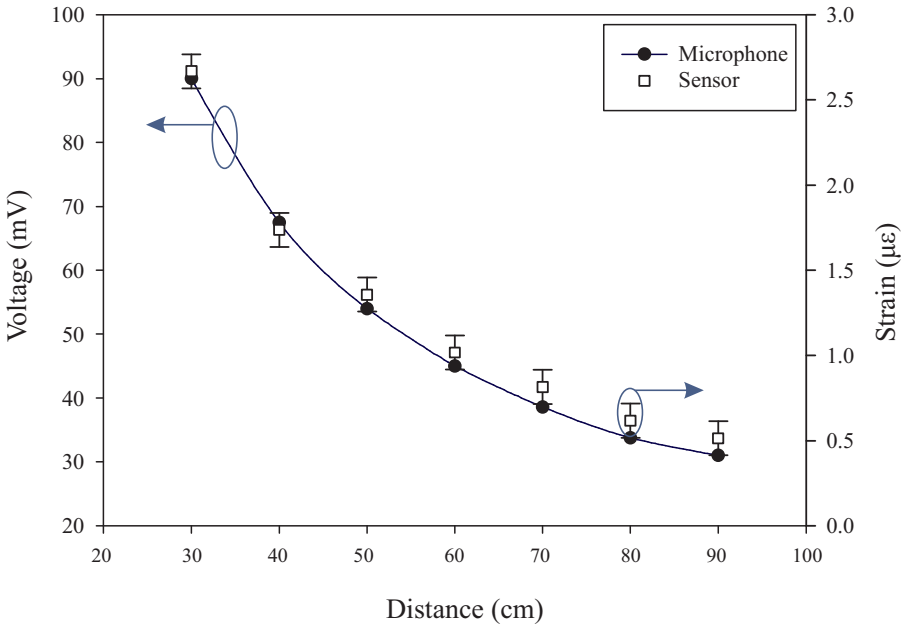

Figure 4.6: The sound-pressure level measurement using the microphone (black circles) and the distributed acoustic sensor (white squares) as a function of the distance between the acoustic source and the sensing fibre.

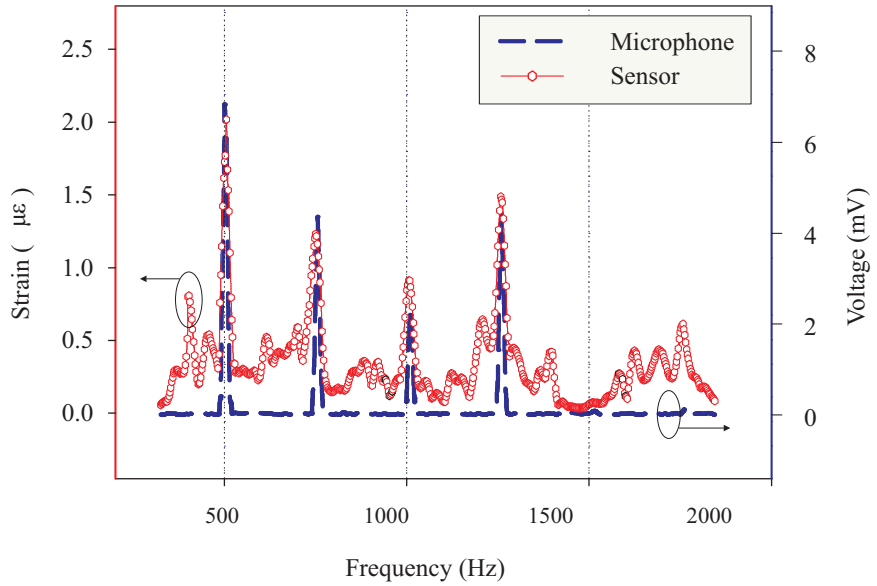

Figure 4.7: Frequency response of the sensor (red-line) and that of the microphone (blue-line) to multiple-frequency sound of a human voice played through the loud speaker for the section of the fibre attached to the polystyrene sheet.

time of $100ms$, the theoretical frequency resolution of $10Hz$ was calculated. This value was confirmed by the experimental results. The frequency range of the sensor was measured to be between $100Hz$ to $5000Hz$. The evaluation of the sensor output showed a lower SNR for higher frequency sound waves, an outcome which is in agreement with strain-frequency curves on figure 4.2. In this figure, it was shown that, for any given gauge length, the net induced strain on the sensing fibre decreases with the increasing frequency of sound wave.

Figure 4.5 shows a linear relationship between the sound-pressure level in dB(C) (C-weighted pressure level in dB) and the *log* of the sensor output for $800Hz$ sinusoidal sound wave for both fibres. Similar experiments at other frequencies (*i.e.* $550Hz$, $1100Hz$, $1500Hz$, and $3000Hz$) exhibited the same linear characteristic. These results indicate that the amplitude of the sensor output is a direct measurement of the net induced strain to the sensing fibres and is independent of the applied frequency. The slope of the fitted line is measured to be unity with an accuracy of $\pm 4\%$. With both axes represented on logarithmic scale, the unity slopes of the two traces in the diagram verify the linear relationship between the pressure-induced strain and the phase-shift described by equation 4.2 ($\Delta\phi = \mathcal{K}.P \;\rightarrow\; log(\Delta\phi) = log(\mathcal{K}) + log(P)$ where $\mathcal{K}$ is a constant). Figure 4.5 also demonstrates that the two sensing fibres have different SPL ranges. The minimum and maximum detectable SPL using the uncoated sensing fibre was measured to be $93dB(C)$ and $114dB(C)$ respectively while the SPL range for the coated fibre was measured to be between $102dB(C)$ and $120dB(C)$. The SPL range of the sensor depends on the degree of the coupling between the sensing fibre and the polystyrene sheet. For the uncoated fibre, the fibre was in direct contact with the polystyrene sheet

and therefore the strain on the polystyrene sheet was directly transferred to the fibre while for the polymer-coated fibre, the coating acted as an intermediary layer between the polystyrene and the fibre. As a result, a fraction of the induced strain was transferred to the fibre. Therefore, the uncoated fibre showed a higher sensitivity to the variation in SPL while the coated fibre demonstrated a larger SPL range. The minimum detectable strain for both fibres was measured to be $500n\varepsilon$ with an accuracy of $100n\varepsilon$.

Figure 4.6 demonstrates the response of the sensor to an acoustic source with a uniform output at different distances. On this diagram, the blue curve which illustrates the output of the microphone verifies the inverse distance law for sound pressure ($P \propto 1/r$). It can be seen that the output of the distributed sensor is consistent with the output of the microphone which indicates that a modified version of this experimental setup can be used to measure the distance between the acoustic source and the sensing fibre (in addition to location, amplitude, and frequency of the acoustic source).

The frequency response of the sensor output shown in figure 4.7 shows a good agreement with that of the microphone. For every frequency component on the microphone output, there is one frequency component on the sensor output which matches that of the sensor. However, in addition to a higher noise level, a few other frequency components are evident on the FFT of the sensor output. There are two reasons for the disparity between the two frequency responses; the first, reason is the difference between the sensing mechanism of the microphone and the distributed sensor. The distributed sensor measures the integration of the acoustically induced strain over the spatial resolution of the sensor (*i.e.* $1m$) whilst the microphone output only shows the acoustic vibration at a single point in the middle of the polystyrene sheet. The second reason for the disparity is due to the difference between the data acquisition process of the microphone and of the sensor. The microphone data acquisition period was set to twice as long as that of the sensor. In addition, the data-averaging time for the microphone was 100 times longer. As a result, the output of the microphone was much less noisy in comparison with that of the sensor with a sampling period of $100ms$.

4.6 Conclusions

A distributed optical fibre sensor has been demonstrated which is capable of detecting both longitudinal and transverse strains along the fibre using the φ-OTDR technique. The experimental results indicate that the sensor can simultaneously measure the frequency and amplitude of multiple dynamic perturbations with a spatial resolution of $1m$. It has been shown that the output of the sensor is a linear function of the sound-pressure level and that the output of the sensor is consistent with the inverse distance law. In addition, it has been demonstrated that the sensor is capable of detecting and accurately reproducing an acoustic wave with multiple frequencies in the frequency range of $100Hz$ to $5000Hz$ and with a frequency resolution of $10Hz$. Finally, it has been shown that the SPL range of the sensor can be adjusted by changing the thickness of the coating

which covers the sensing fibre.

In the previous two chapters, optical fibre was employed as the sensing element to directly measure the strain distribution along its length. The capability of measuring the distributed dynamic strain is a powerful tool which can be used to form a number of novel distributed sensors capable of measuring other variable physical phenomena. One such distributed sensor is introduced in the next chapte; here a distributed magnetic field sensor is developed by coupling an optical fibre with a magnetostrictive Nickel wire.

Bibliography

[1] J. H. Cole, R. L. Johnson and P. G. Bhuta, " Fiber optic detection of sound," Journal of Acoustic Society of America, vol. 62, pp. 1136-1138, 1977.

[2] J. A. Bucaro, H. D. Dardy and E. F. Carome, "Fiber optic hydrophone," Journal of Acoustic Society of America, vol. 62, pp. 1302-1304, 1977.

[3] J. P. Kurmer, S. A. Kingsley, J. S. Laudo, and S. J. Krak, "Distributed fiber optic acoustic sensor for leak detection," Proc. SPIE 1586, Distributed and Multiplexed Fiber Optic Sensors, no. 117, Jan. 1991.

[4] G. B. Hocker, "Fiber-optic sensing of pressure and temperature," Applied Optics, vol. 18, pp. 1445-1448, 1979.

[5] G. B. Hocker, "Fibre optic acoustic sensors with composite structure: an analysis," Applied Optics, vol. 18, pp. 3679-3683, 1979.

Chapter 5

Dynamic Magnetic Field Sensor Based on Magnetostriction

5.1 Introduction

Magnetic field sensors are of significant importance in many areas of engineering and science ranging from monitoring brain activity to measuring the electric current in high-power transmission lines. So far, a wide range of mostly single-point magnetic field sensors have been developed using a number of electrical and optical techniques. Machines such as magnetic resonance imaging (MRI) scanners rely on a large array of single-point sensors for imaging purposes. Distributed optical fibre magnetic field sensors (DOFMS) can replace an array of point sensors with a single strand of optical fibre.

As previously mentioned in chapter 2, Palmieri *el at.* [1] were the first to experimentally demonstrate a distributed magnetic field sensor, based on the polarization of the backscattered light. However, the proposed sensor had a limited sensing range ($15m$) and with repetition rate of $10s$, it was suitable only for DC and quasi-DC magnetic field sensing. In addition, it was shown that the studies on magnetostrictive-based optical fibre magnetic field sensors have been limited to either single-point sensors [2–5] or quasi-distributed sensors [6, 7].

In this chapter, a magnetostrictive-based distributed magnetic field sensor is demonstrated which is capable of quantifying magnetic fields along $1km$ of sensing fibre with a spatial resolution of $1m$. The sensing mechanism of the proposed sensor is based on measuring the strain of an optical fibre which is mechanically coupled to the magnetostrictive material, a Nickel wire, using the strain measurement technique described in chapter 3.

5.2 Principles

The principle of operation of the sensor is based on measuring the magnetic-field-induced strain on an optical fibre coupled with a magnetostrictive material. The role of the

magnetostrictive material is to convert the magnetic field into mechanical strain or stress which then can be sensed using a distributed strain sensor. Therefore, to form the sensing element, a magnetostrictive material in the form of a wire is coupled to the sensing fibre. The sensitivity of the sensor to magnetic fields is determined by the value of the magnetostriction coefficient of the wire, the direction of the magnetic field with respect to the direction of the wire, and the arrangement in which the fibre is coupled with the wire.

The value of the magnetostriction coefficient of the magnetostrictive wire determines the strain on the sensing fibre for a magnetic field at a certain intensity. Since the dynamic strain sensor introduced in chapter 3 has a fixed strain range, the magnetostriction coefficient of the wire within the sensing element can be adjusted to develop sensors with different magnetic field intensity ranges.

With an assumption that the fibre is wrapped helically around the wire of radius r, the change in the radius of the wire due to $\Delta\ell$ metre elongation of the wire is give by

$$\Delta r = \mu_p \, r \, \varepsilon_w = \mu_p \, r \, \frac{\Delta\ell}{\ell} \tag{5.1}$$

where μ_p is the Poisson's ratio of the wire and ℓ is the helix period. Considering the fact that $r \ll \ell$ and with Poisson's ratio much smaller than one ($\mu_p = 0.29$ for Nickel wire for instance), it is clear that the changes in the radius of the wire are much smaller than the changes in the length of the wire. Therefore, the changes in the length of the sensing fibre due to variation in the radius of the magnetostrictive wire as a result of a magnetic field can be neglected. Consequently, if the magnetic field $\mathbf{B}$ forms an angle θ with the axis of the wire laid along the x axis (figure 5.1), the sensing element of the sensor is sensitive only to the component of the $\mathbf{B}$ parallel to the x axis,

$$\mathbf{B}_X = \mathbf{B} \, \cos(\theta). \tag{5.2}$$

Moreover, the strains of the sensing fibre and the magnetostrictive wire are not equal due to the helical configuration in which the fibre is coupled with the wire. If an infinitesimally small section of the fibre makes an angle φ with the longitudinal axis of the wire laid along the x-axis (figure 5.1), the strain of the fibre (ε_f) due to elongation of wire is given by

$$\varepsilon_f = \varepsilon_w \, \cos(\varphi) = \frac{\Delta\ell}{\ell} \cos(\varphi) \tag{5.3}$$

where ε_w is the strain of the wire. From this equation, it can be seen that for $\varphi = 0$, the strain induced on the fibre would be equal to that on wire. However, with the fibre attached to the wire in a helical manner, the fibre strain is smaller than that of the wire. Using equations 5.2 and 5.3, the relationship between the applied magnetic field

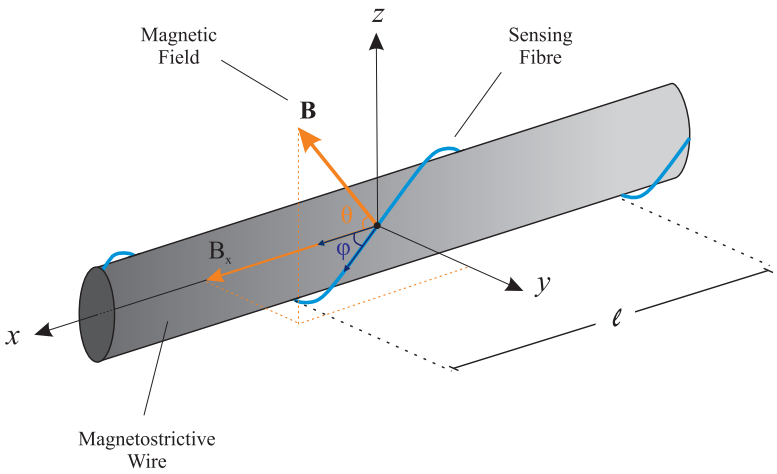

Figure 5.1: Schematic of a section of the sensing element of the sensor.

and the fibre strain can be written as

$$\varepsilon_f = \frac{\Delta\ell}{\ell}\cos(\varphi) = \epsilon_M B_X \cos(\varphi) = \epsilon_M B \cos(\varphi)\cos(\theta) \tag{5.4}$$

where ϵ_M is the magnetostrictive coefficient of the wire and $B = |\mathbf{B}|$.

The principle of the strain measurement is based on comparing the strain-induced phase variation between two segments of the fibre as described in chapter 3. Figure 5.2 demonstrates the strain-sensing principle of the sensor. The concept is similar to the

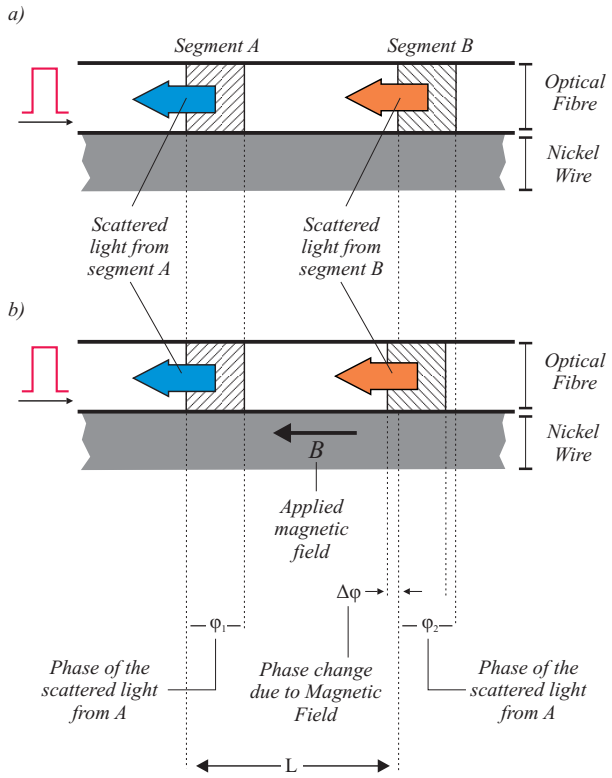

Figure 5.2: Principle of operation of distributed magnetic field sensor.

one described in the previous chapter except that the strain induced on the fibre in this sensor is due to the magnetic-field-induced strain on the magnetostrictive wire rather than the acoustic vibrations.

In the analysis of the strain sensor described in chapter 3, it was shown that the output of the differentiate and cross-multiplying demodulator, Φ, has a linear relationship with the strain on the fibre

$$\Phi = \sqrt{3}\,\Delta\phi = \sqrt{3}\,\frac{4\pi}{\lambda}\,L_0\varepsilon_f \tag{5.5}$$

where L_0 is the initial separation between the two sections of the sensing fibre as shown in figure 5.2 and λ is the wavelength of the interrogating pulse. By combining equations 5.4 and 5.5, the relationship between the magnetic field and the sensor output is given as

$$\Phi = \frac{4\sqrt{3}\pi\,\epsilon_M}{\lambda}\,L_0\,B\,\cos(\theta)\,\cos(\varphi). \tag{5.6}$$

5.3 Experimental Arrangement

5.3.1 Experimental Setup

Figure 5.3 shows a schematic diagram of the experimental setup. The pulse generation and backscattered light detection procedure of this experimental setup is similar to the arrangement described in chapter 3.

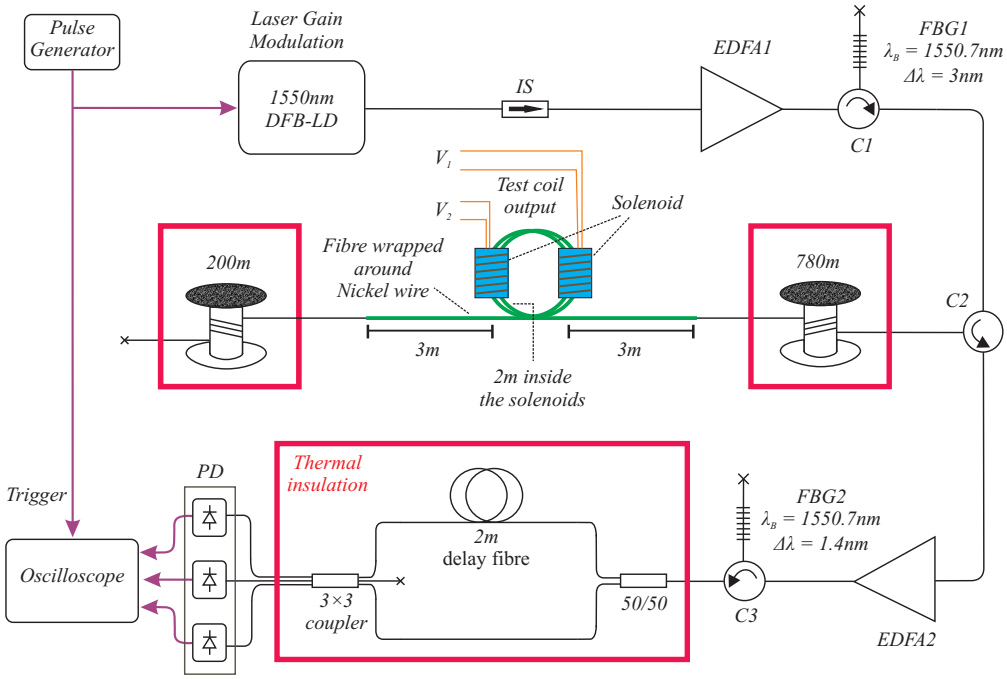

Figure 5.3: Experimental setup. EDFA: Erbium-doped fibre amplifier, PD: photodetector, FBG: fibre Bragg grating, DFB: distributed feedback, IS: isolator; V_1 and V_2; Outputs of test coils.

The sensing fibre, on the other hand, was comprised of three segments including an $8m$ length of magnetostrictive sensing element as well as $780m$ and $200m$ of thermally isolated fibres which were added before and after the sensing element respectively to form a $1km$-long distributed sensor. The sensing element was formed by helically wrapping $8m$ of single mode optical fibre around $8m$ of Nickel wire ($1mm$ diameter) with a helix pitch of $0.5m$ and binding the two elements using epoxy glue. The epoxy glue was used to yield a flexible sensing element but with the fibre firmly secured.

The magnetostriction curve of Nickel wire presented in figure 5.4 is an even function. Therefore, the elongation of the wire depends on the magnitude of the magnetic field applied on the wire as well as the intrinsic magnetic moment of the wire. Applying an AC magnetic field on an unmagnetized Nickel wire results in a non-linear strain on the wire with a frequency twice that of the applied magnetic field. Therefore, to design a sensor with a linear relationship between the applied magnetic field and the magnetic-field-induced strain, a pre-magnetized Nickel wire was used in the setup. Using a Gauss-meter, an intrinsic magnetic field of $4Gs$ (the red dot on the diagram of figure 5.4) was measured which corresponds to magnetostrictive coefficient of $\sim 150n\varepsilon/Gs$.

The middle $2m$ of the sensing element was placed inside two separate $55mm$-long solenoid coils ($27\,turn/mm$) as shown in figure 5.5(a). The coils were used to generate an AC magnetic field parallel to the direction of the Nickel wire. For the magnetic-field-induced strain to be additive along the sensing fibre, the current flow inside the solenoids were arranged to generate magnetic fields with opposite directions and hence to form magnetic field lines parallel with the sensing element (figure 5.5(b)). The rest of the sensing element (*i.e.* $3m$ on either side of the $2m$) was left outside the solenoid coils in order to demonstrate the distributed nature of the sensor.

The manipulation, detection, and signal processing procedure of the backscattered

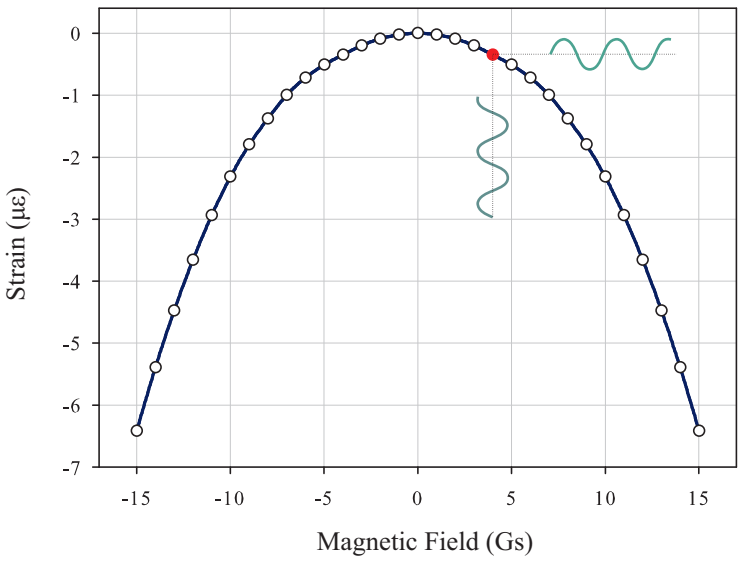

Figure 5.4: Magnetostriction curve (blue trace) and the intrinsic magnetic moment (the red dot) of the Nickel wire used in the experimental setup [8].

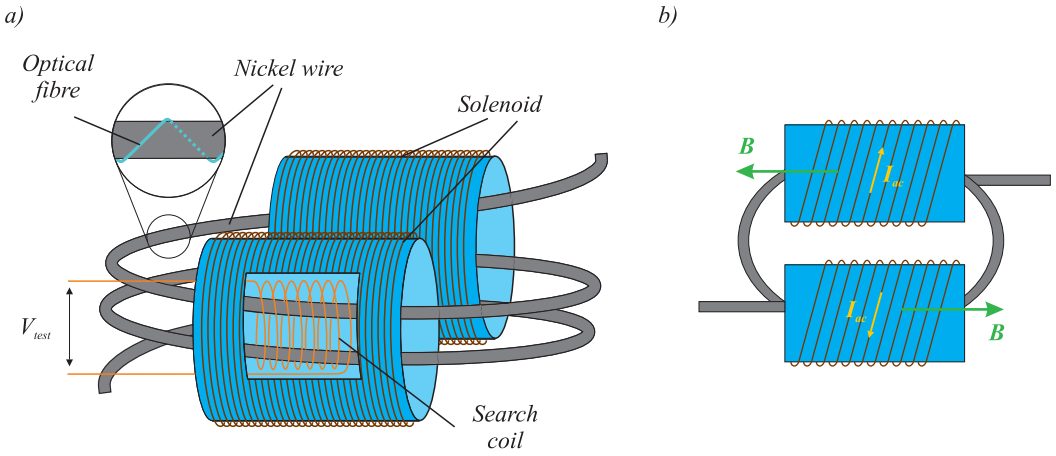

Figure 5.5: Magnetic field source element used in the experimental setup to generate AC magnetic field.

traces were similar to that of the experimental setup studied in chapter 3.

5.3.2 Experimental procedure

A MZI arrangement was initially used to characterize the response of the sensing fibre to the magnetic field for a range of frequencies and intensities. In order to generate the desired magnetic field, two identical driver circuits were designed and assembled to drive the two solenoid coils of the experimental setup. The schematic of the driver circuit is shown in figure 5.6. The circuit was comprised of a signal generator, an emitter-follower amplifier, and an RLC resonant circuit. The inductor L shown in the schematic of figure 5.6 represents the solenoid used in the experimental setup. To maximize the current flow in the solenoids, the impedance of the capacitors were set to match that of the solenoids ($\mathbb{Z}_L = \mathbb{Z}_C^*$). Therefore, to generate a magnetic field with frequency f, the value of the capacitors were set to $C = L\omega^2$ where $\omega = 2\pi f$. Test coils were placed inside each solenoid to monitor the average magnetic field inside the solenoids.

After characterization, the sensing fibre was spliced to the DOFMS setup as shown in

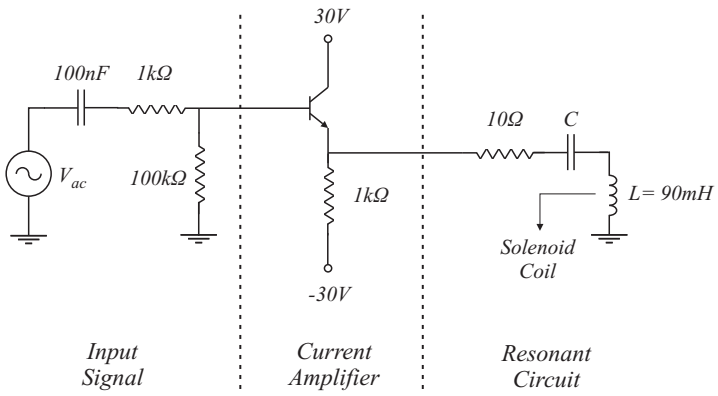

Figure 5.6: Schematic of the circuit used to drive the magnetic coils.

figure 5.3. The driver circuits were initially adjusted to generate $1200Hz$ magnetic field and data were collected for magnetic fields ranging from $1Gs$ to $8Gs$ at a repetition rate of $10\mu s$. 20,000 traces were captured during each experimental run which is equivalent to a data acquisition period of $200ms$. To determine the frequency response of the sensor, the driver circuits were modified to generate magnetic fields with a fixed magnitude over a range of frequencies spanning from $50Hz$ to $5000Hz$.

5.4 Experimental Results

The 3D diagram of figure 5.7(a) shows the FFT of the phase-detector output for a $1150Hz$ magnetic field with a magnitude of $7Gs$. The two horizontal axes at the bottom of the diagram represent the distance along the sensing fibre and the frequency

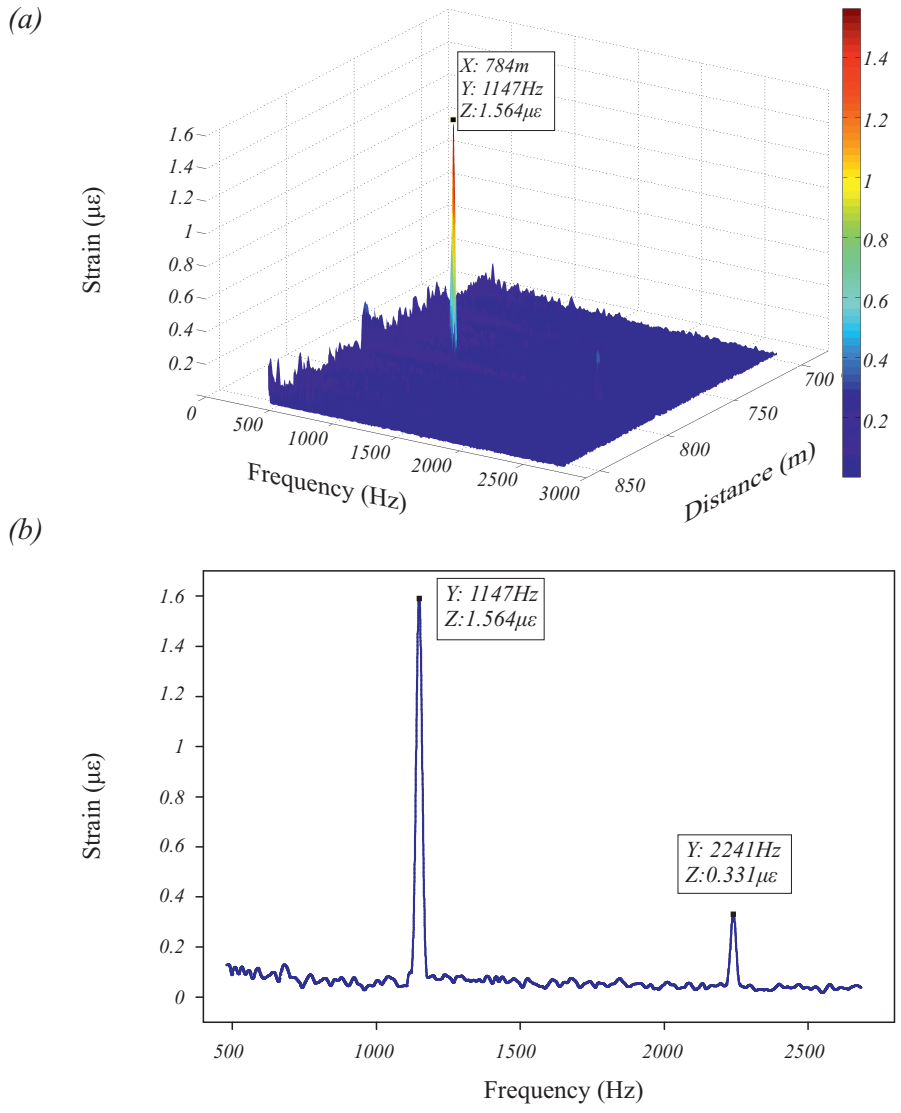

Figure 5.7: (a) 3D plot of FFT of the phase-detector output for the data points between 700m and 850m. (b) A 2D view of the 3D plot at the location of the peak.

components of perturbation. The vertical axis of the diagram represents the magnitude of the strain. The peak in this figure indicates a $1147Hz$ sinusoidal perturbation at a distance of $784m$ from the front-end of the sensing fibre. In addition, the amplitude of the peak indicates a strain of $1.56\mu\varepsilon$ in that section of the sensing fibre. For clarity, a 2D view of peak in the 3D plot is shown in figure 5.7(b). A second peak is observed at $2291Hz$, *i.e.* at the second harmonic of the magnetic field frequency.

Figure 5.8 depicts a 2D cross section of the 3D plot shown in figure 5.7 for the peak at $1150Hz$ as a function of distance. This plot demonstrates the effect of the magnetic-field-induced strain along a $140m$ section of the sensing fibre. The start and end points of the peak shown in this plot are at $781.7m$ and $786.4m$, respectively.

Figure 5.9 shows the response of the sensing fibre to $1200Hz$ magnetic fields at different intensities. The solid line represents the DOFMS output while the dashed-line shows the results obtained using the MZI.

Figure 5.10 shows the frequency response of the sensing fibre to sinusoidal magnetic fields with a fixed magnitude over a range of frequencies spanning from $50Hz$ to $5000Hz$. The solid line shows the magnetic-field-induced strain measured using MZI while the circles are showing the DOFMS output.

5.5 Discussion

5.5.1 Sensor Response to Dynamic Magnetic Field

The larger peak in figure 5.7 accurately indicates the location and frequency of the applied magnetic field within the sensing resolution of the sensor. In addition, the

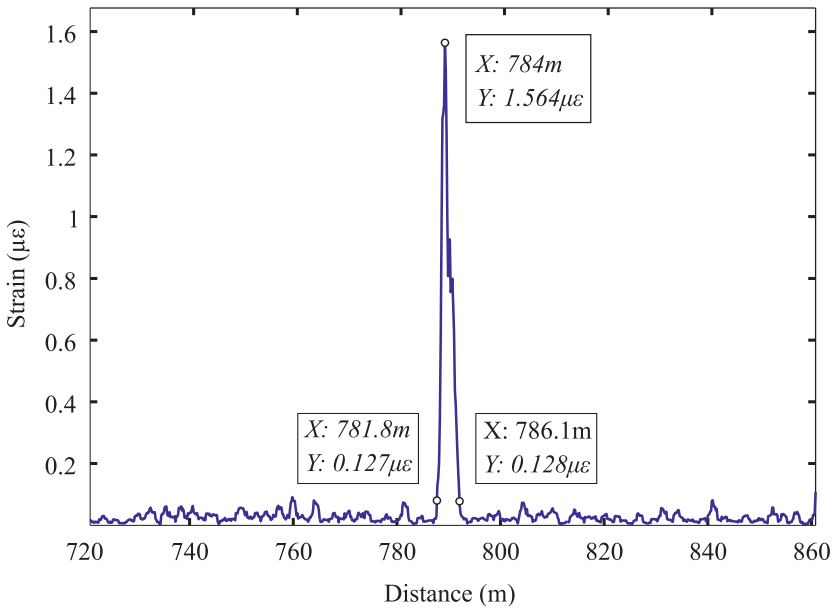

Figure 5.8: A 2D view of the 3D plot of figure 5.7 as a function of distance at the frequency of $1150Hz$.

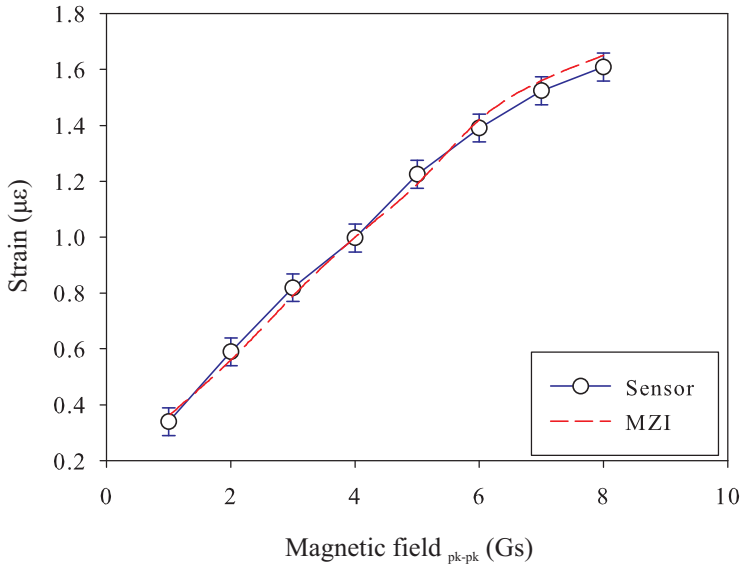

Figure 5.9: The response of the sensing fibre to $1200Hz$ *sinusoidal magnetic field for a range of different intensities. The solid line shows the DOFMS output while the dashed-line represents the results obtained using MZI.*

induced strain of $1.56\mu\varepsilon$ closely matches the results obtained from the MZI experiment, *i.e.* a phase-shift of 4π radians for $2m$ of sensing fibre. Both peaks vanished when the magnetic field was switched off. Therefore, it was concluded that the smaller peak in figure 5.7 is the second harmonic of the magnetically-induced strain on the sensing fibre. The frequency of the peak shown in this figure is within the $5Hz$ predicted frequency resolution.

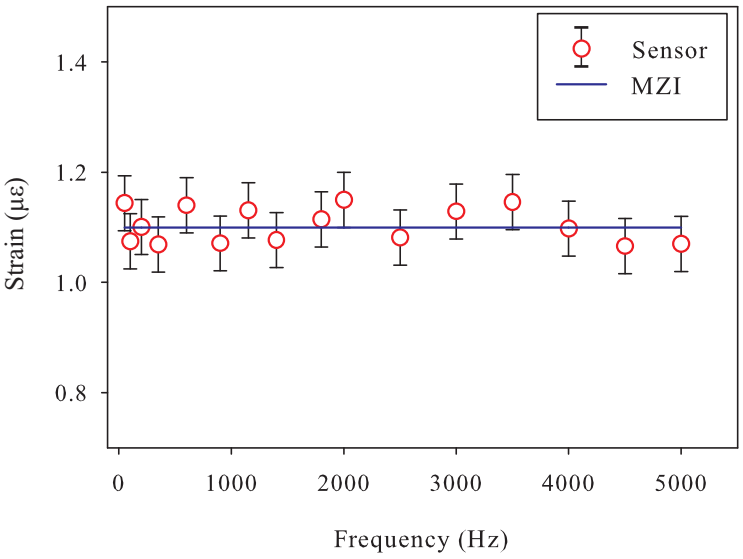

Figure 5.10: The response of the sensing fibre to sinusoidal magnetic fields with a fixed magnitude and a range of frequencies spanning from $50Hz$ *to* $5000Hz$*. The solid line shows the magnetic-field-induced strain measured using MZI while the circles are showing the DOFMS output.*

The $4.3m$ width of the peak shown in figure 5.8 demonstrates the effect of the magnetic field on the sensing element. The middle $4m$ of this spatial distribution is due to the interaction of the $10ns$ light pulse with $2m$ of the sensing element within the solenoids while the additional $0.3m$ of the spatial distribution is due to the interaction of the magnetic field around the solenoids with the sensing elements outside the cavity of the solenoids.

Figure 5.9 demonstrates that the output of the sensor is linearly proportional to the intensity of a $1200Hz$ magnetic field, a result which is in good agreement with the characterization results obtained using a MZI. Similar experiments at a number of different frequencies verified that the sensor's intensity measurement is independent of the frequency of the applied magnetic field. An amplitude resolution of $0.3Gs$ was determined for the linear region of the plot of figure 5.9 which corresponds to a strain resolution of $50n\varepsilon$.

In order to explain the nonlinear behaviour of the sensing fibre for magnetic fields with intensity higher than $7Gs$, it is important to note that the distributed sensor measures the average intensity of the magnetic field along the gauge length of the sensing fibre. Consequently, while a large portion of the sensing fibre is exposed to a magnetic field with moderate intensity, the portion of the sensing fibre in the middle of the solenoids experiences magnetic fields with much higher intensity. Therefore, considering the nonlinear relationship between the intensity of the magnetic field and the strain rate of the Nickel wire (figure 5.4), the deviation from the linear response shown in figure 5.9 originates from the sections of the sensing element under the highest intensity of the magnetic fields, *i.e.* the sections in the middle of the solenoids.

Finally, figure 5.10 demonstrates a good correlation between the sensor and MZI outputs over a frequency range of $50Hz$ to $5000Hz$ which demonstrates that the sensor is capable of measuring the magnitude of a magnetic field independent of its frequency.

5.5.2 The Effect of the Diameter and Properties of the Magnetostrictive Wire on the Sensor's Sensitivity

Using a material with high magnetostriction coefficient such as Nickel or Terfenol-D allows for detection of weaker magnetic fields. To obtain the highest magnetic field sensitivity, the fibre should be coupled parallel to the magnetostrictive wire. Furthermore, this technique can be used to measure larger magnetic fields either by using wires with lower magnetostriction coefficient such as Iron or by wrapping the fibre around the wire in such a way that the fibre forms a low-pitch helix around the wire. This is equivalent to increasing the value of φ in equation (5.3).

To assess the sensitivity of the sensor as a function of the diameter of the magnetostrictive wire, the effect of the fibre on the magnetically-induced strain in the wire needs to be analyzed. The length of a magnetostrictive wire of length ℓ under the

influence of a magnetic field can be written as

$$\ell' = (1 + \epsilon_M\, B)\, \ell. \tag{5.7}$$

Coupling a fibre to the wire in a form of a long helix reduces the elongation of the wire due to the extra force required to stretch the fibre. With an assumption that the length of the wire reduces to ℓ" as a result of the fibre (ℓ" $< \ell'$), the forces on the fibre and wire are given by

$$\begin{cases} F_w = \mathbb{E}_w\, A_w\, (\ell" - \ell')/\ell' \\ \\ F_{fib} = \mathbb{E}_{fib}\, A_{fib}\, (\ell" - \ell)/\ell \end{cases} \tag{5.8}$$

where $\mathbb{E}_w$ and $\mathbb{E}_{fib}$ are the Young's modulus of the wire and fibre respectively, while A_w and A_{fib} are the cross-sectional area of the two. Since F_w and F_{fib} are two equal forces which act in the opposite directions, combining equations 5.7 and 5.8 gives

$$\frac{\mathbb{E}_w\, A_w\, [\ell" - (1 + \epsilon_M\, B)\ell]}{(1 + \epsilon_M\, B)} = \mathbb{E}_{fib}\, A_{fib}\, (\ell - \ell"). \tag{5.9}$$

Rearranging this equation for ℓ'' results in

$$\ell" = (1 + \epsilon_M\, B)\ell\, \frac{\mathcal{R} - 1}{\mathcal{R} - (1 + \epsilon_M\, B)}, \tag{5.10}$$

where

$$\mathcal{R} = \frac{\mathbb{E}_w\, A_w}{\mathbb{E}_{fib}\, A_{fib}} \tag{5.11}$$

is the ratio between the product of the Young's modulus and the cross-sectional area of the wire and that of the fibre. Replacing equation 5.7 in 5.10 gives

$$\ell" = \ell'\, \frac{\mathcal{R} - 1}{\mathcal{R} - (1 + \epsilon_M\, B)}. \tag{5.12}$$

Using this equation, the effect of the fibre on the elongation of the magnetostrictive wire can be analyzed. For Nickel wire with $1mm$ diameter and standard SMF fibre the ratio $\mathcal{R}$ would be

$$\mathcal{R} = \frac{205GPa \times (1mm)^2}{16GPa \times (250\mu m)^2} = 205\,.$$

Since the value of the magnetostrictive coefficient of Nickel is in the order of a few micro-strains per Gauss, it can be shown that $(1 + \epsilon_M\, B) \ll \mathcal{R}$. Therefore, equation 5.12 can be simplified to

$$\ell" = \ell'\, \frac{\mathcal{R} - 1}{\mathcal{R}} \cong \ell' \tag{5.13}$$

which shows that, since the Young's modulus of the Nickel wire is much higher than that of the optical fibre, the variation in the diameter of the Nickel wire has a small effect on the strain rate of the sensing fibre.

5.5.3 Signal Processing Limitations

As briefly mentioned in chapter 3, since discrete data are used for the signal processing procedure, it is the differentiate and cross-multiplying demodulator which imposes a limitation on the frequency range of the sensor. For the current experimental setup, this limitation was experimentally determined to be $50Hz \sim 5000Hz$. For frequencies lower than $50Hz$ the output of the demodulator was noisy due to the frequency resolution of the demodulator which is determined by the data acquisition period of $200ms$. For frequencies greater than $5000Hz$, on the other hand, the demodulator attenuates the measured signal. This attenuation can be seen in the frequency response of the differentiate and cross-multiplying demodulator shown in figure 5.11. This figure shows the frequency response of the differentiate and cross-multiplying demodulator for an input signal with 1.5π phase-shift for two different sampling rates. According to this figure, by allowing a tolerance of $\pm 5\%$, the cut-off frequency of the demodulator for sampling rates of $10\mu s$ and $20\mu s$ are $5000Hz$ and $2500Hz$, respectively. The upper limit of the sensor's frequency range can be increased by implementing an improved signal processing procedure.

5.6 Conclusions

In this chapter, a distributed optical fibre dynamic magnetic field sensor has been demonstrated which is capable of quantifying magnetic fields along $1km$ of the sensing fibre with a spatial resolution of $1m$. It has been shown that, in its current form, the sensor has a frequency range of $50Hz$ to $5000Hz$ and a frequency resolution of $\pm 5Hz$. The

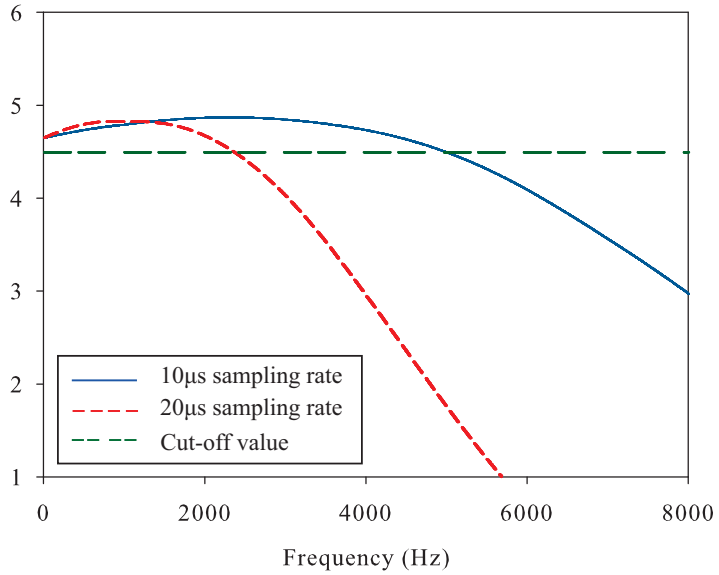

Figure 5.11: The differentiate and cross-multiplying demodulator frequency responses to an input signal with 1.5π *phase-shift at sampling rate of* $10\mu s$ *(solid blue line) and* $20\mu s$ *red dashed-line.*

sensor has demonstrated an intensity resolution of $0.3Gs$ ($\equiv 0.05\mu\varepsilon$) over the magnetic field range of $1Gs$ to $8Gs$. The proposed technique has the potential to be used in a wide range of magnetic field intensities from a few tens of mGs to hundreds of Gauss by changing the compound of the magnetostrictive element in the sensing fibre. This sensor can be used in a variety of applications ranging from monitoring the state of electrical motors or generators to mapping magnetic anomalies.

So far, the powerful technique of using an IMZI combined with the differentiate and cross-multiplying demodulation has been used to measure strain-induced phase changes of the coherent Rayleigh backscattered signal. The output of an IMZI is also dependent on the wavelength of the detected light. Therefore, the same technique can be used to measure the changes in the wavelength of backscattered light. The next chapter explores the possibility of modifying the current experimental setup to devise a sensor capable of converting the strain-induced frequency shift of the Brillouin backscattered light into intensity variation.

Bibliography

[1] L. Palmieri and A. Galtarossa, "Distributed fiber optic sensor for mapping of intense magnetic fields based on polarization sensitive reflectometry," Proceedings of SPIE vol. 8351, 835131, 2012.

[2] S. C. Rashleigh, "Magnetic-field sensing with a single-mode fiber," Optics Letters, vol. 6, pp. 19-21, 1981.

[3] J. P. Willson and R. E. Jones, "Magnetostrictive fiber-optic sensor system for detecting dc magnetic fields," Optics Letters, vol. 8, pp. 333-335, 1983.

[4] Miroslav Sedlar, Ivan Paulicka, and Michael Sayer, "Optical fiber magnetic field sensors with ceramic magnetostrictive jackets," Applied Optics, vol. 35, pp. 5340-5344, 1996.

[5] A. Yariv and H. V. Winsor, "Proposal for detection of magnetic fields through magnetostrictive perturbation of optical fibers," Optics Letters, vol. 5, pp. 87-89, 1980.

[6] P. M. Cavaleiro, F. M. Araujo, and A. B. L. Ribeiro, "Metal-coated fibre Bragg grating sensor for electric current metering," Electronics Letters, vol. 34, pp. 1133 - 1135, 1998.

[7] M Li, J. Zhou, Z. Xiang, and F. Lv, "Giant magnetostrictive magnetic fields sensor based on dual fiber Bragg gratings," Networking, Sensing and Control IEEE Proceedings, pp. 490-495, 2005.

[8] J. R. Hobbie, "Magnetostriction with Small Magnetizing Fields," Physical Review Letters, vol. 19, pp. 456-566, 1922.

Chapter 6

Dynamic Strain Sensor Based on Direct Detection of Spontaneous Brillouin Scattering

6.1 Introduction

The concept of imbalanced Mach-Zehnder interferometer (IMZI) and how the path-imbalance can be utilized to measure the phase of the backscattered light was demonstrated in the previous chapters. The focus of those chapters was on measuring the strain along the sensing fibre using the coherent backscattered Rayleigh signal. The aim of the present chapter, though, is to exploit the wavelength-dependent characteristic of an IMZI to develop a Brillouin-based dynamic strain sensor.

Throughout the years, different techniques have been employed to exploit the inelastic nature of the Brillouin scattering to design sensors with high spatial resolution [1–3] or with long sensing range [4–6]. Despite extensive research to improve Brillouin-based distributed optical fibre sensors (DOFS) as a DC and quasi-DC sensor, there has been little progress in developing long-range dynamic strain DOFS based on Brillouin scattering.

In chapter 2, a number of studies on Brillouin-based dynamic strain measurement based on BOCDA [7,8] and BOTDA [9,10] sensing techniques were reviewed. Although capable of quantifying perturbations, it was shown that neither of the two techniques can be used for detection of dynamic vibrations over long sensing and frequency ranges due to their slow sensing mechanism which requires the scanning of the the sensing fibre in small frequency steps. The BOTDA technique has an additional drawback in the form of a power transfer between the CW pump light and counter-propagating pulse in which the strain distribution along the sensing fibre can influence the strain measurements at other points of the fibre.

Brillouin optical time-domain reflectometry (BOTDR) using coherent detection of the weak spontaneous Brillouin signal overcomes this problem. However, the process of

identifying the peak Brillouin frequency shift has proved to be relatively time consuming, as the Brillouin spectrum was built up from multiple BOTDR traces collected at different frequencies and then post processed to identify the peak Brillouin frequency shift. This limited the bandwidth of the strain measurement to DC or quasi-DC measurements.

In this chapter, a Brillouin-based DOFS is introduced which is capable of measuring low frequency dynamic strains. The proposed technique is based on the concept first introduced by Kee *et al.* [11] which exploits the capability of an IMZI to convert the Brillouin frequency shift to optical intensity variations at the photodetector. However, the previously used 2×2 coupler in the IMZI of that setup is replaced by a 3×3 coupler to allow the use of the differentiate and cross-multiply demodulation scheme described in chapter 3. The advantage of utilizing this demodulation scheme is that the need for locking the MZI close to its quadrature position is now eliminated. Consequently, this technique eliminates the requirement of confining the strain-induced frequency shift to the linear region around the quadrature point of the interferometer. This allows the free spectral range (FSR) of the MZI to be reduced, thereby increasing the strain responsivity but still allowing large strains to be measured. In addition, since the technique is based on Brillouin optical time-domain reflectometry (BOTDR), the measurement at each point of the sensing fibre is independent of the temperature and strain along the rest of the fibre.

6.2 Principles

In chapter 3, it is demonstrated that for an IMZI with symmetrical couplers, the intensity at the three photodetectors can be written as [12]

$$\begin{aligned} I_1 &= \frac{A}{3}\left[1+\cos(\Delta\phi+\frac{2\pi}{3})\right] \\ I_2 &= \frac{A}{3}\left[1+\cos(\Delta\phi)\right] \\ I_3 &= \frac{A}{3}\left[1+\cos(\Delta\phi-\frac{2\pi}{3})\right] \end{aligned} \tag{6.1}$$

where A is a constant and $\Delta\phi$ is the phase difference of the backscattered Rayleigh light between two separate sections of the sensing fibre, L metres apart. In addition, it is shown that the relationship between L and $\Delta\phi$ is (equation (3.6))

$$\Delta\phi = \frac{2\pi}{\lambda}\left(2\Delta L\right) \tag{6.2}$$

where ΔL represents the changes in L due to external perturbations ($L = L_0 + \Delta L$). In the previous chapters where the measurement procedure was based on coherent backscattered Rayleigh (which is an inelastic scattering process), strain fluctuations along the sensing fibre were changing $\Delta\phi$ through the variation of L. However, for an inelastic scattering process such as Brillouin scattering, strain fluctuations modify $\Delta\phi$ through

the variation of the wavelength of the Brillouin signal, λ_B. This capability of an IMZI has been employed in this chapter to directly measure the strain-induced frequency shift.

6.2.1 Characteristic of an IMZI as a Function of Wavelength

To determine the response of an IMZI with a path-imbalance of $\Delta\ell$ (figure 6.1 (a)) to an incident light as a function of its wavelength, $\Delta\phi$ in equation (6.1) should be replaced by the wavenumber of the light and the path-imbalance of the IMZI [13]

$$\begin{aligned} I_1 &= \frac{A}{3}[1+\cos(\Delta\ell\,\frac{2\pi}{\lambda}+\frac{2\pi}{3})] \\ I_2 &= \frac{A}{3}[1+\cos(\Delta\ell\,\frac{2\pi}{\lambda})] \\ I_3 &= \frac{A}{3}[1+\cos(\Delta\ell\,\frac{2\pi}{\lambda}-\frac{2\pi}{3})]. \end{aligned} \tag{6.3}$$

According to this equation, any changes in the wavelength of the input signal translates into optical intensity variation at the photodetectors. Consequently, if this IMZI receives the spontaneous Brillouin backscattered light from a sensing fibre, the strain-induced Brillouin frequency shift will result in an intensity variation of the light at the three output arms of the interferometer. Therefore, the Brillouin frequency shift can be directly measured by monitoring the intensity variation of the light at the output of the IMZI. The relationship between the FSR and the path-imbalance of an IMZI is

$$FSR = \Delta\nu = \frac{c_n}{\Delta\ell} \tag{6.4}$$

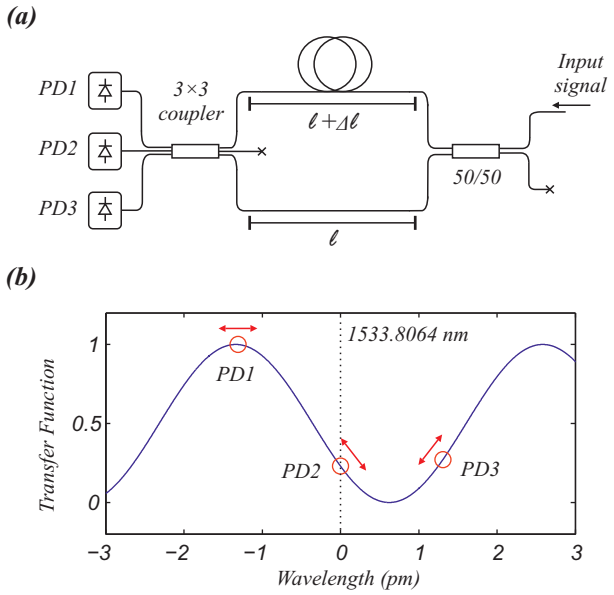

Figure 6.1: (a) Schematic of the MZI filter with a 3×3 coupler as the output coupler. The outputs of the photodetectors vary with varying incident wavelength. (b) Spectral response of MZI for $\Delta\ell = 60cm$ and $\lambda = 1533.8064nm$.

where c_n is the group velocity of the light in the fibre. Figure 6.1(b) shows the spectral response of this interferometer as a function of wavelength for λ between $1530.8nm$ and $1536.8nm$ and $\Delta\ell = 60cm$. The three circles on this figure represent the intensity of the light at the three photodetectors. Although the path-imbalance of the MZI results in the mixture of the backscattered light from two different regions of the fibre, it is later shown that the Brillouin backscattered light from two separate regions of the fibre are not coherent and, as a result, do not interfere. Chapter 3 has explained how the output of the three photodetectors can be combined using the differentiate and cross-multiply (DCM) demodulation technique to provide an output phase as a function of $\Delta\phi$,

$$\Phi = f(I_1, I_2, I_3) = \sqrt{3}\Delta\phi = \Delta\ell \frac{2\sqrt{3}\pi}{\lambda} = \frac{2\sqrt{3}\pi.\nu}{FSR}, \tag{6.5}$$

where ν is the frequency of the light. This equation shows that the demodulator transforms the cosine transfer function characteristic of the MZI to an output which is linearly proportional to the frequency of the light. In addition, according to equation 6.5, the DCM demodulator normalizes its output against the intensity of light at the input of the MZI. This implies that the sensor is immune to variations in the intensity of the backscattered light. This demodulation technique allows the sensor to measure larger strain-induced frequency shifts as the output of the MZI can travel over multiple fringes and is no longer restricted to the linear region of the MZI transfer function.

6.2.2 Effect of Path-Imbalance on BOTDR

In the previous chapters, the delay fibre was added to an IMZI to mix the Rayleigh backscattered light from two separate regions of the sensing fibre in order to extract the phase information. Although the purpose of the path-imbalance in the IMZI of the Brillouin-OTDR (BOTDR) setup is to convert Brillouin frequency shift into intensity variation, the presence of the path-imbalance still results in mixing of the backscattered Brillouin signals. In the case where the path-imbalance, $\Delta\ell$, is much shorter than the interrogating pulse width, L_{PW}, the mixing occurs between the backscattered light from two regions which have a large overlap (figure 6.2(a)) and therefore, the mixing has a negligible effect on the output.

For a longer $\Delta\ell$, however, the overlap of the two regions starts to reduce (figure 6.2(b)). Consequently, the noise level due to the mixing of the backscattered Brillouin light starts to increase. Nevertheless, since there are no correlation between the phase of the incident light and that of the Brillouin backscattered light, the phases of the Brillouin backscattered light from two separate regions of the fibre are not coherent. Therefore, with an assumption that the coherence length of the Brillouin backscattered light is longer than the path-imbalance of the MZI, only the Brillouin light backscattered from the common section of the two regions interfere. The relationship between the coherence

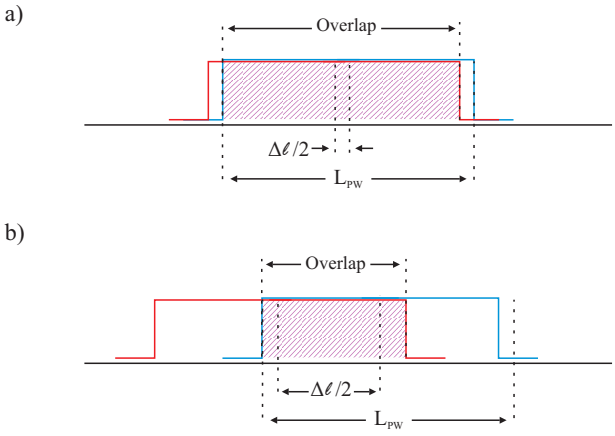

Figure 6.2: The effect of the path-imbalance and interrogating pulse width on the performance of the sensor.

length of light, l_c, and its bandwidth, $\Delta\nu$, is given by [14]

$$\Delta\nu = \frac{2c}{nl_c\pi}\sqrt{ln(2l_c\sqrt{\pi})}. \tag{6.6}$$

Using this equation, the value of the coherence length of Brillouin backscattered light with $30MHz$ bandwidth would be $7.72m$. It is clear that this technique does not work for $\Delta\ell > 2\,L_{PW}$ where there is no overlap between the two regions.

6.3 Experimental Arrangement

6.3.1 Experimental Setup

The experimental setup is shown in figure 6.3. A $1533.9nm$ distributed feedback (DFB) laser source was pulsed by directly modulating the injection current to generate $10ns$ pulses at a repetition rate of $5ms$. 90% of the output pulse was amplified by a $28dB$ gain Erbium-doped fibre amplifier (EDFA1) while the remaining 10% was used to trigger the oscilloscope. The amplified spontaneous emission (ASE) from the EDFA1 was filtered by a fibre Bragg grating (FBG) (reflectivity 99%; $\Delta\lambda = 3nm$; $\lambda = 1533.9nm$) and the filtered pulses ($\sim 4W$ peak power) were launched into the sensing fibre. The power was maximized to a level below the onset of any undesirable nonlinear effects such as self-phase modulation and modulation instability within $2km$ of the sensing fibre.

The sensing fibre comprised $2m$ of fibre subjected to strain by a stepper motor with $1.5km$ and $500m$ of unheated-unstrained fibre on either side of the $2m$ strained region. The backscattered light from the sensing fibre was redirected to another optical amplifier (EDFA2) with $25dB$ gain via circulator C2 for pre-amplification. A tunable fibre Bragg grating (TFBG) (reflectivity 70%; $\Delta\lambda = 3.5GHz$; $\lambda_{TFBG} = 1533.5 \sim 1534.5nm$) was tuned to reflect the Brillouin anti-Stokes at $\lambda = 1533.8064nm$. Anti-Stokes Brillouin backscattered light was used to avoid any undesirable stimulated Brillouin scattering

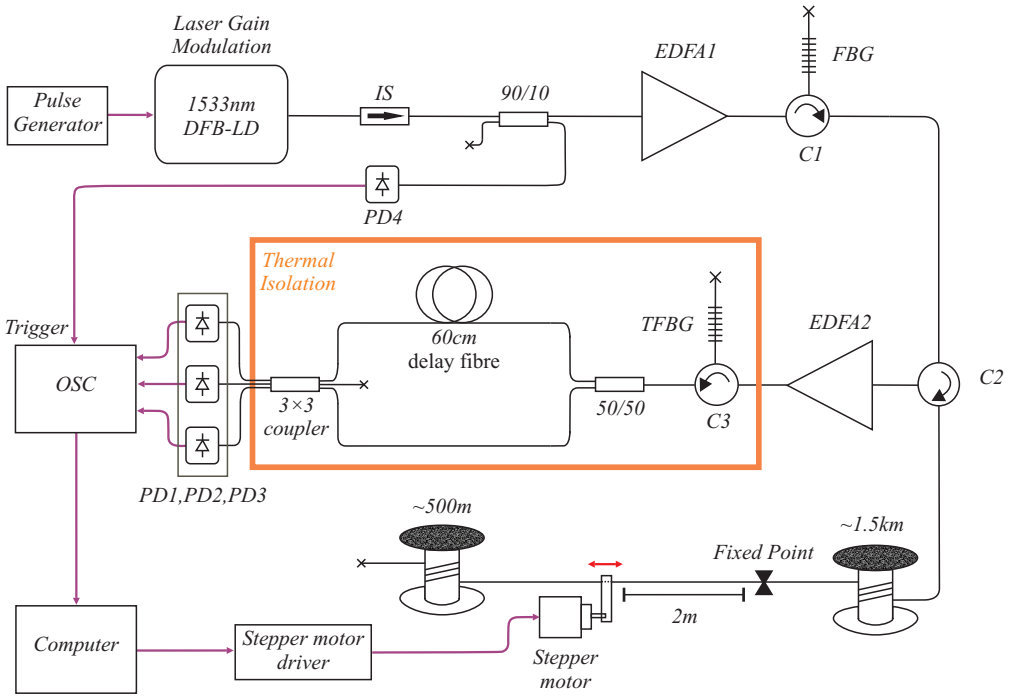

Figure 6.3: Experimental setup. DFB-LD: distributed feedback laser source, IS: isolator, EDFA: Erbium-doped fibre amplifier, PD: photodetector, FBG: fibre Bragg grating, TFBG: tunable fibre Bragg grating, C: circulator, OSC: oscilloscope.

(SBS). The anti-Stokes Brillouin light reflected from the TFBG was fed into the MZI filter with a path-imbalance of $60cm$ via a 50/50 coupler. The $60cm$ path-imbalance provided a filter with an FSR of $330MHz$ (equation (6.4)). A Brillouin frequency shift of $330MHz$ corresponds to $6.6m\varepsilon$ of strain, assuming a frequency variation of $1MHz$ per $20\mu\varepsilon$ [15].

The three arms of the 3×3 coupler at the output of the MZI filter were connected to three detectors (PD1, PD2, PD3) ($40V/mA$ transimpedance, $125MHz$ bandwidth, $22.5pW/\sqrt{Hz}$ NEP). The detector outputs were captured with a $250MHz$ oscilloscope at a $625MSa/sec$ sampling rate. The TFBG and the MZI filter were thermally isolated to prevent any undesirable changes in the path-imbalance of the interferometer ($\Delta\ell$) and λ_{TFBG}. The DCM demodulation was executed digitally. The steps of the signal-processing procedure including data rearrangement, DCM demodulation, and fast Fourier transform (FFT) are explained thoroughly in chapter 3.

6.3.2 Experimental Procedure

A stepper motor was used to apply strain with a triangular waveform to the fibre. Data were collected for various strains ($200\mu\varepsilon \sim 4m\varepsilon$) at different frequencies ($70mHz \sim 1Hz$). The oscilloscope sampling rate was set to $625MSa/sec$ which provided 12500 points for $2km$ of the sensing fibre *i.e.* one sample every $16cm$. The collected data were averaged at two stages. Initially, the data were averaged spatially by six points

to reduced the data points to 2100, *i.e.* approximately to one sample per metre. The second stage of averaging was carried out after the data acquisition and during the signal processing procedure. At this stage, the acquired traces were temporally averaged 100 times to further improve the SNR, an improvement which resulted in the reduction of the effective sampling rate from $200Sa/sec$ to $2Sa/sec$. Since each data point on the backscattered traces represents backscattered light from a specific section of the sensing fibre, averaging of a train of 100 traces is equivalent to time-averaging each section 100 times.

6.4 Results

Figure 6.4 depicts the FFT of the DCM demodulator output in a 3D diagram for a triangular strain of $1m\varepsilon$ with a repetition rate of $5sec$. The two axes at the bottom of the figure represent the distance along the fibre and the frequency of perturbation while the third axis shows the strain-induced frequency shift. The peak in this figure corresponds to the region where the stepper motor was located at a distance of $1520m$ from the front end of the sensing fibre.

Figure 6.5 shows the sensor's demodulator output as a function of time for $900\mu\varepsilon$ triangular strain with a repetition rate of $6\,sec$. The vertical axes of this diagram represent the applied strain on the sensing fibre for $30\,sec$ as a function of both frequency shift (axis on the left) and strain (axis on the right).

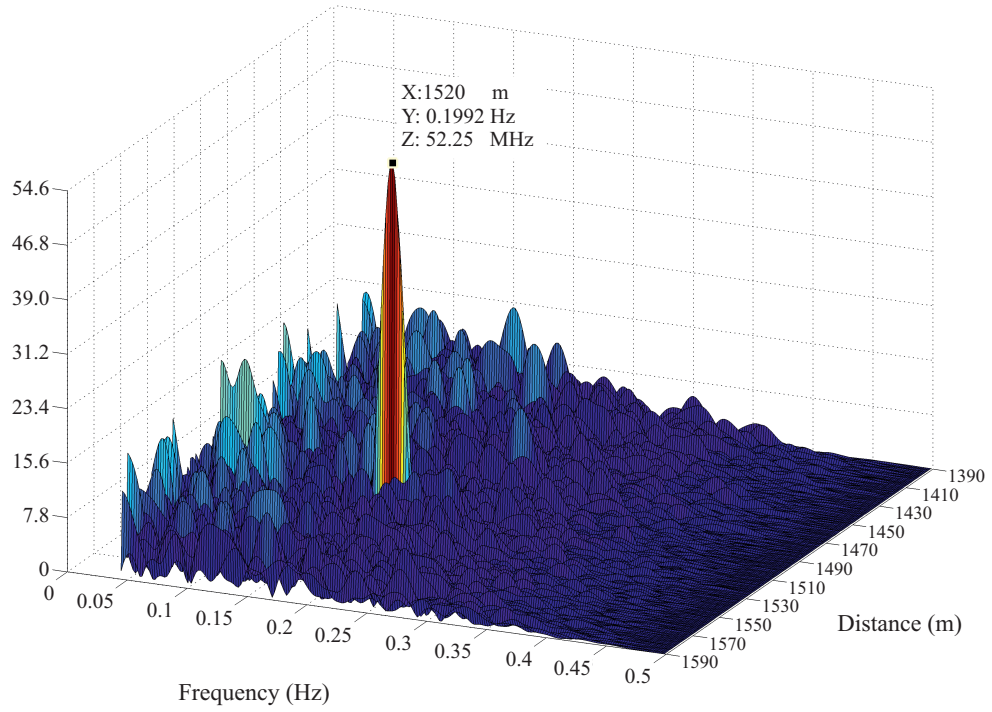

Figure 6.4: 3D plot of FFT of the DCM demodulator output for the $1390 \sim 1590m$ *section of the sensing fibre.*

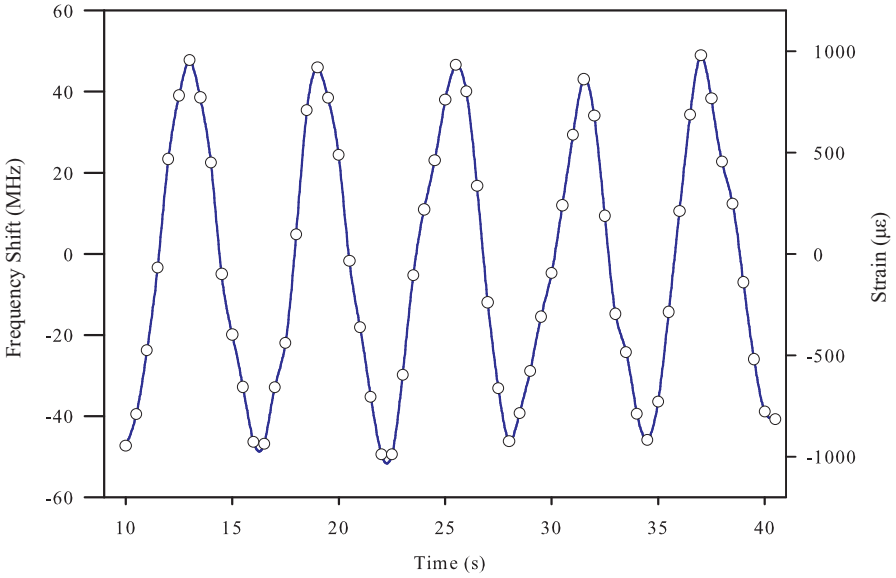

Figure 6.5: DCM demodulator output of the FUT at $1520m$.

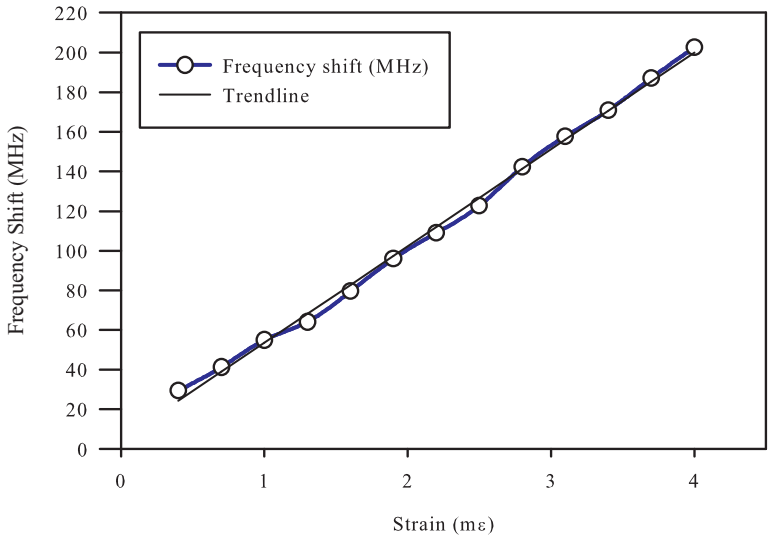

Figure 6.6: Applied strain to the fibre versus sensor output for $0.1Hz$ *triangular signal.*

The diagram of figure 6.6 depicts the peak value of the sensor's demodulator output as a function of the induced strain when the sensing fibre was subjected to various levels of strain at a frequency of $0.1Hz$ with a triangular wavelike pattern. A linear fit to the collected data yielded a correlation coefficient of $R^2 = 0.9966$.

6.5 Discussions

The peak in the 3D diagram of figure 6.4 accurately indicates the location, magnitude and frequency of the induced strain on the sensing fibre within the predicted accuracy of the sensor, *i.e.* $0.01Hz$ frequency resolution and $0.7m$ spatial resolution. This spatial

resolution was achieved by using interrogating pulses with $10ns$ pulse width. Unlike conventional BOTDR systems where the broadening of the Brillouin gain spectrum sets the lower limit of the spatial resolution[1], the minimum spatial resolution of the sensor proposed in this chapter depends on both the FSR of the MZI filter and the bandwidth of the Brillouin gain spectrum. The value of the FSR plays an important role in particular since it determines the spatial overlap between the backscattered light from two regions of the fibre (section 6.2.2) as well as the frequency response of the MZI filter. A smaller FSR increases the sensitivity of the sensor to frequency shift as demonstrated in figure 6.7(a) and 6.7(b).

In this figure, which shows the effect of the Brillouin frequency shift on the output of two MZI with FSR of $300MHz$ and $150MHz$, it can be seen that the intensity variation at the output of the MZI with a smaller FSR (longer path-imbalance) is much larger than that in the MZI with larger FSR. However, a longer path-imbalance reduces the overlap between the Brillouin backscattered light from two regions of the fibre which leads to a lower sensitivity, as explained earlier.

On the other hand, the spatial resolution of the sensor cannot be improved by reducing the width of the interrogating pulse since a narrower pulse with a broader linewidth covers a larger frequency range of the MZI filter. Comparing the frequency response of a MZI filter with an FSR of $150MHz$ with the linewidth of $10ns$ and $2ns$ pulses (figure 6.7(b) and 6.7(c) respectively) shows that while the linewidth of the $10ns$ pulse is confined within one fringe of the MZI characteristic, that of the $2ns$ pulse has spread over three fringes. As a result, the intensity variation is less significant in the case of the $2ns$ pulse since, for any given frequency shift, a portion of the backscattered light will always pass through the filter and reduce the visibility of the sensor.

In the proposed setup, the path-imbalance was adjusted to form a MZI filter with an FSR ten times larger than the linewidth of the Brillouin backscattered light. Therefore, for $10ns$ pulse width with $33MHz$ linewidth, the path-imbalance of the MZI was set to $60cm$ which is equivalent to FSR of $333MHz$ (equation (6.4)). In addition, it can be shown that, for a MZI with $60cm$ path-imbalance and $10ns$ pulse width, there would be 70% overlap between the backscattered signals which are mixed at the output coupler of the MZI filter.

Figure 6.5 shows the DCM demodulator output at the distance of $1520m$, matching the position of the stepper motor. The triangular wave with repetition rate of $6sec$ in this figure indicates that the output of the sensor accurately follows the applied strain to the sensing fibre. A strain accuracy of $\pm 50\mu\varepsilon$ was measured with signal-to-noise ratio of 1. The strain accuracy can be improved either by increasing the number of averages at the expense of the sampling rate or, alternatively, by narrowing the bandwidth of the MZI filter by increasing its path imbalance.

[1] Using a narrower pulse width in search of a higher spatial resolution results in a broader backscattered Brillouin spectrum which makes the detection of the peak value of the Brillouin spectrum more difficult.

The sensitivity of the demodulation to photodetector noise was assessed by simulating the backscattered Brillouin signal with detector noise. This revealed that photodetectors with a noise equivalent power (NEP) of $22.5pW/\sqrt{Hz}$ at the input of the DCM demodulator results in $35\mu\varepsilon$ strain noise. The detectors used had similar transimpedance gain. In principle, the overall sensitivity could be further improved by compensating for any variation in gain by detecting the fringe amplitude for each detector.

Figure 6.6 shows a linear relationship between the amplitude of the applied strain on the FUT and the sensor output for a triangular signal with $10sec$ repetition rate.

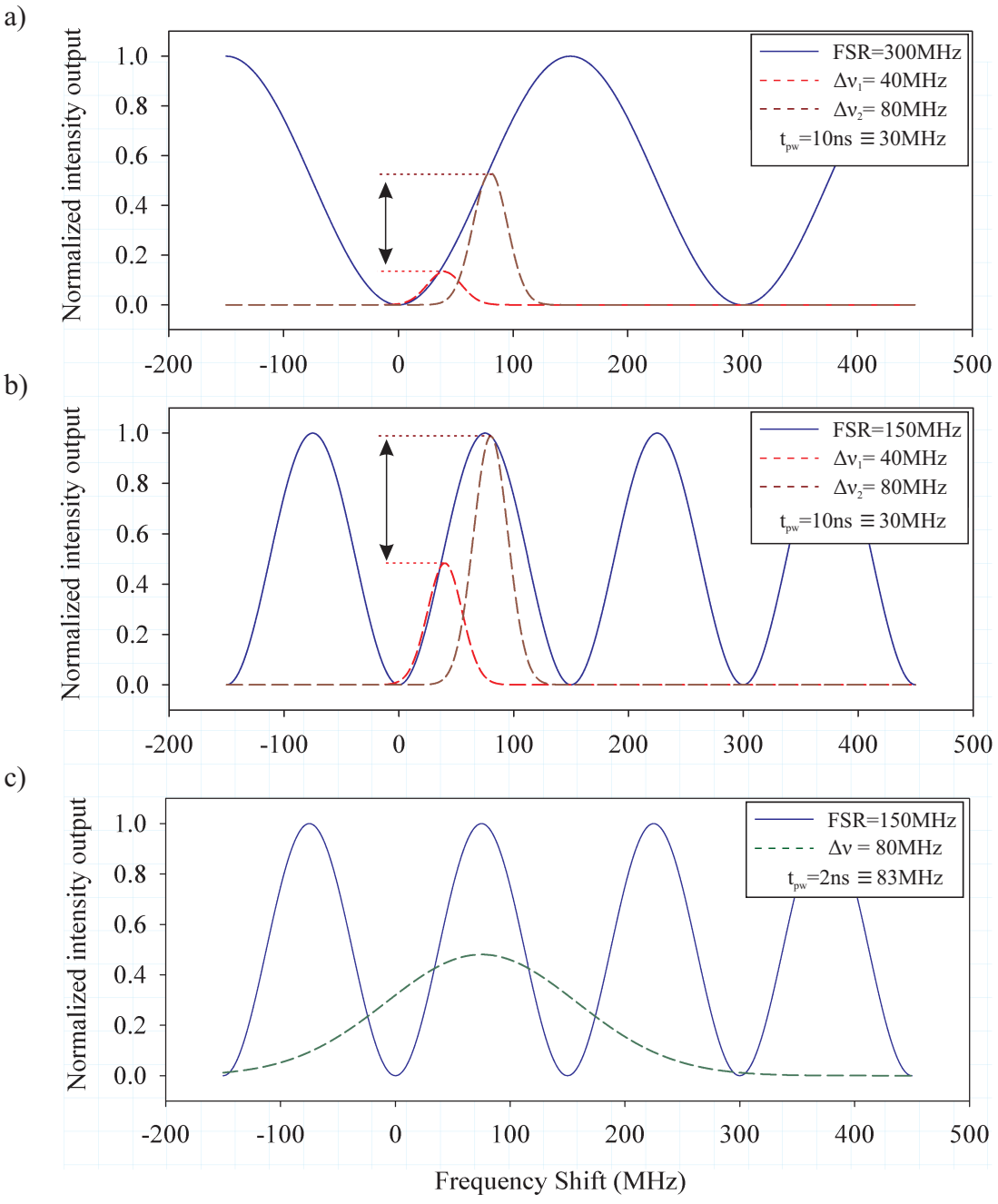

Figure 6.7: The effect of pulse width and FSR on the sensitivity of the sensor.

Similar experiments at other frequencies confirmed that the amplitude of the DCM demodulator is proportional to the strain amplitude and is independent of the applied frequency. The maximum measured strain was limited to $4m\varepsilon$ corresponding to the maximum displacement of the stepper motor. However, since the frequency shift is not limited to the linear region of the MZI filter transfer function, the maximum strain is only limited by the fibre's failure stress. For a standard single mode fibre (SSMF) the failure stress equals $100kpsi$ or $10m\varepsilon$.

The sampling rate of $200Sa/sec$ was limited by the data transfer rate of the oscilloscope. With a $2km$-long sensing fibre, the time-of-flight of an optical pulse is $20\mu s$. Therefore, with an oscilloscope capable of transferring data at a higher rate, the sampling rate of the proposed technique can be improved up to $50kSa/sec$ or $500Sa/sec$ effective sampling rate after 100 averages.

6.6 Conclusion

In this chapter, a Brillouin-based distributed strain sensor was demonstrated which directly measures the frequency shift of the Brillouin backscattered light by converting it to intensity variation at the photodetectors. An IMZI with an FSR of $300MHz$ was used to convert frequency shift to intensity variation. In addition, it was shown that incorporation of a 3×3 coupler at the output end of the IMZI combined with a DCM demodulator eliminates the fading problem associated with the MZI transfer function and enables the sensor to detect strains up to $10m\varepsilon$ at a sampling rate of $2Sa/sec$.

In addition, the relationship between the interrogating pulse width, path-imbalance of the MZI, and the spatial and strain resolution of the sensor was explained and it is shown that a setup with a path-imbalance of $60cm$ is capable of detecting dynamic strain with spatial resolution of $0.7m$ and strain accuracy of $\pm 50\mu\varepsilon$ using $10ns$ pulse width.

Bibliography

[1] L. Y. Song, Z. Y. He, and K. Hotate, "Distributed strain measurement with millimeter-order spatial resolution based on Brillouin optical correlation domain analysis," Optics Letters, vol. 31, pp. 2526-2528, 2006.

[2] M. Belal, Y. T. Cho, M. Ibsen, and T. P. Newson, "A temperature-compensated high spatial resolution distributed strain sensor," Measurement Science and Technology, vol. 21, 015204, 2010.

[3] M. Belal, and T. P. Newson, "A 5 cm spatial resolution temperature compensated distributed strain sensor evaluated using a temperature controlled strain rig," Optics Letters, vol. 36, pp. 4728-4730, 2011.

[4] M. N. Alahbabi, Y. T. Cho, and T. P. Newson, "150-km-range distributed temperature sensor based on coherent detection of spontaneous Brillouin backscatter and in-line Raman amplification," Journal of Optical Society of America B, vol. 22, pp. 1321-1324, 2005.

[5] M. N. Alahbabi, Y. T. Cho, and T. P. Newson, "100 km distributed temperature sensor based on coherent detection of spontaneous Brillouin backscatter," Measurement Science and Technology, vol. 15, pp. 1544-1547, 2004.

[6] S. M. Maughan, H. H. Kee, and T. P. Newson, "57-km single-ended spontaneous Brillouin-based distributed fiber temperature sensor using microwave coherent detection," Optics Letters, vol. 26, pp. 331-333, 2001.

[7] K. Hotate and S. S. L. Ong, "Distributed dynamic strain measurement using a correlation-based Brillouin sensing system," IEEE Photonics Technology Letters, vol. 15, pp. 272-274, 2003.

[8] K. Y. Song, M. Kishi, Z. Y. He, and K. Hotate, "High-repetition-rate distributed Brillouin sensor based on optical correlation-domain analysis with differential frequency modulation," Optics Letters, vol. 36, pp. 2062-2064, 2011.

[9] R. Bernini, A. Minardo, and L. Zeni, "Dynamic strain measurement in optical fibers by stimulated Brillouin scattering," Optics Letters, vol. 34, pp. 2613-2615, 2009.

[10] Y. Peled, A. Motil, I. Kressel, and M. Tur, "Monitoring the propagation of mechanical waves using an optical fiber distributed and dynamic strain sensor based on BOTDA," Optics Express, vol. 21, pp. 10697-10705, 2013.

[11] H. H. Kee, G. P. Lees, and T. P. Newson, "All-fiber system for simultaneous interrogation of distributed strain and temperature sensing by spontaneous Brillouin scattering," Optics Letters, vol. 25, pp. 695-697, 2000.

[12] R. G. Priest, "Analysis of Fiber Interferometer Utilizing 3x3 Fiber Coupler," IEEE Journal of Quantum Electeronics, vol. 18, pp. 1601-1603, 1982.

[13] K. De Souza, P. C. Wait, T. P. Newson "Double-pass configured fibre Mach-Zehnder interferometric optical filter for distributed fibre sensing," IEEE Electronics Letters, vol.33, pp.2148 - 2149, 1997.

[14] P.C. Wait, T.P. Newson, "Measurement of Brillouin scattering coherence length as a function of pump power to determine Brillouin linewidth," Optics Communications, vol. 117, pp. 142–146, 1995.

[15] M. Belal and T. P. Newson, "Experimental Examination of the Variation of the Spontaneous Brillouin Power and Frequency Coefficients Under the Combined Influence of Temperature and Strain," Journal of Lightwave Technology, vol. 30, pp. 1250-1255, 2012.

Chapter 7

Conclusion

7.1 Summary

For more than two decades, the focus of the research on distributed optical fibre sensors was primarily to develop distributed sensors capable of measuring slow-varying phenomena such as temperature and static strain. However, the advancements in a number of key areas such as high-speed digital signal processing and high throughput data acquisition technology have led to an ever-increasing research activity in DOFS capable of detecting and measuring dynamic phenomena such as acoustic vibrations.

One such sensor capable of measuring the frequency and amplitude of multiple dynamic strains along the sensing fibre has been studied in this thesis. The strain measurement along the given section of the sensing fibre was realized using the phase difference between the Rayleigh backscattered light from the two ends of that section. To measure the phase difference between the backscattered light from the two ends, an imbalanced Mach-Zehnder interferometer (IMZI) was used. It has been shown that by using a 3×3 coupler at the output end of the IMZI and analyzing the output of the interferometer using a digitally implemented differentiate and cross-multiply demodulator (DCM), a linear relationship between the strain-induced phase-shift and the sensor output can be achieved. In addition, it has been shown that the signal fading problem in the interferometer can also be eliminated using a symmetrical 3×3 coupler.

The response of the sensor to dynamically-induced longitudinal strain on the sensing fibre has been evaluated. It has been shown that the sensor can detect longitudinal strains as low as $80n\varepsilon$ with an accuracy of $30n\varepsilon$ over a frequency and sensing range of $4000Hz$ and $1km$, respectively. The minimum detectable frequency of the sensor was limited to $500Hz$ due to the limitation in the data collection time.

The response of the sensor to transverse strain was also analyzed both theoretically and experimentally. It was shown that the sensitivity of the sensor to acoustically-induced transverse strains in the fibre is a function of the gauge length of the sensor and the frequency of the acoustic wave. The sensitivity of the fibre to acoustic wave was assessed by exciting the sensing fibre using a loud speaker. To improve the sensitivity

of the sensor to acoustic perturbations, the effective surface area of the sensing fibre was increased by attaching the fibre to a polystyrene sheet. The frequency and sound-pressure level range of the sensor was measured to be between $90dBC \sim 120dBC$ and $100Hz \sim 4000Hz$, respectively. It was shown that the SPL range of the sensor can be modified by changing the coating diameter of the sensing fibre. In addition, a comparison between the output of the sensor and the output voltage of a microphone showed that the sensing fibre can be used as a distributed acoustic transducer.

It has been explained how the distributed dynamic strain sensor can be used to measure other dynamic phenomena such as magnetically-induced strains in a Nickel wire. By coupling a Nickel wire and an optical fibre, a distributed magnetic field sensor has been formed that was capable of mapping the transverse component of the applied magnetic field on the Nickel wire over a $1km$ sensing range. The sensor demonstrated a magnetic field intensity range of $1Gs \sim 8Gs$ over a frequency range of $50Hz \sim 5000Hz$. The accuracy of the sensor was measured to be $0.3Gs$.

Furthermore, considering the transmission curve of an IMZI as a function of the frequency (or wavelength) of the incident light, a Brillouin-based distributed strain sensor has been demonstrated. In this experiment, an IMZI has been used to convert the Brillouin frequency shift to optical intensity variations, hence forming a strain-to-intensity transducer. The sensor has demonstrated a strain range of $0.5m\varepsilon$ to $4m\varepsilon$ with an accuracy of $\pm 50\mu\varepsilon$ and spatial resolution of $70cm$.

Finally, a comparison between the main parameters of the distributed dynamic strain sensor studied in this thesis and two other distributed vibration sensing techniques introduced in the second chapter (*i.e.* distributed strain sensing based on the Brillouin correlation domain technique and distributed vibration technique based on CRN) is presented in table 7.1.

7.2 Future Work

Using optical fibres for distributed measurement of a dynamic phenomenon is relatively new in comparison with more established distributed sensors such as distributed temperature sensors. Therefore, there is still a great deal of scope for research in this area since most of the studies are still in their early stages. The following outlines the key aspect of distributed dynamic strain sensing which can be further explored.

Limitation of the Sensing Technique

The focus of this research was to establish a distributed sensor capable of measuring dynamic phenomena using φ-OTDR. The minimum detectable strain of the preliminary experimental setup was measured to be $100n\varepsilon$ which is equivalent to $\sim 0.4\,rad$. Since Mach-Zehnder interferometers are sensitive enough to measure phase-shifts as low as few micro-radians, it is of significant importance to determine the factors which limit

	$\varphi - OTDR$	CRN	$BOCDR$ & $BOCDA$
Spatial Resolution	$1m$	$1m$	$10cm$
Sensing Range	$1km$	$50km$	$20m$
Frequency Range	$5kHz$	$1kHz$	$200Hz$
Strain Range	$100n\varepsilon \sim 1.6\mu\varepsilon$	N/A	$200\mu\varepsilon \sim 900\mu\varepsilon$
Strain Resolution	$20n\varepsilon$	N/A	$140\mu\varepsilon$
Complexity of the Setup	*Moderate*	*Simple*	*Complex*

Table 7.1: Comparison between the three optical fibre-based distributed vibration sensing techniques discussed in this thesis.

the strain range of the distributed sensor to $0.4\,rad$. Both simulation and experiment can be used to evaluate the sensitivity of the sensor to parameters such as linewidth of the light source, pulse width, and polarization of the light.

Sensing Range

The relatively short sensing range of the sensor was another limiting factor of the distributed dynamic strain sensor studied in this thesis. As discussed in chapter 3, the frequency and strain range of the φ-OTDR-based distributed sensors are inversely proportional to the sensing range of the sensor (equation 3.17). However, both the sensing and strain ranges of the sensor can be improved by wavelength division multiplexing (WDM) technique in which multiple interleaved probe pulses with different wavelengths are used to monitor changes along the sensing fibre. In this technique, the sensing range (or the strain range) of the sensor can be increased by a factor of n where n is the number of pulses with different wavelengths.

Strain Resolution

The strain resolution of the φ-OTDR-based distributed dynamic strain sensors can be improved using two sets of approaches. The first approach which has been mentioned

earlier is based on refining the parameters of the sensor such as the linewidth of the probe pulse to reduce the noise level and improve the SNR. The second approach, on the other hand, relies on modifying the mechanical properties of the elements which form the sensor. For instance, the strain sensitivity of a fibre can be increased by using low Young's modulus compounds in the cladding and protective coating of the fibre. Therefore, a micro-structured hollow core fibre is an ideal replacement for standard single mode fibre (SSMF) since the layout of such fibre allows most of the strain on the surface of the fibre to be transferred to the core. A light source with a shorter wavelength can also be used to improve the strain resolution of the sensor. For instance, changing the wavelength of the light source from $1500nm$ to $750nm$ not only improves the intensity of the backscattered Rayleigh by a factor of sixteen ($I_{BS} \propto 1/\lambda^4$), but also enhances the strain sensitivity of the sensor since the phase angle of the MZI is inversely proportional to the wavelength of the backscattered light.

Signal Processing Procedure

The performance of the φ-OTDR-based distributed dynamic strain sensor relies on both the experimental setup as well as the signal processing procedure. A more advanced signal processing procedure can be used to improve the performance of the sensor. Improvement in data processing can be realized by optimizing the window function before the FFT process, using the infinite-duration impulse response (IIR) filter, and using cross-correlation between adjacent data along the trace to improve the SNR. In addition, the signal processing procedure presented in Appendix C can also be improved by using an interpolation technique to measure the slope of the signal at each point.

Real-Time Data Acquisition and Signal Processing

In the fourth chapter, it has been shown that the lower frequency range of the sensor is limited to $100Hz$. This was because the data acquisition time was restricted to less than $200ms$ on account of the buffer size of the digitizer. Therefore, by developing a hybrid Optical-Electronics system capable of transferring traces directly to an external storage in real time, the frequency range of the sensor can be expanded to sub-hertz regime while the SNR can be improved at the same time. In addition, by adding an embedded system to the output of the experimental setup, a real-time data processing capability can be added to the sensor. The embedded system can be developed to, for instance, analyze and discard unimportant data while displaying the perturbations along the fibre in real time.

New Class of Distributed Sensors

By combining two or more distributed dynamic strain sensors, a new class of distributed sensors with diverse sensing capabilities can be formed. The following are two examples of such sensors.

Distributed 2D Positioning Sensors: In chapter 4, it has been shown that a DAS can be used to measure the frequency, amplitude, and location of the acoustic perturbations along the sensing fibre. However, using a single sensing fibre, it is difficult to measure the distance of the acoustic source from the sensing fibre, *i.e.* to determine whether the acoustic perturbation is due to a small sound source close to the fibre or a loud sound source further away from the fibre. However, by laying two sets of sensing fibres in parallel with each other, but at some distance apart, and by monitoring and comparing the output of the two sensors simultaneously, measuring the size and distance of the acoustic source from the sensing fibre can be facilitated.

3D Shape Sensing: The sensing procedure explained in the previous paragraph can be expanded to monitor the shape of a 3D structure. By installing four parallel sets of distributed dynamic strain sensors on a structure and by collecting and analyzing the combined data, it is possible to measure the deformation of a 3D structure. Such measurement is very important in geophysical sciences where the changes in the shape of the Earth's crust due to geophysical activities of the Earth such as earthquakes and land slides can provide a better understanding of the activities inside the Earth.

Application of the Distributed Dynamic Strain Sensor in Measuring Other Physical Phenomena

The distributed dynamic strain sensor can be used to indirectly measure a range of other physical phenomena which induce strain in the fibre. An example of such a sensor has been demonstrated in chapter 5 where the distributed magnetic field was measured by coupling the sensing fibre to a Nickel wire. This category of sensors can be considered as a subset of the distributed dynamic strain sensor since they rely on a transducer (magnetic field to mechanical strain in case of the distributed magnetic field sensor) to convert a certain physical phenomenon to mechanical strain. In the case of the distributed magnetic field sensor, for instance, the role of the Nickel wire was to convert the magnetic field to mechanical strain. The same principle can be employed to develop a number of different distributed sensors. For instance, by coating the sensing fibre with an electroactive polymer, a distributed electric field sensor can be developed.

Appendices

A The Derivation of the Rayleigh Scattering Coefficient

The thermal motion of molecules during the cooling phase of the fibre fabrication process results in fluctuations in the density of the molecules in the fibre, which in turn produces fluctuations in its permitivity [1]. The permitivity of the fibre can be written as

$$\varepsilon = \varepsilon_m + \varepsilon_m \Delta\varepsilon \tag{A.1}$$

where ε_m is the average permitivity of the medium and $\Delta\varepsilon$ is the deviation of the permitivity from its average value. The first term in equation (A.1) does not contribute to the scattering of light since, in a completely homogeneous medium, the radiation from homogeneously distributed dipoles cancels out in all but the forward direction. Therefore, from a total dipole moment $\mathbf{P}$ ($= \mathbf{P}_m + \Delta\mathbf{P}$), only the secondary wave generated due to fluctuations in dipole moment, $\Delta\mathbf{P}$, contributes to the scattering of the light. The relationship between the dipole moment due to fluctuations in the density of the medium, $\Delta\mathbf{P}$, and the incident electric field is given by

$$\Delta\mathbf{P} = \varepsilon_m \Delta\varepsilon \mathbf{E}. \tag{A.2}$$

To analyze the effect of the fluctuations in the medium permitivity on the total electric field inside the fibre, E_T, the total electric field needs to be represented in the form of the sum of the incident field, $\mathbf{E}$, and the scattered field, $\mathbf{E}'$

$$\mathbf{E}_T = \mathbf{E} + \mathbf{E}'. \tag{A.3}$$

The electric displacement due to the secondary waves can be written as

$$\mathbf{D}' = \varepsilon_m \mathbf{E}' + \Delta\mathbf{P} = \varepsilon_m \mathbf{E}' + \varepsilon_m \Delta\varepsilon \mathbf{E}. \tag{A.4}$$

Note that the $\mathbf{P}_m$ term is not included since it does not contribute to the scattered waves. For numerical analysis of the scattered light within a continuous medium, the

macroscopic form of Maxwell's equations for the secondary waves are used:

$$\begin{cases} \nabla \times \mathbf{E}' = -\frac{\partial \mathbf{B}'}{\partial t} \ , \\ \nabla \,.\, \mathbf{D}' = 0 \ , & (\rho = 0) \\ \nabla \times \mathbf{H}' = \frac{\partial \mathbf{D}'}{\partial t}. & (\mathbf{J} = 0) \end{cases} \tag{A.5}$$

Eliminating $\mathbf{H}'$ from the set of equations (A.5) yields

$$\nabla \times (\nabla \times \mathbf{E}') = -\mu_m \frac{\partial^2 \mathbf{D}'}{\partial t^2} \tag{A.6}$$

where μ_m is the permeability of the medium. Replacing $\mathbf{E}'$ from equation (A.4) in equation (A.6) yields

$$\nabla^2 \mathbf{D}' - \frac{n^2}{c^2} \frac{\partial^2 \mathbf{D}'}{\partial t^2} = \nabla \times (\nabla \times \varepsilon_m \Delta\varepsilon \mathbf{E}) \tag{A.7}$$

where n is the refractive index of the medium and c is the speed of light. The solution of the differential equation (A.7) is given by [2]

$$\mathbf{D}' = \nabla \times (\nabla \times \mathbf{\Pi}) \tag{A.8}$$

where Π is the Hertzian vector which, at large distances for scattering volume V, can be described as

$$\mathbf{\Pi} = \frac{1}{4\pi L} \int_V \varepsilon_m \Delta\varepsilon \mathbf{E} \exp[ik'(L - r)] \, dV. \tag{A.9}$$

Here, k' is the wave vector of the scattered light, $\mathbf{L}$ is the distance vector from volume V to the point of observation, and $\mathbf{r}$ is the radius vector from volume V to any elements within the scattering medium. Substituting the incident light wave $E = E_0 \exp(ikr)$ in equation (A.9) gives

$$\mathbf{\Pi} = \frac{\varepsilon_m E_0 \exp[ik'L]}{4\pi L} \int_V \Delta\varepsilon \exp[i(k - k')\, r] \, dV. \tag{A.10}$$

permitivity fluctuations, $\Delta\varepsilon$, can be written in terms of the fluctuations in the temperature and density of the medium

$$\Delta\varepsilon = \left(\frac{\partial \varepsilon}{\partial \rho}\right)_T \Delta\rho + \left(\frac{\partial \varepsilon}{\partial T}\right)_\rho \Delta T. \tag{A.11}$$

Replacing equation (A.11) in (A.10) gives

$$\mathbf{\Pi} = \frac{\varepsilon_m E_0 \exp(ik'L)}{4\pi L} \left(\frac{\partial \varepsilon}{\partial \rho}\right)_T \int_V \Delta\rho \exp[i(k - k')] \, dV \tag{A.12}$$

where the second term on the right side of equation (A.11) is neglected. The density deviation can be represented in the form of a three dimensional Fourier series

$$\Delta\rho = \sum_{q} \Delta\rho_q \, \exp(iqr) \tag{A.13}$$

where $\Delta\rho_q$ is given by [3]

$$\Delta\rho_q = \frac{1}{V} \int \Delta\rho \exp(-iqr)\, dV. \tag{A.14}$$

Here, q is the expansion parameter. Substituting equation (A.13) in (A.12) gives

$$\mathbf{\Pi} = \frac{\varepsilon_m E_0 \exp(ik'L)}{4\pi L} \left(\frac{\partial\varepsilon}{\partial\rho}\right)_T \int_V \sum_q \Delta\rho_q \, \exp[i(k+q-k')]\, dV. \tag{A.15}$$

For large volumes of V, the value of the integral in equation (A.15) differs from zero only when [3]

$$k + q - k' = 0.$$

Therefore, by satisfying this condition, equation (A.15) transforms into

$$\mathbf{\Pi} = \frac{\varepsilon_m E_0 \, V \, \exp(ik'L)}{4\pi L} \left(\frac{\partial\varepsilon}{\partial\rho}\right)_T \Delta\rho_q. \tag{A.16}$$

The electric field of the scattered light can be obtained by substituting equation (A.16) in (A.8)

$$\mathbf{E}' = \frac{(k')^2 \, E_0 \, V \, \exp(ik'L)}{4\pi L} \left(\frac{\partial\varepsilon}{\partial\rho}\right)_T \Delta\rho_q \, \sin\theta \tag{A.17}$$

where θ is the angle between the incident and the scattered light. For an incident light propagating in $\bar{x}$ direction with two orthogonal polarization in $\bar{y}$ and $\bar{z}$ directions, using equation (A.17), the intensity of the scattered light can be written as follows:

$$I = I_0 \frac{(k')^4 \, V^2 \, \overline{\Delta\rho_q^2} \left(\frac{\partial\varepsilon}{\partial\rho}\right)_T^2}{2\,(4\pi L)^2} \left(\sin^2(\theta_y) + \sin^2(\theta_z)\right) \tag{A.18}$$

where

$$I_0 = {E_{0y}}^2 + E_{0z}^2.$$

In addition, since the following equation is valid for any arbitrary direction in the Cartesian coordination

$$\sin^2(\theta_x) + \sin^2(\theta_y) + \sin^2(\theta_z) = 1, \tag{A.19}$$

substituting this in (A.18) gives

$$I_\theta = I_0 \frac{(k')^4\, V^2\, \overline{\Delta\rho_q^2}\, \left(\frac{\partial\varepsilon}{\partial\rho}\right)_T^2}{2\,(4\pi L)^2}\, cos^2(\theta_x) \tag{A.20}$$

where θ_x is the angle between the direction of the incident light and the direction of observation. The mean-square density fluctuation, $\overline{\Delta\rho_q^2}$, is given by [4]

$$\overline{\Delta\rho_q^2} = \frac{\rho_0^2}{V}\left\{K\,T_f\,(\beta_T - \beta_S) + K\,T_f\,[\beta_S - (\rho_0\,v^2)^{-1}] + K\,T\,[(\rho_0\,v^2)^{-1}]\right\} \tag{A.21}$$

where T_f is the fictive temperature, β_S and β_T are the equilibrium isothermal and adiabatic compressibilities, respectively, K is the Boltzmann's constant, ρ_0 is the mean density of the medium, T is the absolute temperature, and v is the sound velocity in the glass. The first two terms in this equation represent intensity that appears in the Rayleigh line of the spectrum while the last term represents the Brillouin scattering. Therefore, substituting the first two terms of equation (A.21) in (A.20) gives the intensity of the Rayleigh scattering due to density fluctuations, $I_{\theta(\rho)}$:

$$I_{\theta(\rho)} = I_0 \frac{(k')^4\, V}{2\,(4\pi L)^2}\, K\,T_f\,[\beta_T - (\rho_0\,v^2)^{-1}]\,\left(\rho\,\frac{\partial\varepsilon}{\partial\rho}\right)_T^2 cos^2(\theta_x). \tag{A.22}$$

However, since $(\rho_0\,\nu^2)^{-1} \ll \beta_T$ and $k' = \frac{2\pi}{\lambda}$, equation (A.22) becomes

$$I_{\theta(\rho)} = I_0 \frac{\pi^2\, V}{2\,L^2\,\lambda^4}\, K\,T_f\,\beta_T\,\left(\rho\,\frac{\partial\varepsilon}{\partial\rho}\right)_T^2 cos^2(\theta_x). \tag{A.23}$$

Also, for an isotropic solid, the derivative of the permitivity with respect to the density of the medium can be expressed as a function of the average photoelastic coefficient, p, and the refractive index of it [5]

$$\left(\rho\,\frac{\partial\varepsilon}{\partial\rho}\right)_T = n^4 p. \tag{A.24}$$

Substituting (A.24) in (A.23) gives

$$I_{\theta(\rho)} = I_0 \frac{\pi^2\, V}{2\,L^2\,\lambda^4}\, K\,T_f\,\beta_T\,n^8 p^2\, cos^2(\theta_x). \tag{A.25}$$

The total scattered light due to volume V is given by

$$I = \int_0^{2\pi}\int_0^{\pi} I_{\theta(\rho)}\,\sin(\theta_x)\,d\theta_x d\varphi = I_0 \frac{8\pi^3\, V}{3\,L^2\,\lambda^4}\, K\,T_f\,\beta_T\,n^8 p^2. \tag{A.26}$$

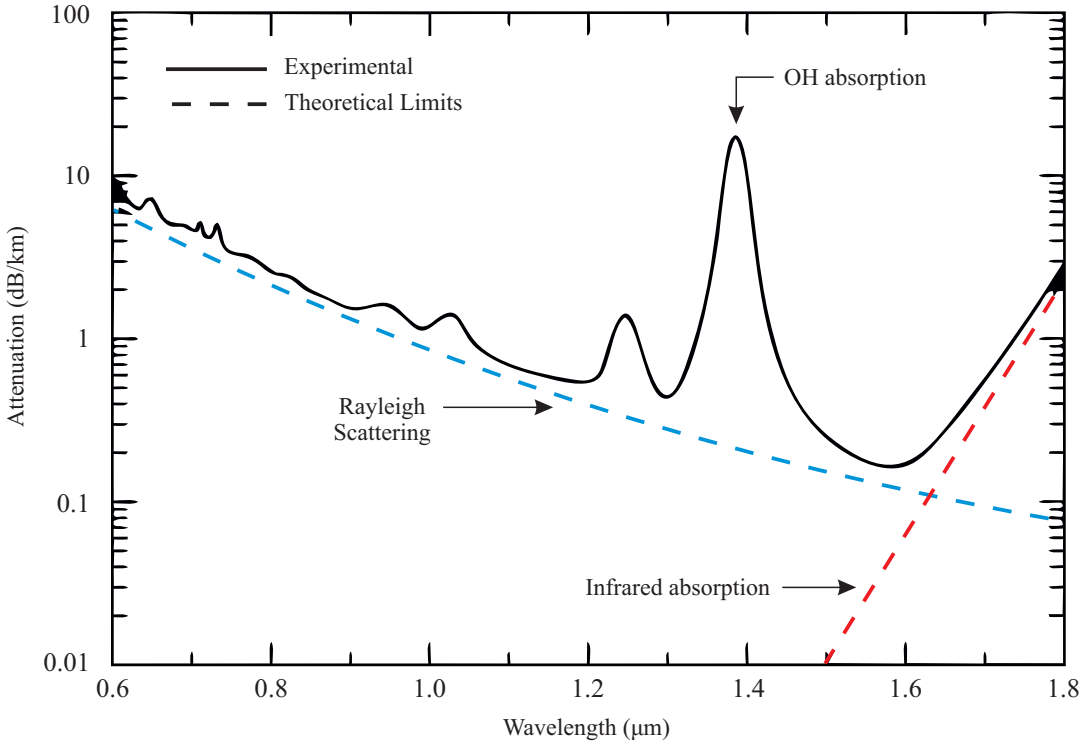

Figure A.1: Standard single mode fibre attenuation as a function of wavelength, adopted from [6].

The Rayleigh scattering coefficient, γ_R, is defined as the intensity of the scattered light per unit incident light intensity per unit length

$$\gamma_R = \frac{I}{I_0}\frac{L^2}{V}. \tag{A.27}$$

As a result, the Rayleigh scattering coefficient can be obtained by combining equations (A.26) and (A.27)

$$\gamma_R = \frac{8\pi^3}{3\,\lambda^4} K\, T_f\, \beta_T\, n^8 p^2. \tag{A.28}$$

Figure A.1 shows the diagram of silica fibre attenuation as a function of wavelength (the solid line). The dashed blue-line in this figure exhibits the theoretical limitation of attenuation set by Rayleigh scattering (equation (A.28)). This demonstrates that the fibre attenuation cannot be improved any further regardless of the level of control over the production process of the fibre.

Bibliography

[1] K. Yoshida, Y. Furui, S. Sentsui, and T. Kuroha, "Loss factors in optical fibres," Optical and Quantum Electronics, vol. 13, pp. 85-89, 1981.

[2] J. A. Startton, "Electromagnetic theory," McGraw-Hill, New York, 1941.

[3] I. L. Fabelinskii, "Molecular scattering of light," Plenum Press, New York, 1986.

[4] N. L. Laberge, V. V. Vasilescu, C. J. Montrose, and P. B. Macedo, "Equilibrium compressibilities and density fluctuations in $K_2O - SiO_2$ glasses," 74th Annual Meeting, The American Ceramic Society, Washington DC, May 10, 1972.

[5] J. F. Nye, "Physical properties of crystals," Clarendon Press, Oxford, 1960.

[6] J. M. Senior, "Optical fibre communications: Principles and practice," 3rd edition, Pearson Education, Essex, 2009.

B Mathematical Analysis of Differentiate and Cross-Multiply Demodulator

This appendix provides the mathematical analysis of the differentiate and cross-multiply demodulator. The block diagram of this demodulator is reproduced here for convenience (figure B.1). It will be shown that for an input signal in the form of

$$\begin{aligned} I_1 &= I_0[M + N\cos(\Delta\phi)] \\ I_2 &= I_0[M + N\cos(\Delta\phi + \frac{2\pi}{3})] \\ I_3 &= I_0[M + N\cos(\Delta\phi - \frac{2\pi}{3})], \end{aligned} \tag{B.1}$$

the output of the demodulator is a linear function of the input phase-difference, $\Delta\phi$.

The demodulation process starts with the elimination of the DC components from the input signals. Adding the three outputs gives

$$3S = I_1 + I_2 + I_3 = 3M \tag{B.2}$$

since $cos(\varphi) + cos(\varphi + 120°) + cos(\varphi - 120°) = 0$. Subtracting the sum S from the three interferometric outputs gives

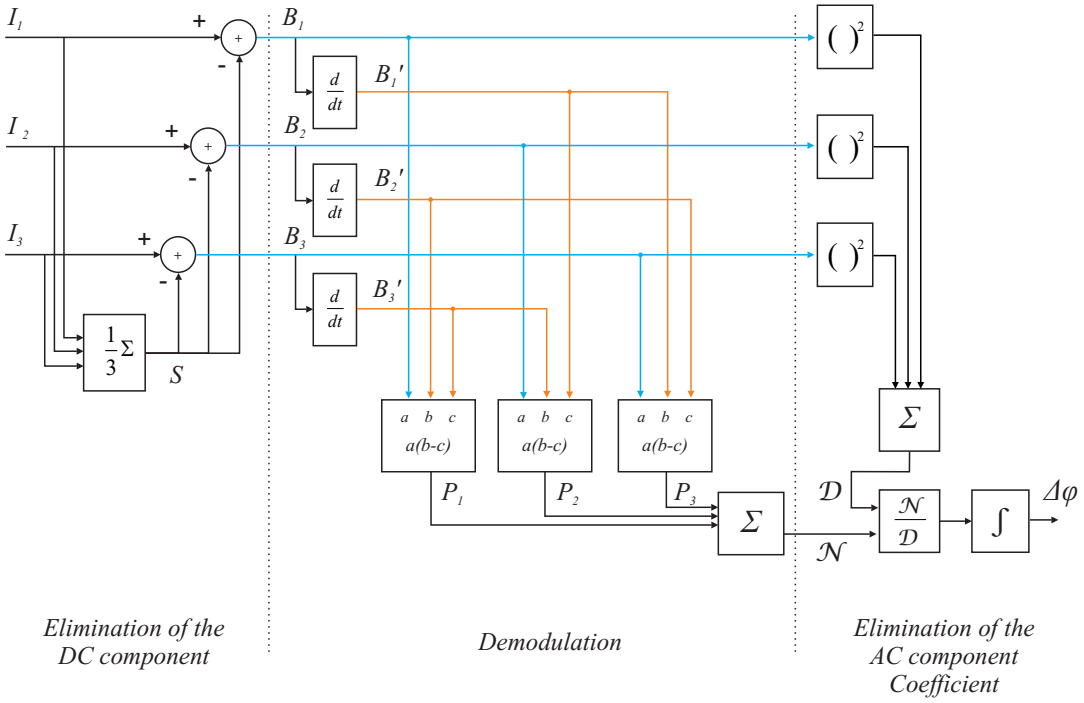

Figure B.1: Block diagram of the differentiate and cross-multiply demodulator.

$$\begin{aligned} B_1 &= I_0 N \cos(\Delta\phi) \\ B_2 &= I_0 N \cos(\Delta\phi + \frac{2\pi}{3}) \\ B_3 &= I_0 N \cos(\Delta\phi - \frac{2\pi}{3}). \end{aligned} \tag{B.3}$$

The second stage of the demodulation process involves taking the difference between the derivatives of each of two signals and multiplying it by the third signal to extract the phase information. For instance, combining signal B_1 with the derivatives of B_2 and B_3 yields

$$P_1 = B_1(\dot{B_2} - \dot{B_3}) = I_0^2 N^2 \,\dot{\Delta\phi} \cos(\Delta\phi)[-sin(\Delta\phi + \frac{2\pi}{3}) + sin(\Delta\phi - \frac{2\pi}{3})]. \tag{B.4}$$

Applying the trigonometric identity

$$sin(A+B) - sin(A-B) = 2\,cos(A)\,sin(B)$$

to equation (B.4) gives

$$P_1 = \sqrt{3}\, I_0^2 N^2 \,\dot{\Delta\phi} cos^2(\Delta\phi). \tag{B.5}$$

Using the same process for two other combinations results in

$$\begin{aligned} P_1 &= \sqrt{3}\, I_0^2 N^2 \,\dot{\Delta\phi} cos^2(\Delta\phi) \\ P_2 &= \sqrt{3}\, I_0^2 N^2 \,\dot{\Delta\phi} cos^2(\Delta\phi - \frac{2\pi}{3}) \\ P_3 &= \sqrt{3}\, I_0^2 N^2 \,\dot{\Delta\phi} cos^2(\Delta\phi + \frac{2\pi}{3}). \end{aligned} \tag{B.6}$$

By using the trigonometrical identity

$$cos^2(A) = \frac{1 + cos\,(2A)}{2}$$

it can be shown that $cos^2(\Delta\phi) + cos^2(\Delta\phi - \frac{2\pi}{3}) + cos^2(\Delta\phi + \frac{2\pi}{3}) = \frac{3}{2}$. Therefore, the summation of the three terms in equation (B.6) gives

$$\mathcal{N} = P_1 + P_2 + P_3 = \frac{3\sqrt{3}}{2} I_0^2 N^2 \,\dot{\Delta\phi}. \tag{B.7}$$

Integration of the expression in equation (B.7) yields an output which is a linear function of $\Delta\phi$. However, this integration still depends on the intensity of the interferometer outputs since there is a factor of I_0 in this equation. Therefore, the third stage of the demodulator is implemented to eliminate this factor by adding the square of the three terms in equation (B.3)

$$\begin{aligned}\mathcal{D} &= B_1^2 + B_1^2 + B_1^2 \\ &= I_0^2 N^2 \left[cos^2(\Delta\phi) + cos^2(\Delta\phi - \frac{2\pi}{3}) + cos^2(\Delta\phi + \frac{2\pi}{3})\right] \\ &= \frac{3}{2} I_0^2 N^2. \end{aligned} \tag{B.8}$$

The I_0^2 factor is eliminated by dividing equation (B.7) by (B.8)

$$\frac{\mathcal{N}}{\mathcal{D}} = \frac{\frac{3\sqrt{3}}{2} I_0^2 N^2 \dot{\Delta\phi}}{\frac{3}{2} I_0^2 N^2} = \sqrt{3}\,\dot{\Delta\phi}. \tag{B.9}$$

Integration of this equation yields

$$\int \frac{\mathcal{N}}{\mathcal{D}} = \int \sqrt{3}\,\dot{\Delta\phi} = \sqrt{3}\,\Delta\phi \tag{B.10}$$

which is a linear function which depends only on $\Delta\phi$.

C Digital Implementation of Differentiate and Cross-multiply Demodulation

The MATLAB codes used for phase demodulation are as follow:

```
01  function [Vout]= PhaseDet3 (v1,v2,v3)
02
03      siz=size(v1,1);
04
05      DC= (v1+v2+v3)/3;
06      v1=v1-DC;
07      v2=v2-DC;
08      v3=v3-DC;
09
10      SUMofSQUARE=v1.^2 + v2.^2 + v3.^2;
11
12      v1_dot=(diff(v1(1:siz-1,:))+diff(v1(2:siz,:)))/2;
13      v2_dot=(diff(v2(1:siz-1,:))+diff(v2(2:siz,:)))/2;
14      v3_dot=(diff(v3(1:siz-1,:))+diff(v3(2:siz,:)))/2;
15
16      Pro_of_diff1 = (v1(2:siz-1,:)).*(v2_dot-v3_dot);
17      Pro_of_diff2 = (v2(2:siz-1,:)).*(v3_dot-v1_dot);
18      Pro_of_diff3 = (v3(2:siz-1,:)).*(v1_dot-v2_dot);
19
20      sumOFproOFdiff = Pro_of_diff1 + Pro_of_diff2 + ...
21                       Pro_of_diff3;
22
23      Vout= (cumtrapz(sumOFproOFdiff./ ...
24            SUMofSQUARE(2:siz-1,:))) /sqrt(3);
25
26  end
```

The MATLAB codes are included to illustrate how differentiate and cross-multiply demodulation (which has been explained in its continuous form in appendix B) is implemented digitally. More importantly, it shows how the derivatives of data for a certain section of the fibre has been defined and calculated.

The DC components of the input data are removed by the codes in line $5 \sim 8$. Therefore, these lines are equivalent to the first stage of phase demodulation demonstrated in appendix B.

The differentiation of data is implemented in lines $12 \sim 14$. The discrete form of differentiation is called difference and is defined as the subtraction of adjacent data

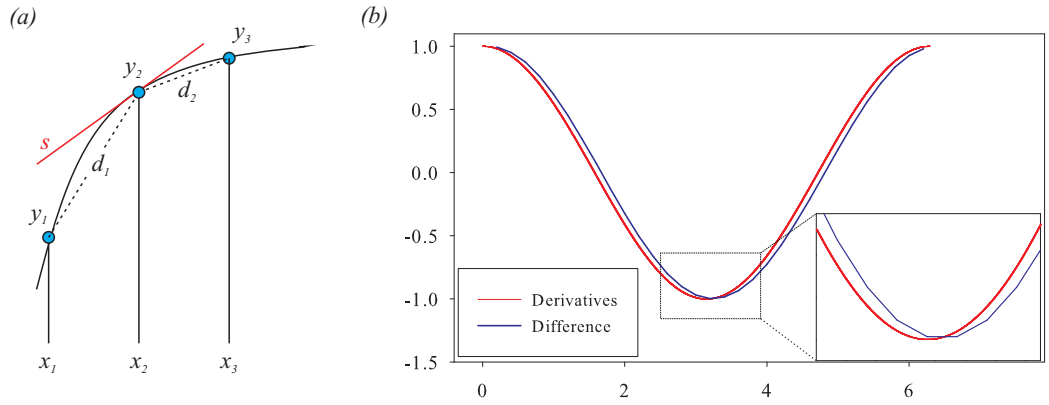

Figure C.1: Discrepancy between the derivative and the difference of a function.

points

$$d_n = \frac{y_n - y_{n-1}}{x_n - x_{n-1}}. \tag{C.1}$$

However, this definition cannot be used for calculation of the derivatives in the phase demodulator since the difference between two points is not equivalent to the slope of the data points. According to figure C.1(a), the slope of the black curve at point x_2, S, is not equal to the slope of the difference between x_1 and x_2, which is labelled as d_1. Figure C.1(b) demonstrates the discrepancy between the derivative and the difference of a sinusoidal function. The inset of this figure shows an enlarged scale of the two lines. From this figure, it is clear that the divergence between the derivative and the difference of a non-linear function depends on the rate of sampling of that function.

To estimate the derivative of the inputs more accurately, the value of the slope at a certain point was defined as

$$S_n = \frac{d_{n+1} + d_n}{2} = \frac{1}{2}\,[\,\frac{y_{n+1} - y_n}{x_{n+1} - x_n} + \frac{y_n - y_{n-1}}{x_n - x_{n-1}}\,]. \tag{C.2}$$

In other words, the slope at each point was defined as the average of the difference of that point relative to points before and after it. Since the data acquistion unit samples the backscattered light at fixed intervals, it can be shown that $x_{n+1} - x_n = x_n - x_{n-1}$. Therefore, simplifying equation (C.2) gives

$$S_n = \frac{y_{n+1} - y_{n-1}}{x_{n+1} - x_{n-1}}. \tag{C.3}$$

This is the definition which has been implemented in the MATLAB code. The rest of the codes are executing the rest of the algorithm described in figure B.1.

D Publications

D.1 Journal Publications

- A. Masoudi, M. Belal, T. P. Newson, "A distributed optical fibre dynamic strain sensor based on phase-OTDR," Measurement, Science and Technology, vol. 24, 085204, 2013.
- A. Masoudi, M. Belal, T. P. Newson, "Distributed dynamic large strain optical fiber sensor based on the detection of spontaneous Brillouin scattering," Optics Letters, vol. 38, pp. 3312-3315, 2013.
- A. Masoudi, T. P. Newson, "Distributed optical fibre dynamic magnetic field sensor based on magnetostriction," Applied Optics, vol. 53, pp. 2833-2838, 2014.
- A. Masoudi, M. Belal, T. P. Newson, "A distributed optical fibre acoustic sensor," Measurment, Science and Technology (Submitted).

D.2 Conference Contributions

- A. Masoudi, "Mapping vibration and strain using fibre optic sensors," Faculty of Engineering and the Environment, An ISVR seminar, University of Southampton, 24 Feb, 2014.
- A. Masoudi, M. Belal, T. P. Newson, "Distributed optical fibre audible frequency sensor ," OFS 23 (23rd International Conference on Optical Fiber Sensors) , Santander, Spain, 2-6 June, 2014.
- A. Masoudi, G. Brambilla, "The ultimate strength of silica nanofibre bundle," Optical Nanofiber Applications: From Quantum to Bio Technologies, Okinawa, Japan (Submitted).